Pseudospin pairing and transport in atomic Fermi gases and bilayer systems

printed by Ipskamp Drukkers
ISBN: 978-90-393-5827-6

Pseudospin pairing and transport in atomic Fermi gases and bilayer systems

Pseudospinpaarvorming en -transport in fermionische atoomgassen en dubbellaags systemen

(met een samenvatting in het Nederlands)

Proefschrift

ter verkrijging van de graad van doctor aan de Universiteit Utrecht op gezag van de rector magnificus, prof. dr. G. J. van der Zwaan, ingevolge het besluit van het college voor promoties in het openbaar te verdedigen op woensdag 12 september 2012 des ochtends te 10:30 uur

door

Martijn Peter Mink

geboren op 24 december 1984 te Geldrop

Promotor: Prof. dr. ir. H. T. C. Stoof
Co-promotor: Dr. R. A. Duine

Contents

Publications

This Thesis is based on the following publications:

- Chapter 2: The Influence of Remote Bands on Exciton Condensation in Double-Layer Graphene, M. P. Mink, A. H. MacDonald, H. T. C. Stoof, and R. A. Duine, Phys. Rev. B **84**, 155409 (2011).
- Chapter 3: Probing the topological exciton condensate via Coulomb drag, M. P. Mink, H. T. C. Stoof, R.A. Duine, Marco Polini, G. Vignale, Phys. Rev. Lett **108**, 186402 (2012).
- Chapter 4: Spin transport in a unitary Fermi gas close to the BCS transition, M. P. Mink, V. P. J. Jacobs, H. T. C. Stoof, Marco Polini, G. Vignale, and R. A. Duine, to be submitted.
- Chapter 5: Boltzmann-transport theory for the drag resistivity close to a phase transition: from ultracold Fermi gases near a Stoner instability to spatially separated electron-hole systems close to exciton condensation, M. P. Mink, H. T. C. Stoof, Marco Polini, G. Vignale, and R. A. Duine, to be submitted.

Other articles the author has contributed to

- Vortex-lattice pinning in two-component Bose-Einstein condensates, M. P. Mink, C. Morais Smith, and R. A. Duine, Phys. Rev. A **79**, 013605 (2009).
- Ion beam shaping of Au nanoparticles in silica: Particle size and concentration dependence E. A. Dawi, G. Rizza, M. P. Mink, A. M. Vredenberg, and F. H. P. M. Habraken, J. Appl. Phys. **105**, 074305 (2009).

Chapter 1

Introduction

1.1 Phase transitions and transport coefficients

One of the most interesting aspects of physics is the study of phase transitions. When a system parameter, e.g. the temperature, is changed, the system can undergo a transition from one phase into another. Young children are already familiar with the transition of water going from the liquid to the solid phase (ice), when the temperature drops below the transition (freezing) temperature of zero degrees Celsius. Especially in the Netherlands, the importance of this transition cannot be overstated. Every winter, the entire country holds its breath to see wether a thick enough top layer of water in the canals undergoes the transition from the liquid to the solid phase, so that they can go ice skating. Another phase transition which is rooted in the Dutch history is superconductivity. In 1911, Kamerlingh Onnes discovered in Leiden that the electrical resistance of mercury drops to zero when cooled below 4 K [1]. It turns out that for such low temperatures, mercury is in the superconducting state, and that the sudden drop of the electrical resistance is but one of many interesting properties of this state. The electrical resistance is a so-called transport coefficient, since it relates the force on the electrons in mercury (the voltage) to the transport of charge due this force (the electrical current). The value of this transport coefficient is intimately linked to the phase of the system: above the transition temperature to superconductivity, where the system is in the normal state, it is nonzero, but it vanishes in the superconducting state. Actually, the presence of the phase transition influences the behavior of the resistance also above the transition temperature. Here, critical fluctuations suppress the resistivity, which can be used as a precursor for the transition: the presence of the phase transition can be inferred from the behavior of the transport coefficient above the transition temperature. This phenomenon is the main subject of this Thesis. We study the behavior of the so-called drag resistivity in several physical systems close to a phase transition. The drag resistivity can be described as the ability of one type of particles to move or drag along an other type. In this Thesis we deter-

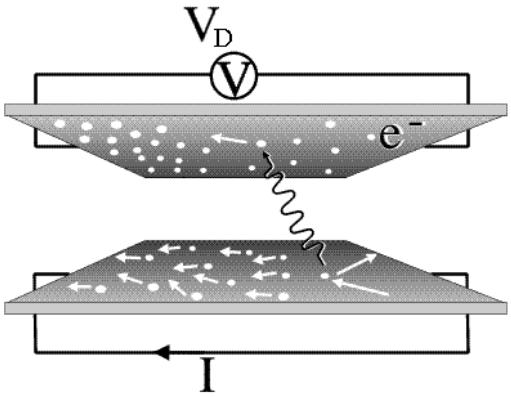

Figure 1.1: Illustration of a Coulomb drag measurement: a pair of two-dimensional electron gases is separated by a tunnel barrier. A current is applied in one of the layers leading to a voltage drop in the other. (Adapted with permission from http://www.sp.phy.cam.ac.uk/SPWeb/).

mine this drag resistivity in cold atomic Fermi gases close to the superconducting or ferromagnetic transition, and in electron-hole bilayers, graphene double layers, and topological insulator thin films close to exciton condensation.

1.2 Drag Resistance

In this Section we introduce the transport coefficient called the drag resistance. Imagine a collection of a type A particles which are moving in some direction, so that the collection has a total momentum different from zero in that direction. The particles might interact among themselves, but this does not change the total momentum of the collection. Now, imagine a collection of particles of a different type B which are at rest and are brought in contact with the moving collection of A particles. When the particles of the two types do not interact, the particles of type A just pass by the particles of type B, which remain at rest. However, when the particles of the two types do interact, momentum will be transferred between the two collections: the total momentum of the collection of A particles will decrease and the collection of B particles will start moving. Due to momentum conservation, they must move in the same direction as the A particles were moving. In this way, the B particles are dragged along by the A particles, and the drag resistance shows how effective this process occurs.

Now, we give a more precise definition of the drag resistance. We consider the setup shown in Fig. 1.1, consisting of two layers each containing one two-

dimensional electron gases (which we explain below). A barrier between the layers (not shown) prevents the electrons from tunneling from the top to the bottom layer or vice versa. A current is run through the bottom layer (also called the active or drive layer) but no current is allowed in the top layer (also called the passive layer). The moving electrons in the bottom layer will exchange momentum with the electrons in the top layer by the Coulomb interaction between them. Since electrons are moving to the left in the top layer, a negative charge will build up on the left side in that layer. This process continues until an equilibrium is reached in which the force from the electrons in the bottom layer on those in the top layer is canceled by the repulsion due to the built up negative charge on the left side of the top layer. In this equilibrium, a voltage drop can be measured between both sides of the top layer. The drag resistance is then the ratio between this voltage drop and the current in bottom layer. Since the Coulomb interaction is responsible for the effect it is named Coulomb drag. In 1991 this effect was measured experimentally for the first time by Gramila *et al.*, as shown in Fig. 1.2 [2].

To make this effect more explicit, we present a phenomenological calculation of the drag resistivity in a bilayer system, which is just the drag resistance divided by the length and multiplied with the width of the sample. In general, the electrons in a solid-state system move with high velocities in all directions. When a current is flowing this is still true, but now the mean velocity is not zero. This so-called drift velocity is much smaller than the typical velocity of a single electron. Using Newton's third law, we may write an equation for the drift velocity $\mathbf{v}$ of the electrons in a single layer under the influence of an electric field $\mathbf{E}$

$$nm\frac{d\mathbf{v}}{dt} = -ne\mathbf{E}, \tag{1.1}$$

where m is the mass of the electrons, $-e$ their charge, and n their density. The left-hand side of Eq. (1.1) is the time derivative of the total momentum density in the layer. The term $-ne\mathbf{E}$ gives the force on the electrons due to the electric field. The electric field gives a constant acceleration of the electrons and a quickly increasing current. However, we know from experience that in reality something else happens, namely that by Ohm's law the electric field and the current are proportional. What is missing in Eq. (1.1) is the effect of scattering processes in the layer, which would quickly relax any current back to zero in the absence of an electric field. Introducing the phenomenological transport relaxation time τ, Eq. (1.1) is corrected to

$$nm\frac{d\mathbf{v}}{dt} = -ne\mathbf{E} - \frac{nm\mathbf{v}}{\tau}. \tag{1.2}$$

Now, we may find a steady state solution ($d\mathbf{v}/dt = 0$) where the current density $\mathbf{j} = -ne\mathbf{v}$ and the electric field are proportional. We easily find the resistivity ρ

$$\rho \equiv \frac{E}{j} = \frac{m}{\tau ne^2}, \tag{1.3}$$

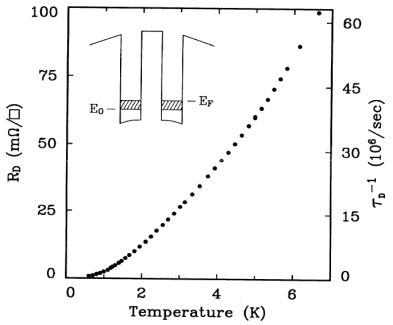

Figure 1.2: The results of Gramila *et al.* showing the drag resistance R_D versus the temperature. Picture taken from Ref. [2]

which is the so-called Drude expression for the resistivity. When there are no scattering processes $\tau = \infty$ and the resistivity is zero.

Now, we move on to the case of two layers coupled by the Coulomb interaction

$$nm\frac{d\mathbf{v}_t}{dt} = -ne\mathbf{E}_t - \frac{nm\mathbf{v}_t}{\tau} - \Gamma_D(\mathbf{v}_t, \mathbf{v}_b), \tag{1.4}$$

$$nm\frac{d\mathbf{v}_b}{dt} = -ne\mathbf{E}_b - \frac{nm\mathbf{v}_b}{\tau} + \Gamma_D(\mathbf{v}_t, \mathbf{v}_b). \tag{1.5}$$

We introduced the layer index t for the top layer and b for the bottom layer for the electric field and drift velocities. We added the terms $\pm\Gamma_D(\mathbf{v}_t, \mathbf{v}_b)$ which describe the momentum exchange due to the Coulomb interaction between the electrons in the layers. Note that due to momentum conservation, the contribution in the top layer equation should be opposite to the one in the bottom layer equation. The function $\Gamma_D(\mathbf{v}_t, \mathbf{v}_b)$ should vanish when $\mathbf{v}_t = \mathbf{v}_b$. Indeed, when both drift velocities are equal, no net momentum exchange should take place between the layers. Thus, we may set $\Gamma_D(\mathbf{v}_t, \mathbf{v}_b) = \Gamma_D(\mathbf{v}_t - \mathbf{v}_b)$ in Eqs. (1.4) and (1.5). We want to consider the so-called linear response regime, in which the electric fields and drift velocities are small. Thus, we may use the first order expansion $\Gamma_D(\mathbf{v}_t - \mathbf{v}_b) = \Gamma_D'(\mathbf{0}) \times (\mathbf{v}_t - \mathbf{v}_b)$. Next, we apply Eqs. (1.4) and (1.5) to the situation of Fig. 1.1, where $\mathbf{v}_t = 0$. We use Eq. (1.4) to relate $\mathbf{v}_b$ and $\mathbf{E}_t$ in the steady state. The drag resistivity ρ_D is then

$$\rho_D \equiv \frac{E_t}{j_b} = \frac{\Gamma_D'(\mathbf{0})}{e^2n^2}. \tag{1.6}$$

Thus, the drag resistivity is completely determined by the magnitude of the momentum exchange between the layers, and independent of any scattering processes within the layers, or the absence thereof. The problem of determining the drag

resistivity reduces to finding the momentum exchange between the layers due to the interlayer interaction.

Another drag phenomenon closely related to Coulomb drag is spin drag. In this case, the two types of carriers are not physically separated in different layers, but instead are present in interpenetrating clouds, e.g. the free spin up and spin down electrons in a metal. In this Thesis we will be interested in spin drag, not in solid-state systems, but in cold atomic Fermi gases where the interaction between the spin species is not the Coulomb but the inter-atomic Lennard-Jones-like interaction.

1.3 Experimental Systems

In this Section we discuss the physical systems we consider in this Thesis. Also, we discuss the various phase transitions that can occur in these systems.

1.3.1 Ultracold Fermi gases and superconductivity

In the last decades of the previous century, there was a great experimental effort focussing on the cooling of dilute atomic (neutral) gases to extremely low temperatures. The typical temperatures the experimentalists aimed at where far below a millikelvin, which is too low to obtain with any cryogenic cooling technique. Since any contact with a wall of a container would spoil the low temperature and heat the gas, they have to be trapped using either magnetic or electric fields. Instead of cryogenic techniques, a combination of laser cooling and evaporative cooling was used in the race to reach lower and lower temperatures. In 1997 Steven Chu, Claude Cohen-Tannoudji, and William D. Phillips were awarded the Nobel prize in physics for their contribution to the development of these cooling techniques.

Now, why did people want to reach these low temperatures? The reason is that quantum effects become important at these low temperatures. Atomic gases would be a novel and highly interesting experimental system for the observation and study of these effects. All this effort culminated in 1995 in the observation of Bose-Einstein condensation in a gas of rubidium-87 atoms (which are bosons) cooled to a temperature of 170 nanokelvin [3], see also Fig. 1.3. To be able to understand what Bose-Einstein condensation is, we first need to give some background.

In a cloud of bosons at a high temperature, most particles will be in different microscopic energy states, since in this way the system is in a state with a large entropy. When we lower the temperature, minimizing the energy becomes more important with respect to maximizing the entropy and the system will start to put more and more particles in the lowest energy state to lower its energy. It turns out that there is a sharp transition temperature below which the number of particles in the single-particle ground state becomes macroscopic, which means of the same

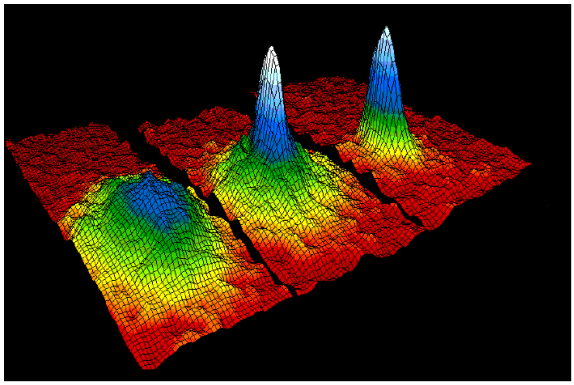

Figure 1.3: The velocity distribution of a cloud of ultracold bosons in a trap for different temperatures. In the graph on the left the temperature is larger than the condensation temperature. When the temperature is lowered below the condensation temperature, a peak appears in the middle of the cloud (middle graph) which is caused by a macroscopic occupation of the single-particle ground state: the gas has Bose-Einstein condensed. When the temperature is lowered even further (right graph), even more particles move into the single-particle ground state. Picture taken from http://www.bec.nist.gov/gallery.html.

order as the total number of particles in the system. The system is then said the have Bose-Einstein condensed. For their pioneering experiments in this field the 2003 Nobel prize in physics was awarded to Eric Cornell, Wolfgang Ketterle, and Carl Wieman.

The systems we consider in this Thesis do not consist of bosons but of fermions. Each microscopic state can only hold a single fermion, and for that reason fermions can not condense. So why did we talk about Bose-Einstein condensation? The reason is that when two fermions form a pair, that pair is a boson, and these pairs *can* condense. Indeed, superconductivity in a metal as studied by Kamerlingh Onnes can be seen as the Bose-Einstein condensation of pairs of spin up and spin down electrons, called Cooper pairs [4]. For two fermions to be able to form a pair, there needs to be an attractive interaction between them. In a metal, this attractive interaction is caused by the exchange of phonons (lattice vibrations). Also in cold atomic gases with two species of fermions, Bose condensation of pairs can occur, as was first predicted theoretically [5] and later shown experimentally [6]. In this case, there is no underlying atomic lattice but the interaction between the atoms itself can be attractive. Bose-Einstein condensation of pairs in cold atomic Fermi gases is one of the phase transitions we consider in this Thesis.

As said above, in ultracold fermi gases the phenomenon of spin drag can be observed. An interesting feature for this system is that the scattering pro-

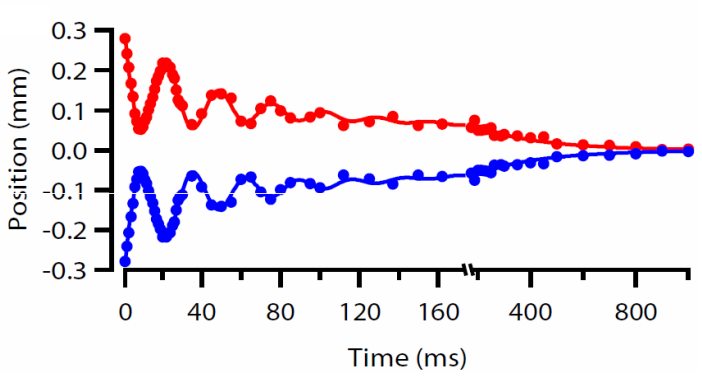

Figure 1.4: The center-of-mass motion of the spin up (red) and spin down (blue) clouds with respect to the trap center from Sommer *et al.* [7]. After being released in the non-equilibrium position, the clouds first bounce off each other several times (first part of plot) and then relax back to their equilibrium positions (second part of plot). The steady decrease in speed with which the clouds approach each other is caused by their mutual friction: spin drag. Picture taken from Ref. [7].

cessing within a species are nearly absent, and so the scattering times τ's in Eqs. (1.4) and (1.5) are infinite and the terms proportional to $1/\tau$ vanish. In 2011 an experimental group at MIT measured spin drag in an ultracold Fermi gas for the first time [7]: we show their results in Fig. 1.4.

1.3.2 Bilayers and exciton condensation

The bilayer systems we study in this Thesis resemble closely the setup of Fig. 1.1. Two parallel layers with electronic carriers are separated by a barrier, which prevents tunneling between the layers. Since the carriers are charged, they interact via the Coulomb interaction to exchange momentum, leading to the phenomenon of Coulomb drag described above. However, there is one important difference between our bilayers and the setup of Fig. 1.1. This difference is that the carriers in one of the two layers are not electrons but holes. A hole is a vacancy or empty state in a completely filled band just as an electron is an occupied state in a largely empty band, as explained in Fig. 1.5. Since the presence of a hole means the absence of an electron, a hole has a positive charge and can carry current, just as an electron can. Coulomb drag can occur between an electron and a hole layer, in the same way as it can occur between two electron layers, as was demonstrated experimentally in 1992 [8].

One of the reasons to be interested in bilayer systems with an electron and a hole layer is that such layers have the possibility to undergo exciton condensation.

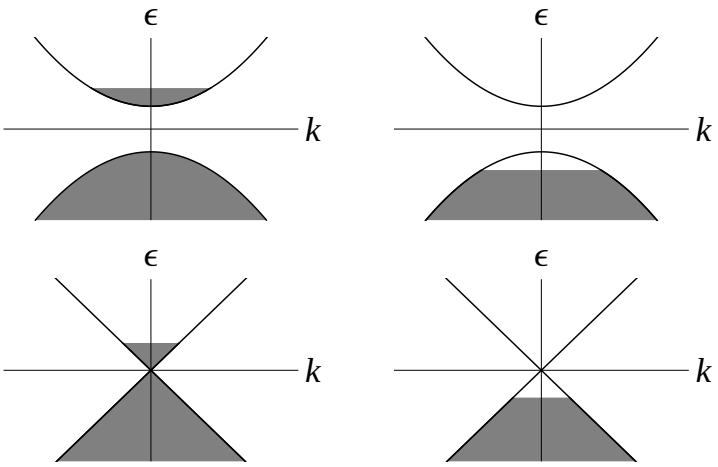

Figure 1.5: In these panels we explain the concept of holes. In panels (a) and (b) we show a typical semiconductor band structure: a band gap between two quadratic bands giving the relation between the energby ϵ and the momentum k. When the chemical potential lies in the upper band as in panel (a), the lower band is completely filled and inert. The electrons in the upper band can participate in transport, since there are free states in which they can move. Similarly, when the chemical potential lies in the lower band like in panel (b), the states with energy larger than the chemical potential are unoccupied and called holes. Also these hole can participate in transport, since there are occupied electron states in which they can move. In panels (c) and (d), we show similarly the presence of electrons (panel (c)) and holes (panel (d)) for a linear band with zero band gap. This so-called Dirac cone is the dispersion in graphene and on the surface of a three-dimensional topological insulator.

An exciton is a pair consisting of an electron and hole, which atrract each other by the Coulomb interaction. In three-dimensional systems, the electron and the hole typically recombine very quickly. In a bilayer system this problem is not present: the electrons are spatially separated from the holes so the recombination of excitons is greatly suppressed. These so-called indirect excitons are long lived and are a promising candidate to undergo exciton condensation, which is the Bose-Einstein condensation of electron-hole pairs, just as superconductivity is the Bose-Einstein condensation of electron-electron pairs. Very recently, the exciting first direct measurement of spontaneous coherence in a gas of indirect excitons due to exciton condensation was reported [9]. In this Thesis we consider three different experimental realizations of a bilayer with an electron layer and an hole layer: electron-hole bilayers, graphene double layers, and topological insulator thin films.

It is possible to create a structure consisting of a GaAs layer and an AlGaAs

layer such that there is a two-dimensional quantum well at the interface. Electrons can be trapped in this well and for low enough temperatures, excitations in the perpendicular direction are frozen out, so that electrons can effectively move only in a two-dimensional space. This two-dimensional electron gas has band structure as shown in panels (a) and (b) of Fig. 1.5. An electron-hole bilayer is then created by stacking two of these two-dimensional electron gases and shifting the chemical potential by doping or applying external gate voltages such that one of the layers contains electrons (as in panel (a) of Fig. 1.5) and the other one holes (as in panel (b) of Fig. 1.5). When the wells are deep enough tunneling of carriers between the layers becomes negligible.

A graphene double layer is a structure of two parallel graphene layers separated by a tunnel barrier. Since its isolation in 2004 [10], graphene has attracted much attention, because of its unusual properties and promise for technological applications. Already in 2011, the Nobel prize in Physics was awarded to Andre Geim and Konstantin Novoselov for their pioneering work on this material. Graphene is a single layer of graphite in which the carbon atoms are ordered in a two-dimensional honeycomb lattice, as shown in Fig. 1.7. In Section 1.5.1 we calculate the band structure for this material, which is shown in Fig. 1.6. For low enough temperatures, the energy of the electrons will be small, and then the dispersion (near the black dots in Fig. 1.6) is to a good approximation given by the Dirac cones as shown in panels (c) and (d) of Fig. 1.5. Graphene was one of the first realizations of this Dirac cone in a condensed-matter system.

Even more recent is the first realization of a three-dimensional time-reversal invariant topological insulator [11]. These materials are insulating in the bulk, but since the topology of the wave functions is non-trivial there, topologically protected Dirac cones are present on the surface, so that the surfaces are conducting. By application of a suitable gate voltage, electrons (panel (c) of Fig. 1.5) can be induced on the one surface, and holes (panel (d) of Fig. 1.5) on the other. In a topological insulator thin film these two surfaces are separated by a thin layer of the insulating bulk of the material, and drag effects and exciton condensation due to the Coulomb interaction can be studied.

1.4 Outline

Before we give some technical background of the concepts introduced above, we first present an outline of this Thesis. In chapter 2 we calculate the transition temperature for exciton condensation in double layer graphene, showing that the remote bands can play a supporting role in this transition. In chapter 3 we consider a topological insulator thin film and calculate the behavior of the drag resistivity close to the transition temperature. We find a strong enhancement which can be

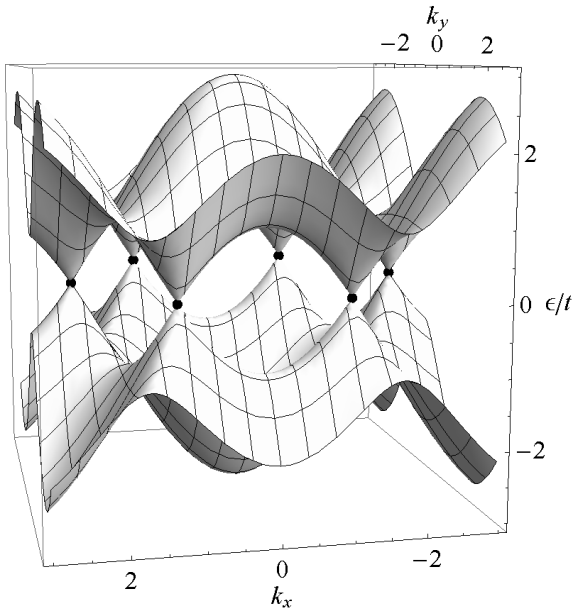

Figure 1.6: The electron dispersion of graphene showing the energy scaled by the hopping strength t as a function of the momenta in the x and y direction. For low energy (near the black dots), the dispersion is well approximated by the Dirac cones shown in panels (c) and (d) of Fig. 1.5.

used as a precursor for the transition. In chapter 4 we discuss an ultracold Fermi gas close to the superconducting transition and compare two different methods to obtain the drag resistivity, each taking into account a different phenomenon which affects the drag resistivity close to the transition. Finally, in chapter 5, we present a uniform theoretical framework to determine the drag resistivity in all experimental systems considered in this Thesis.

1.5 Technical background

In this Section we give some technical background needed to understand the chapters of this Thesis. We show explicitly how to determine the dispersion of graphene shown in Fig. 1.6, starting from the tunneling Hamiltonian. Then, we study the ferromagnetic phase transition starting from the many-particle Hamiltonian. We introduce the concept of an order parameter, and study under which conditions the ferromagnetic transition can occur. Finally, we show that Bose-Einstein condensation of fermion pairs, can be studied by performing a so-called particle-hole

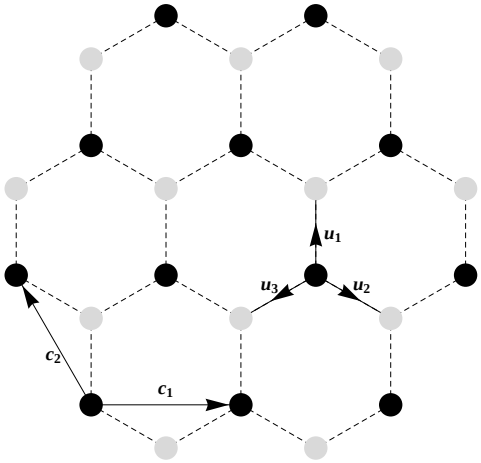

Figure 1.7: The honeycomb lattice structure of graphene. The black dots are the carbon atoms of sublattice A and the gray dots are the carbon atoms of sublattice B. The vectors are explained in the main text.

transformation in the previous calculation.

1.5.1 Graphene Dispersion

The honeycomb lattice structure of graphene can be represented by two interpenetrating triangular sublattices A and B as shown in Fig. 1.7, where the black (gray) dots are the carbon atoms of sublattice A (B). Sublattice A is spanned by the lattice vectors $\mathbf{c}_1 = \sqrt{3}a(1,0)$ and $\mathbf{c}_2 = (a/2)(-\sqrt{3},3)$, where $a = 0.142$ nm is the distance between two neighboring carbon atoms. The positions of the B-atoms are shifted by $a\hat{\mathbf{y}}$ with respect to the A atoms. Tunneling can occur in three directions between the A and B atoms, shown in Fig. 1.7 as $\mathbf{u}_1, \mathbf{u}_2$, and $\mathbf{u}_3$. The tunneling Hamiltonian is

$$H = -t \sum_{\mathbf{c}\in A, i=1,2,3} \left[a^\dagger_{\mathbf{c}} b_{\mathbf{c}+\mathbf{u}_i} + b^\dagger_{\mathbf{c}+\mathbf{u}_i} a_{\mathbf{c}} \right], \tag{1.7}$$

where $t = 2.8$ eV is the tunneling strength and where the operators $a^\dagger_{\mathbf{c}}$ and $b^\dagger_{\mathbf{c}}$ create a particle at position $\mathbf{c}$ in sublattice A and B, respectively. We transform the operators to reciprocal space

$$a_{\mathbf{c}} = \frac{1}{\sqrt{N}} \sum_{\mathbf{k}} e^{i\mathbf{k}\cdot\mathbf{c}} a_{\mathbf{k}} \quad \text{and} \quad b_{\mathbf{c}} = \frac{1}{\sqrt{N}} \sum_{\mathbf{k}} e^{i\mathbf{k}\cdot\mathbf{c}} b_{\mathbf{k}}, \tag{1.8}$$

where N is the number of A sublattice atoms. Using these relations, we find the Hamiltonian

$$H = \sum_{\mathbf{k}} \begin{pmatrix} a_{\mathbf{k}}^\dagger & b_{\mathbf{k}}^\dagger \end{pmatrix} \begin{pmatrix} 0 & f(\mathbf{k}) \\ f^*(\mathbf{k}) & 0 \end{pmatrix} \begin{pmatrix} a_{\mathbf{k}} \\ b_{\mathbf{k}} \end{pmatrix}, \tag{1.9}$$

where the Fourier transform of the hopping is

$$f(\mathbf{k}) = -t \left(1 + e^{-i\mathbf{k}\cdot\mathbf{c}_1} + e^{-i\mathbf{k}\cdot(\mathbf{c}_1+\mathbf{c}_2)} \right). \tag{1.10}$$

To find the dispersion we diagonalize the Hamiltonian in Eq. (1.9) and find the bands $\pm|f(\mathbf{k})|$, which are shown in Fig. 1.6.

1.5.2 Ferromagnetism

To be able to introduce some theoretical concepts used in this Thesis, we present a model calculation to describe the ferromagnetic transition in a Fermi gas. We consider a two-component Fermi gas in which only particles with different spin interact. The creation and annihilation operators for a fermion with momentum $\mathbf{k}$ in spin state $|\sigma\rangle$ are $c_\sigma^\dagger(\mathbf{k})$ and $c_\sigma(\mathbf{k})$, respectively. The non-interacting part of the Hamiltonian is

$$H_0 = \sum_{\mathbf{k},\sigma} \xi(\mathbf{k}) c_\sigma^\dagger(\mathbf{k}) c_\sigma(\mathbf{k}), \tag{1.11}$$

where $\xi(\mathbf{k}) = \hbar^2 k^2/2m - \mu$ is the dispersion with μ the chemical potential. The product $c_\sigma^\dagger(\mathbf{k})c_\sigma(\mathbf{k})$ just counts the number of particles with momentum $\mathbf{k}$ and spin σ. The contribution from the contact interaction between the spins is

$$H_I = \frac{V_0}{V} \sum_{\mathbf{k},\mathbf{k}',\mathbf{q}} c_\uparrow^\dagger(\mathbf{k}) c_\uparrow(\mathbf{k}-\mathbf{q}) c_\downarrow^\dagger(\mathbf{k}') c_\downarrow(\mathbf{k}'+\mathbf{q}), \tag{1.12}$$

where V_0 is the repulsive contact interaction strength $V_0 > 0$. We introduce the density fields as follows

$$n_\uparrow = \frac{1}{V} \sum_{\mathbf{k}} \langle c_\uparrow^\dagger(\mathbf{k}) c_\uparrow(\mathbf{k}) \rangle \equiv n/2 + m \tag{1.13}$$

$$n_\downarrow = \frac{1}{V} \sum_{\mathbf{k}} \langle c_\downarrow^\dagger(\mathbf{k}) c_\downarrow(\mathbf{k}) \rangle \equiv n/2 - m, \tag{1.14}$$

where n is the total density and m the magnetization density $2m = n_\uparrow - n_\downarrow$. When m is nonzero the gas has (by definition) become polarized and undergone the ferromagnetic transition. Thus, m is the so-called order parameter for this transition: a quantity which is zero on one side of the transition (the normal state) and nonzero on the other side (the ordered state).

To introduce the order parameter m in our theory explicitly, we use the mean-field approximation in which we replace the operator pairs $c_\uparrow^\dagger(\mathbf{k})c_\uparrow(\mathbf{k}-\mathbf{q})$ and

$c_\downarrow^\dagger(\mathbf{k}')c_\downarrow(\mathbf{k}'+\mathbf{q})$ by their expectation values. This procedure leads to the appearance of energy shifts in the dispersion in the total Hamiltonian

$$H = \sum_{\mathbf{k},\sigma}(\xi(\mathbf{k}) - \sigma V_0 m)c_\sigma^\dagger(\mathbf{k})c_\sigma(\mathbf{k}), \tag{1.15}$$

where the spin label σ means $+1$ for spin up and -1 for spin down when used in an equation. In Eq. (1.15), we absorbed a spin-independent mean-field shift $V_0 n/2$ into the chemical potential. We see that the dispersion of a single spin species is shifted by the interaction strength times the magnetization. The next step is to see if there is a nonzero solution for the magnetization. To do so, we calculate the magnetization as function of the magnetization, which leads to a self-consistent equation for m. First, we determine the spin up and spin down densities

$$n_\sigma = \int d\epsilon \nu(\epsilon) n_F(\xi(\mathbf{k}) - \sigma V_0 m), \tag{1.16}$$

where $\nu(\epsilon)$ is the so-called density of states per volume and spin: $\nu(\epsilon)d\epsilon$ gives the number of states with energy between ϵ and $\epsilon + d\epsilon$. The function $n_F(\epsilon)$ is the Fermi-Dirac distribution function, which gives the number of particles in a state with energy ϵ. Subtracting the spin $\uparrow$ density from the spin $\downarrow$ density leads to

$$2m = \int d\epsilon \nu(\epsilon)[n_F(\epsilon - \mu - V_0 m) - n_F(\epsilon - \mu + V_0 m)]. \tag{1.17}$$

We are not so much interested in the precise value of m, but instead for which V_0 a nonzero value of m starts to be a solution. This information can be found by taking the derivative to m of the previous equation and then setting $m = 0$, which leads to

$$1 = -V_0 \int d\epsilon \nu(\epsilon) n_F'(\epsilon - \mu). \tag{1.18}$$

This equation can be solved numerically, but for our purposes, we only need the $T = 0$ solution. Then, the chemical potential is equal to the energy of highest filled state, the Fermi energy ϵ_F. The derivative of the Fermi function is $n_F'(\epsilon - \epsilon_F) = -\delta(\epsilon - \epsilon_F)$, leading to the condition

$$1 = \nu(\epsilon_F) V_0, \tag{1.19}$$

which is called the Stoner criterion.

The Stoner criterion determines the winner of the competition between interaction and kinetic energy. When the gas is completely polarized, the interaction energy is zero, since there is only one species present. Decreasing the polarization increases the interaction energy, which reaches a maximum in the unpolarized state, where the densities of spin $\uparrow$ and $\downarrow$ particles are equal. In contrast, the kinetic energy is minimized in the unpolarized state, where the Fermi levels for the

spin ↑ and ↓ species are equal. To get a nonzero magnetization, we need to move particles into higher energy states, which is increases the kinetic energy. Starting from the unpolarized state, V_0 is a measure for the gain in interaction energy after polarization, while $1/\nu(\epsilon_F)$ is a measure for the kinetic energy cost. Whichever of the two is largest, determines whether the gas will spontaneously polarize, as shown by the Stoner criterion.

1.5.3 Condensation of fermion pairs

In the previous Section we saw that a two-component Fermi gas can polarize under the influence of a repulsive interaction. When the interaction strength is larger than a critical value, it is energetically favorable for the gas to put more particles in one spin state than in the other. Next, we consider what can happen when this gas has an attractive interaction. It turns out that to study this case, we can conveniently use the results of the previous Section.

The order parameter describing the superconducting transition is not a density field like in the case of ferromagnetism. Superconductivity can be seen as Bose-Einstein condensation of Cooper pairs, which are pairs of spin up and spin down electrons. The creation operator for such a Cooper pair is the product $c_\uparrow^\dagger(\mathbf{k})c_\downarrow^\dagger(-\mathbf{k})$ and it turns out this operator has a nonzero expectation value in the superconducting state, while the expectation value is zero in the normal state. Thus, it can be used as an order parameter for this transition, which we will denote as Δ

$$\Delta = \frac{V_0}{V}\sum_{\mathbf{k}}\langle c_\uparrow^\dagger(\mathbf{k})c_\downarrow^\dagger(-\mathbf{k})\rangle. \tag{1.20}$$

Now, we could perform a similar mean-field approximation as in the previous section replacing either $c_\uparrow^\dagger(\mathbf{k})c_\uparrow^\dagger(\mathbf{k}')$ or $c_\downarrow(\mathbf{k}'+\mathbf{q})c_\uparrow(\mathbf{k}-\mathbf{q})$ by their expectation values. However, this calculation can be found in many textbooks, see e.g. Ref. [12]. Instead, we will perform some tricks to obtain the equation for Δ directly from the equation for the magnetization m in Eq.(1.17). The first step is to choose the x-axis as quantization axis for the fermion operators instead of the z-axis. We can express the old operators in the new operators

$$c_\uparrow(\mathbf{k}) = \frac{1}{\sqrt{2}}\left(c_+(\mathbf{k}) + c_-(\mathbf{k})\right) \quad \text{and} \quad c_\downarrow(\mathbf{k}) = \frac{1}{\sqrt{2}}\left(c_+(\mathbf{k}) - c_-(\mathbf{k})\right), \tag{1.21}$$

where $c_\pm(\mathbf{k})$ annihilates a fermion in a state with spin $\pm$ in the x-direction. We

may determine the magnetization in terms of these operators

$$\begin{aligned} m &= \frac{1}{2V}\sum_{\mathbf{k}}\langle c_{\uparrow}^{\dagger}(\mathbf{k})c_{\uparrow}(\mathbf{k}) - c_{\downarrow}^{\dagger}(\mathbf{k})c_{\downarrow}(\mathbf{k})\rangle \\ &= \frac{1}{V}\sum_{\mathbf{k}}\left[\langle c_{+}^{\dagger}(\mathbf{k})c_{-}(\mathbf{k})\rangle + \langle c_{-}^{\dagger}(\mathbf{k})c_{+}(\mathbf{k})\rangle\right] \\ &= \frac{2}{V}\sum_{\mathbf{k}}\langle c_{+}^{\dagger}(\mathbf{k})c_{-}(\mathbf{k})\rangle, \end{aligned} \tag{1.22}$$

where we assumed that the last expression is real. Thus, we have arrived at an alternative expression for the order parameter m. We rewrite the equation for m Eq.(1.17) in a form which will be useful below

$$\frac{1}{V_0} = -\int d\epsilon \nu(\epsilon)\frac{n_F(\epsilon-\mu-V_0 m) - n_F(\epsilon-\mu+V_0 m)}{[\epsilon-\mu-V_0 m]-[\epsilon-\mu+V_0 m]}. \tag{1.23}$$

At this point we have an equation for m which is a sum of expectation values of the type $\langle c_{+}^{\dagger}(\mathbf{k})c_{-}(\mathbf{k})\rangle$. We want to have an equation for Δ which is a sum of expectation values of the type $\langle c_{+}^{\dagger}(\mathbf{k})c_{-}^{\dagger}(-\mathbf{k})\rangle$. To make the connection, we perform a so-called particle-hole transformation on the $-$-particles in which we switch the creation and annihilation operators for the $-$-particles (but not for the $+$-particles): $c_{-}(\mathbf{k}) \to c_{-}^{\dagger}(-\mathbf{k})$ and $c_{-}^{\dagger}(\mathbf{k}) \to c_{-}(-\mathbf{k})$. Then, the order parameters are related as $V_0 m/2 \to \Delta$. Another consequence of the particle-hole transformation is that the energies of the $-$-particles are changed to their opposite values: the energy of a hole is minus the energy of a particle. Thus, we should replace $\epsilon-\mu+V_0 m \to -\epsilon+\mu-V_0 m$ in Eq. (1.23). Similarly, also the interaction strength should be changed $V_0 \to -V_0$. Again, we are only interested in the onset of Bose-Einstein condensation of Cooper pairs so we keep only the terms of lowest order in Δ. Performing all these steps leads to the equation

$$-\frac{1}{V_0} = \int d\epsilon \nu(\epsilon)\frac{1-2n_F(\epsilon-\mu)}{2(\epsilon-\mu)}, \tag{1.24}$$

where we used that $n_F(-x) = 1 - n_F(x)$. The equation (1.24) is the famous linearized BCS gap equation. The contribution from energies close to the Fermi energy for lower and lower temperatures diverges like $-\log(T/\epsilon_F)$. Thus, however small $|V_0|$, we may always find a temperature such that Eq. (1.24) is satisfied.

Chapter 2

Influence of remote bands on exciton condensation in double-layer graphene

We examine the influence of remote bands on the tendency toward exciton condensation in a system consisting of two parallel graphene layers with negligible interlayer tunneling. We find that the remote bands can play a crucial supporting role, especially at low carrier densities, and comment on some challenges that arise in attempting quantitative estimates of condensation temperatures.

2.1 Introduction

In the last few years, there has been enormous experimental and theoretical interest in the properties of graphene, a hexagonally ordered two-dimensional sheet of carbon atoms [13]. Graphene is a gapless semiconductor whose valence and conduction bands cross linearly near two inequivalent Dirac points (valleys) located at the honeycomb lattice Brillouin zone corners. Since the Fermi level in graphene can be shifted by the electric field effect [10], the density and polarity of the charge carriers can be tuned by application of a gate voltage.

A symmetric voltage applied between the layers of a double-layer graphene system can induce an electron density in one layer, and an equal hole density in the other. Under these circumstances electrons will tend [14, 15, 16] to form a broken symmetry state in which coherence is established spontaneously between separate layers in the absence of interlayer tunneling. The broken symmetry state is driven by Coulomb interactions between layers and favored by nesting between the nearly circular Fermi surfaces. In this state the one-particle electron density matrix has nonzero components that are off-diagonal in the layer indices. A bilayer

This chapter is published in Physical Review B: The Influence of Remote Bands on Exciton Condensation in Double-Layer Graphene, M. P. Mink, A. H. MacDonald, H. T. C. Stoof, and R. A. Duine, Phys. Rev. B **84**, 155409 (2011).

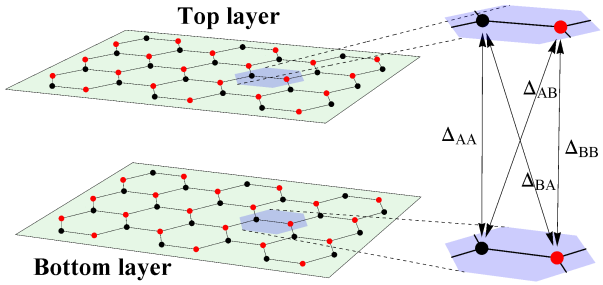

Figure 2.1: Double-layer graphene consists of two parallel graphene sheets. The black dots are atoms in sublattice A and the red dots in sublattice B. The four component structure of the condensate is illustrated at right. The exact definition of the order parameter Δ is given in Sec. 2.4.

spontaneous coherence state is a type of exciton condensate (see below) which has particularly interesting transport properties [17, 18] when the two layers can be contacted independently. In graphene the possibility of independently contacting two graphene sheets separated by a distance of several nanometers has recently been demonstrated [19, 20]. After performing a particle-hole transformation on the hole-like layer, the broken-symmetry state can be viewed as a spatially indirect electron-hole pair (exciton) condensate. This is the viewpoint we will use throughout this chapter.

In addition to having spin and valley degrees of freedom, electron states in single layer graphene are two-component spinors with a sublattice degree of freedom. As a consequence, the order parameter for exciton condensation has a four-component sublattice structure. The structure of the double-layer graphene system is illustrated in Fig. 2.1, where the blow-up at right emphasizes the 4-component structure of the order parameter. In the broken-symmetry state all elements of the expectation value $\langle c^\dagger_{t,\alpha} c_{b,\alpha'} \rangle$, where $c^\dagger_{t,\alpha}$ is the creation operator of an electron in the top layer in sublattice $\alpha = A, B$, and $c_{b,\alpha'}$ is the annihilation operator of an electron in the bottom layer in sublattice $\alpha' = A, B$, can be nonzero at each crystal momentum.

This system was first studied by Lozovik and Sokolik [14] for $k_F d \gg 1$, with k_F the Fermi momentum and d the interlayer distance, and later revisited by a number of authors [15, 16, 22, 21, 23, 24]. Min *et al.* [16] evaluated the ground state superfluid density of the condensate, demonstrating that it is proportional to

the carrier Fermi energy, and on this basis proposed that the Kosterlitz-Thouless (KT) transition temperature for exciton condensation could be of the order of room temperature in systems with high carrier densities and small layer separations. This suggestion was countered by Kharitonov *et al.* [22], who estimated that $T_c < 1$ mK because the interlayer interaction is strongly screened in the normal state. In this chapter we consider two graphene layers without any dielectric so that the effective dielectric constant for interlayer interactions $\epsilon = 1$. Our work differs from earlier work in that we include the influence of remote bands, which play a supporting role. When a static screening approximation is employed we find that the maximum critical temperature is of the order of Kelvins and occurs at rather low carrier densities. Since static screening underestimates the interlayer interaction, particularly for remote band effects, higher condensation temperatures appear to be a possibility.

This chapter is organized as follows. In Sec. 2.2 we present the main results of our analysis for the condensate structure and the transition temperature T_c. In Sec. 2.3 we present our discussion and conclusions. Sec. 2.4 describes important technical details of the calculations used to obtain the results described in Sec. 2.2.

2.2 Results

In this chapter we estimate the transition temperature and determine the optimal structure for exciton condensation in double-layer graphene. The details of this calculation are given in Sec. 2.4. We consider only order parameters that have zero center-of-mass momentum. Using mean-field theory we derive a self-consistent gap equation, which we solve numerically in two approximations. First, to gain physical insight, we approximate the screened Coulomb interaction by a contact interaction. We determine the strength of the contact interaction by performing an angular average over incoming and outgoing momenta on the Fermi surface. In this version of our calculation, we use the full graphene dispersion, but we find that substituting the Dirac dispersion with an appropriate ultra-violet cutoff gives nearly identical results. In an effort to obtain more quantitatively reliable results, we have also used a separable approximation to the screened Coulomb interaction, similar to the form used by Lozovik *et al.* [25], to determine the gap at zero temperature. This calculation is carried out within the Dirac approximation. The greatest source of uncertainty in our work is the approximation used for the screened interlayer interaction. In all of our explicit calculations we use a static approximation which overestimates screening. The critical temperatures we obtain will therefore tend to be underestimated.

In the present section we present the results of our calculations. We describe the optimal condensate structure, which turns out to be the same in both approx-

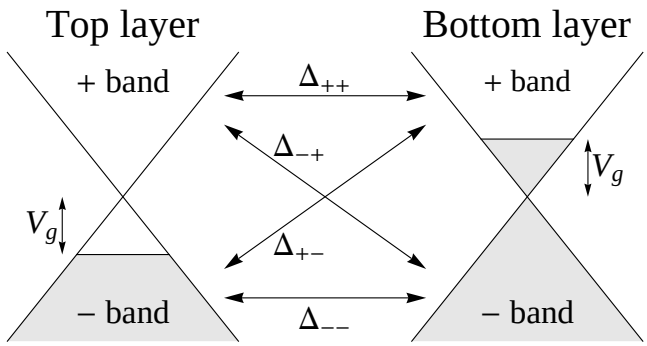

Figure 2.2: Dirac approximation band dispersions for the top and bottom layer. The shaded areas correspond to filled states. The four components of the order parameter in the band representation are indicated. These components are related to the components of the order parameter in the sublattice representation by a unitary transformation. In the close-band approximation only the (lower energy) valence band in the top layer (bottom left) and the (higher energy) conduction band of the bottom layer (top right) are retained.

imations. We then discuss the phase diagrams we obtain. The contact-interaction approximation leads to unphysically high values for the transition temperature, as may be expected for such a crude model. In contrast, using the separable approximation for the screened Coulomb interaction, we obtain a T_c of order of Kelvins for typical carrier Fermi energies $V_g = 0.25 - 0.5$ meV and interlayer distances $d < 4$ nm, respectively.

2.2.1 Condensate structure

The condensed state optimizes the order parameter sublattice structure ($\Delta_{\alpha,\alpha'}(\mathbf{k})$ with $\alpha, \alpha' = A, B$). (The explicit definition of the order parameter Δ is given in Sec. 2.4.) We find that the structure that is optimal (i.e. that minimizes the thermodynamic potential) has the form $\mathbf{\Delta} \equiv (\Delta_{AA}, \Delta_{AB}, \Delta_{BA}, \Delta_{BB}) = (\Delta_1, \Delta_2, -\Delta_2, -\Delta_1)$, where $\Delta_1 \gg \Delta_2$. The property that $\Delta_{AA} = -\Delta_{BB}$ can be understood in terms of the primary mechanism by which condensate formation lowers the energy of the system, namely the opening of an avoided crossing gap between the conduction band of one layer and the valence band of the other layer. In the Dirac-band approximation the conduction and valence band sublattice spinors are $(1, \exp(i\phi_{\mathbf{k}}))/\sqrt{2}$ and $(1, -\exp(i\phi_{\mathbf{k}}))\sqrt{2}$ respectively, where $\mathbf{k}$ is momentum measured from the Brillouin-zone corner and $\phi_{\mathbf{k}}$ is the angular orientation of this momentum. An order parameter with $\Delta_{AA} = -\Delta_{BB}$ couples these spinors with equal strength at all $\phi_{\mathbf{k}}$. To avoid confusion, we note that this order parameter

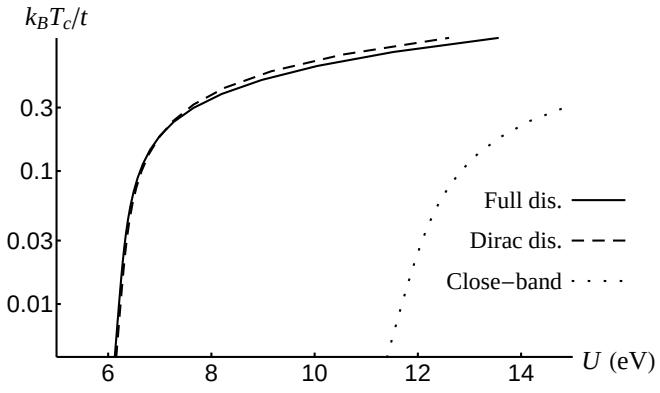

Figure 2.3: $T_c(U)$ for the contact-interaction approximation for $V_g = 0.1$ eV. Here, U is the effective interaction strength in eV units. The critical temperature T_c is expressed in units of the hopping parameter $t = 2.8$ eV. The solid line is obtained using the full dispersion, the dashed line using the Dirac approximation, and the dotted line using the close-band approximation.

structure does not represent a charge density wave, since e.g. Δ_{AA} describes the correlation between the A-sublattice sites in the two layers and not within a single layer.

We note that the same order parameter sublattice structure is associated with the broken inversion symmetry often thought [26] to be plausible in isolated graphene sheets. In that case, of course, the mean-field potential couples sites in the same layer. Broken inversion symmetry in an isolated graphene sheet is analogous to chiral symmetry breaking in elementary particle physics and is most likely to occur in neutral sheets without any carriers. Experiments appear to establish that spontaneous gaps do not in fact occur in single-layer graphene; angle-resolved photoemission experiments [27] are perhaps most conclusive in this respect. Spontaneous gaps do however appear [28] in neutral graphene sheets when a magnetic field is applied. It is sometimes argued [29] that the appearance of gaps in a field demonstrates that this order is barely avoided and latent even in the absence of a field. (For a contrary view see Ref. [30]). We will show that, because of their order parameter compatibility, latent sublattice-pseudospin chiral symmetry breaking order in a single layer is favorable for bilayer excitonic order. Although the presence of carriers always acts against order in an isolated graphene layer, we show that in the bilayer case it acts in favor of order provided that the carrier densities have opposite signs in opposite layers.

2.2.2 Full dispersion and close-band approximation

In this section we consider the influence of the full graphene dispersion and the close-band approximation on our result for the transition temperature. Since we are interested in qualitative effects, it is sufficient to consider the contact-interaction approximation results. We show in Fig. 2.3 the critical temperature T_c as a function of the effective interaction strength U for a fixed carrier Fermi energy $V_g = 0.1$ eV. The transition temperature T_c is scaled by the hopping strength $t = 2.8$ eV. Note that the interaction strength U in our model has the units of energy and that it is obtained as the continuum model interaction strength divided by the unit cell area. The solid line is obtained using the full graphene dispersion and the dashed line using the Dirac approximation. When we employ the close-band approximation, we obtain the dotted curve. Below we relate the parameter U to the contact-interaction approximation to the screened Coulomb interaction: $V^{\rm scr}(\mathbf{q}) \to U$, where $V^{\rm scr}(\mathbf{q})$ is the screened interlayer interaction matrix element.

When we want to employ the Dirac approximation, we are confronted with the fact that the theory has one free parameter, namely the value of the cutoff energy ξ that is needed to cure the ultra-violet divergence in the gap equation on which T_c will depend. In Sec. 2.4 we explain how to choose ξ, so that the results obtained using the Dirac dispersion and the full graphene dispersion overlap for temperatures corresponding to the low energies where the two dispersions do not differ noticeably. With this choice of ξ, we obtain the dashed curve in Fig. 2.3 for the Dirac model and the solid curve for the full π-band model. Note that the curves differ only slightly and then only for temperatures $k_B T > 0.2t$ at which the difference between the full graphene dispersion and Dirac dispersion becomes noticeable. Since the results obtained using the Dirac and full dispersions do not differ appreciably, we use the Dirac approximation for the contact-interaction phase diagrams shown in the next section. The dotted curve in Fig. 2.3 is the result of the close-band approximation, discussed further below.

Notice that the critical temperature is weakly dependent on interaction strength at large U and strongly-dependent on interaction strength at small U. The weak dependence occurs in the range of values where U is strong enough to produce order even when the carrier Fermi energy is set to zero, and the strong temperature-dependence in the range of U where order is assisted by the gate-driven Fermi surface nesting. To understand this observation consider the linearized T_c equation which is derived in detail in Sec. 2.4 and represented there by Eq. (2.28):

$$\frac{1}{U} = \frac{1}{2}\int_0^{\xi} d\epsilon \nu(\epsilon) \sum_{s=\pm 1} \frac{1 - 2n_f(\epsilon + sV_g)}{\epsilon + sV_g}. \tag{2.1}$$

Here, $\nu(\epsilon)$ is the isolated layer density-of-states per spin and valley per unit cell, $n_f(\epsilon)$ is the Fermi distribution function, and $s = -$ and $s = +$ terms correspond

respectively to close and remote band contributions. (The cross contributions between these two pairs vanish identically in the linearized gap equation.) When the carrier Fermi energy $V_g \to 0$ the two types of particle-hole pairs make identical contributions to the right-hand-side that decrease with temperature on the scale of the band width $\sim 3t$ and approach $1/2t$ for $T \to 0$. (The $1/t$ dependence for $T \to 0$ can be understood by noting that $\nu(\epsilon) \propto \epsilon/t^2$.) The linearized gap equation for $V_g \to 0$ has a solution only if $U/t \gtrsim 2$. For $V_g > 0$ the situation changes. The remote band contribution decreases slightly as these bands are separated from the Fermi energy. At the same time the close band contribution from small ϵ is enhanced, and in fact diverges logarithmically as $T \to 0$ because the density of states $\nu(V_g)$ is finite when the energy denominator vanishes. This is the Fermi surface nesting effect. Because the right-hand-side diverges, the linearized gap equation will always have a solution. On the other hand because the divergence is only logarithmic, the critical temperature will be extremely small if U is well below the strength at which coherence already appears for $V_g \to 0$. This observation accounts for the rapid drop in T_c at a particular interaction strength. Because the high-energy contributions of close and remote bands are nearly identical, the interaction strength required for a high critical temperature is badly underestimated if the remote bands are ignored. Note that the lowest temperature illustrated in Fig. 2.3 $\sim 0.003t$ is ~ 100K.

2.2.3 Phase diagrams

In this section we discuss the phase diagrams constructed from contact-interaction and separable potential approximations. We start with the former to gain physical insight and then compare with the latter. In Fig. 2.4, we show how the contact-interaction transition temperature versus effective interaction strength curve depends on carrier density. From right to left the three curves correspond to the carrier Fermi energies $V_g = (0, 0.2, 0.3)$ eV. In Fig. 2.4 we sees that T_c is an increasing function of both U and, for a fixed value of U, also an increasing function of V_g.

This figure provides a nice illustration of the separate roles played by the carriers (the conduction band states occupied by electrons and the valence band states occupied by holes) and higher energy states in forming the instability. The contribution of the carriers to the linearized gap equation scales with the density-of-states at the Fermi level, and hence with V_g. The higher energy contribution depends on the density-of-states far away from the Dirac point near the model's cut-off energy. For $V_g = 0$ only the remote band contribution is present and the system has a quantum critical point at $U_{\rm QCP} = 6.25$ eV which is indicated in Fig. 2.4 by the dot. Because of the $1/E$ weighting factor in the gap equation combined with the linear in E density-of-states of the Dirac model, this quantum critical point

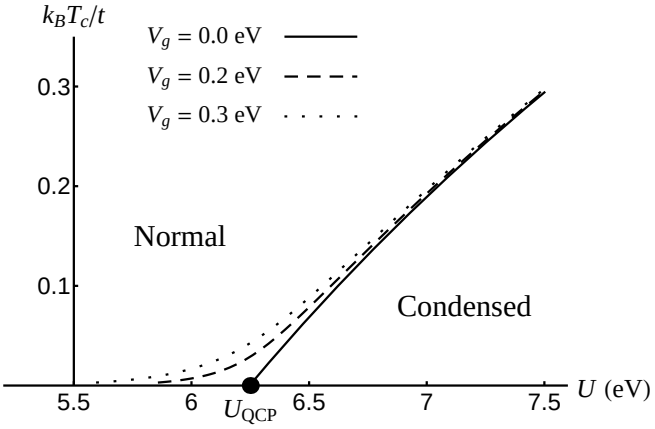

Figure 2.4: The scaled critical temperature T_c/t versus the effective interaction strength U in eV's for several values of the carrier Fermi energy V_g for the contact interaction approximation. From right to left the curves correspond to $V_g = (0, 0.2, 0.3)$ eV. The location of the normal state and condensed state are indicated. The quantum critical point is marked by a dot.

satisfies a Stoner-like criterion $\nu(\xi)U = 1$, where $\nu(\xi)$ is the density of states at the cutoff energy ξ. When $V_g \neq 0$, condensation occurs at any value of U, but not at low temperatures unless U is close to $U_{\rm QCP}$. The carrier contribution has a larger relative importance, and values of U that are substantially smaller than $U_{\rm QCP}$ can still yield high transition temperatures when V_g is pushed toward the largest physically realistic values ~ 0.3 eV. The high energy state contribution to the gap equation can be captured approximately by replacing the interaction among carriers by the effective interaction $U_{\rm eff} = U/(1 - U/U_{\rm QCP})$. We note that room temperature condensation corresponds to $k_BT_c \simeq 10^{-2}t$, which is a low-temperature on the scale of this phase diagram.

The T_c prediction based on the constant interaction model depends on a procedure for constructing an accurate value of U. We discuss such a procedure in Sec. 2.4 where we derive an expression in which U depends on Fermi energy V_g and interlayer distance d. We estimate U by performing the angular average of the screened interlayer Coulomb interaction over incoming and outgoing momenta restricted to the Fermi surface. The phase diagram thus obtained is shown in Fig. 2.5, where we plot the transition temperature T_c in Kelvin versus the interlayer distance d in nanometers. From right to left the curves correspond to carrier Fermi energies $V_g = (0.05, 0.1, 0.15)$ eV. We observe that T_c is a decreasing function of d, as expected. The behavior of T_c, which decreases as a function of V_g,

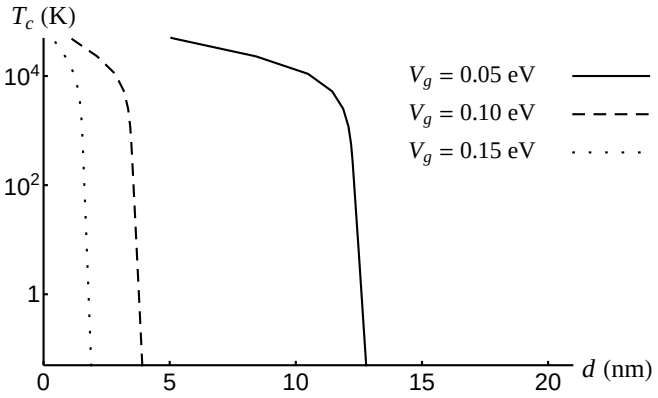

Figure 2.5: $T_c(d)$ critical curves calculated in the Dirac approximation with the transition temperature T_c in Kelvin versus the interlayer distance d in nanometer for the contact-interaction approximation. From right to left the curves correspond to $V_g = (0.05, 0.1, 0.15)$ eV. To the right of or above a curve the system is in the normal phase, to the left of or below a curve the system is in the condensed state.

is opposite to the behavior observed in Fig. 2.4 in which V_g was varied at fixed U. This behavior illustrated in Fig. 2.5 occurs because screening increases with density-of-states and hence with V_g, decreasing the value of U. Both the high transition temperatures and the trends illustrated in this figure are suspect, however, because static screening at the Fermi energy is irrelevant for the high energy states in the linearized gap equation. This conundrum demonstrates that reliable T_c estimates are challenging.

In Sec. 2.4 we show how to obtain the transition temperature T_c as a function of interlayer distance d and carrier Fermi energy V_g using a separable-potential approximation. In Fig. 2.6 we plot the resulting transition temperature T_c in Kelvin versus interlayer distance d in nanometer for three fixed carrier Fermi energies. The solid line corresponds to $V_g = 0.1$ meV, the dashed to $V_g = 0.3$ meV, and the dotted to $V_g = 1$ meV. The separable potential approximation is more realistic and at small d captures the expected increase of T_c with V_g. In Fig. 2.7 we plot the separable potential transition temperature T_c in Kelvin versus carrier Fermi energy V_g in meV for three fixed interlayer distances. The solid line corresponds to $d = 2$ nm, the dashed to $d = 4$ nm, and the dotted to $d = 8$ nm. Corresponding points are indicated by colored markers in the two Figs. 2.6 and 2.7. In Figs. 2.7 we see that T_c has a non-monotonic dependence on V_g. This behavior is due to a competition between the increase of screening (as in Fig. 2.5) and the increase

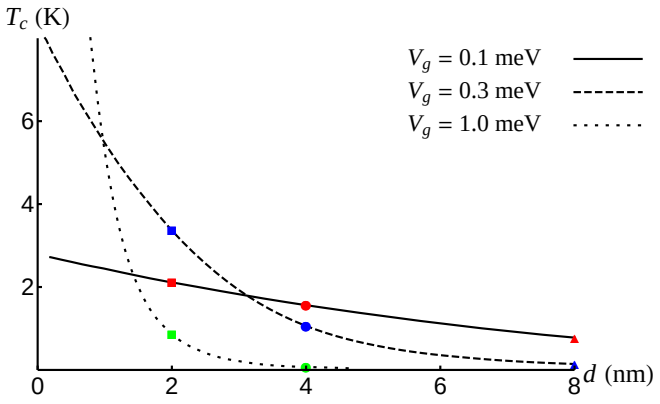

Figure 2.6: Transition temperature T_c in Kelvin versus interlayer distance d in nanometer for three fixed carrier Fermi energies for the separable-potential approximation. The solid line corresponds to $V_g = 0.1$ meV, the dashed to $V_g = 0.3$ meV, and the dotted to $V_g = 1$ meV. The points corresponding with Fig. 2.7 are indicated by the colored markers.

of the Fermi energy for larger V_g (as in Fig. 2.4). The maximum T_c for fixed d occurs for $k_F d \simeq 0.001$ and the height of the maximum goes as $1/d$. This conclusion is, however, also based on an approximation scheme that is unreliable for the high energy virtual states that appear in the gap equation. We note that in obtaining Figs. 2.6,2.7 we approximated the polarizibility of Graphene by a constant, neglecting the increase of Π with scattering momenta $q > 2k_F$. Including this dependence will lead to a suppression of the transition temperatures shown in Figs. 2.6 and 2.7.

As mentioned before, the use of a static screened Coulomb interaction is unreliable for high energy intermediate states in the gap equation. If we assume that our static screening estimate U is appropriate for $\epsilon < 2V_g$ and another estimate $\tilde{U}$ is appropriate for $\epsilon > 2V_g$, the gap equation becomes

$$\frac{1}{U} = \frac{\tilde{U}_c}{\tilde{U}_c - \tilde{U}} \frac{1}{2} \int_0^{2V_g} d\epsilon \nu(\epsilon) \sum_{s=\pm 1} \frac{1 - 2n_f(\epsilon + sV_g)}{\epsilon + sV_g}. \tag{2.2}$$

Here $\tilde{U}_c$ is the value of $\tilde{U}$ necessary to solve the $V_g = 0$ gap equation:

$$\frac{1}{\tilde{U}_c} = \nu(\xi), \tag{2.3}$$

where $\nu(\xi)$ is the density of states evaluated at the ultraviolet cutoff. In Fig. 2.8 we show the T_c versus d lines for several values of $\tilde{U}/\tilde{U}_c$. From left to right the curves correspond to $\tilde{U}/\tilde{U}_c = 0.5, 0.7, 0.9$.

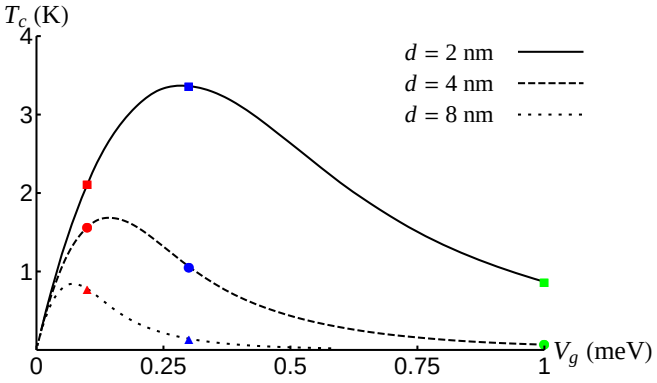

Figure 2.7: The critical lines of transition temperature T_c in Kelvin versus carrier Fermi energy V_g in milli-electronvolt for three fixed interlayer distances for the separable-potential approximation. The solid line corresponds to $d = 2$ nm, the dashed to $d = 4$ nm, and the dotted to $V_g = 8$ nm. The points corresponding with Fig. 2.6 are indicated by the colored markers.

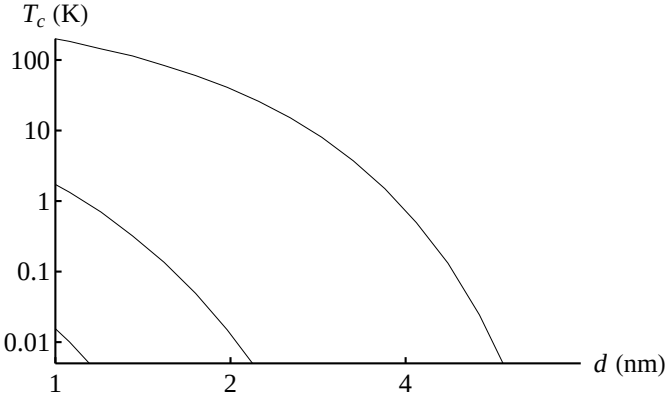

Figure 2.8: The critical lines of transition temperature T_c in Kelvin versus interlayer distance d in nanometer for Fermi energy $V_g = 0.1$ eV. From left to right the curves correspond to $\tilde{U}/\tilde{U}_c = 0.5, 0.7, 0.9$.

2.3 Discussion

In this chapter we have discussed a number of possible estimates for the critical temperature for exciton condensation in Coulomb coupled graphene layers in which a gate voltage has been applied to induce nesting between the conduction band Fermi level in the high-density layer and the valence band Fermi surface of the low-density layer. One of our main results concerns the sublattice structure of the inter-layer coherence order, which tends to be mainly off-diagonal in sublattice and opposite in sign for the AA and BB components. This structure is due to the momentum-direction dependence of inter-subband phases in both conduction and valence band states near the K and K' valleys in graphene. Similar observations have been made previously [21, 32]. These extra phases cause contributions to the anomalous inter-layer self-energy that are off-diagonal in sublattice to tend toward small values, yielding approximate cancelation. In a bilayer system this self-energy structure leads to compatible self-energy contributions from coherence between the bands with nested Fermi surfaces and from coherence between the two remote bands, the valence band of the high-density layer and the conduction band of the low-density layer. In addition the sublattice structure of bands remains consistent in graphene out to energies well beyond the Fermi energies of the nested bands, implying that contributions to interlayer coherence can be expected from high energy states in both carrier and remote bands.

Critical temperature estimates for coherent graphene bilayers are considerably complicated by the importance on the one-hand of screening by the gate-induced carriers at low energies and on the other hand of lattice scale correlations at high energies. For a two-dimensional system, mean-field theory overestimates the transition temperature to a superfluid and instead a KT-transition should be considered. For strong short-range interaction this consideration leads to a correction of the transition temperature by a factor ~ 3 [33]. We have reported on a number of T_c estimates that are based on momentum and frequency independent interactions. When appropriate values for the effective interaction strength are estimated based on low-energy screening considerations, large critical temperatures tend to occur at low carrier densities simply because screening is then minimized. These T_c estimates likely misrepresent trends as a function of carrier density, since screening at high energies is in fact not strongly influences by carriers. On the other hand, they do correctly, capture the fact that spontaneous coherence would appear even in systems without carriers if interactions were strong enough. In the contact interaction approximation the gap equation in the absence of carriers implies a Stoner-like criterion in which order appears for $U\nu(\xi) > 1$, where $\nu(\xi) \sim 1/(ta)^2$ is the density-of-states at the graphene Dirac model ultraviolet cut-off. The interaction assumes this form because the density-of-states in graphene increases linearly with energy over a very broad energy range. It is interesting to compare

this condition with the corresponding Stoner-like condition for density-wave states in a single-layer graphene sheet, $U\nu(\xi) > 1$ [34].

In the single-layer case, experiment seems to clearly indicate that the ground state is not a density-wave state, *i.e.* that $U < \nu(\xi)^{-1}$. On the other hand, the fact that density-wave states appear to occur in the presence of a magnetic field may suggest that the criterion is nearly met. If so, Fig. 2.8 shows that gating-induced Fermi surface nesting can enhance electron-hole pairing correlations and induce order at substantial temperatures.

The difference between our results and the prediction by Kharitonov *et al.* [22, 24] that T_c is maximally of the order of milliKelvins deserves further comment. Firstly, the value of the dielectric constant for the system we consider $\epsilon = 1$ differs from the value $\epsilon \simeq 4$ from Refs. [22] and [24]. This difference leads to a drastic difference in the prediction for T_c, as mentioned above. Furthermore, in their estimate of the upper limit for T_c, Kharitonov *et al.* set the width of the pairing region to zero, while we have shown that T_c depends exponentially of the ratio of this width to the Fermi energy. This distinction is important for the low Fermi energies we consider. A similar effect leads to the enhancement of the gap at zero temperature, as shown in Ref. [25]. None of these estimates include the effect of finite frequencies, which is likely to reduce screening effects and raise transition temperatures further.

In conclusion, we have determined the sublattice structure of the condensate and discussed the inter-layer coherence phase diagrams predicted by various estimates of interlayer interaction strengths. Our calculations make no assumptions about the sublattice structure of the condensate and take the full graphene dispersion into account. When contact interaction approximations are used high transition temperatures can occur. For the separable-potential approximation, we find transition temperatures of the order of Kelvins for the parameter range $V_g = 0.25 - 0.5$ meV and $d < 4$ nm. This results differs greatly from the result obtained by Kharitonov *et al.*[22, 24], that T_c is maximally of the order of milliKelvins, mainly because of the important role played in our calculations by states at high energy intermediate states with $\epsilon > 2V_g$. Careful consideration of the roles of retardation effects and coherence in reducing screening could increase T_c estimates further.

2.4 Methods

In this section we describe the methods we used to obtain the results shown in Sec. 2.2. We use a functional-integral approach since it provides a convenient starting point to account for non-mean-field effects.

2.4.1 Action of double-layer graphene

The coherent state path-integral representation for the partition function Z is given by

$$Z = \int d[\psi^*]d[\psi]e^{-(S_0[\psi^*,\psi]+S_I[\psi^*,\psi])/\hbar}, \tag{2.4}$$

where the integration is over all Grassmann-valued fields ψ^* and ψ that are anti-periodic on the interval $[0, \hbar\beta]$. The non-interacting action $S_0[\psi^*, \psi]$ in Eq. (2.4) is given by

$$S_0[\psi^*,\psi] = \sum_{\mathbf{k},\omega_n} \sum_{\alpha,\alpha',\sigma,\sigma'} \psi^*_{\alpha,\sigma}(\mathbf{k}, i\omega_n) \left[-\hbar G^{-1}_{0;\alpha,\sigma;\alpha',\sigma'}(\mathbf{k}, i\omega_n)\right] \psi_{\alpha',\sigma'}(\mathbf{k}, i\omega_n), \tag{2.5}$$

where the momenta are restricted to the first Brillouin zone, the $\omega_n = \pi(2n+1)/\hbar\beta$ are the fermionic Matsubara frequencies with $\beta = 1/k_BT$ the inverse temperature, $\alpha = A, B$ is the sublattice index, and $\sigma = t, b$ the which-layer pseudospin index. We ignore the electron spin for this moment, to return to it later. In the tight-binding model for graphene, the inverse noninteracting Green's function from Eq. (2.5) is

$$G^{-1}_{0;\sigma;\sigma'}(\mathbf{k}, i\omega_n) = -\frac{\delta_{\sigma,\sigma'}}{\hbar} \begin{pmatrix} -i\hbar\omega_n - \mu_\sigma & f(\mathbf{k}) \\ f^*(\mathbf{k}) & -i\hbar\omega_n - \mu_\sigma \end{pmatrix}, \tag{2.6}$$

where μ_σ is the chemical potential for the σ-layer, where $t = 2.8$ eV the nearest-neighbor hopping strength, and $f(\mathbf{k}) = -t\left(1 + e^{-i\mathbf{k}\cdot\mathbf{r}_1} + e^{-i\mathbf{k}\cdot(\mathbf{r}_1+\mathbf{r}_2)}\right)$, and $\mathbf{r}_1$ and $\mathbf{r}_2$ are the lattice vectors [13, 27]. The interaction contribution to the total action $S_I[\psi^*, \psi]$ in Eq. (2.4) describes the interaction between electrons via the Coulomb interaction and consists of both intra and interlayer terms. The effect of the intralayer terms is to renormalize the chemical potentials μ_σ and hopping strength t and to screen the interlayer interaction [31, 27]. These terms will be omitted in the remainder of this chapter. To account for them, we assume that the renormalized chemical potentials are such that in the normal state the top layer is electron and the bottom layer hole-like, with equal densities. The corresponding Fermi levels are denoted by the carrier Fermi energy V_g. To incorporate the effect of screening by density fluctuations, we use the screened instead of the bare Coulomb interaction as the interlayer interaction. Then, $S_I[\psi^*, \psi]$ consists only of interlayer terms and is given by

$$S_I[\psi^*,\psi] = \int_0^{\hbar\beta} d\tau \sum_{\mathbf{r},\mathbf{r}'} \sum_{\alpha,\alpha'} V^{\mathrm{scr}}(\mathbf{r}-\mathbf{r}')\psi^*_{\alpha,t}(\mathbf{r},\tau)\psi^*_{\alpha',b}(\mathbf{r}',\tau)\psi_{\alpha',b}(\mathbf{r}',\tau)\psi_{\alpha,t}(\mathbf{r},\tau), \tag{2.7}$$

where the position summations are over all N unit cell positions. Since the transition depends only weakly on the precise stacking of the layers [15], we make the simplifying assumption that the stacking is such that the A-sites (B-sites) of the top layer lie directly above the A-sites (B-sites) of the bottom layer.

The statically screened interlayer Coulomb interaction is given by

$$V^{\mathrm{scr}}(\mathbf{q}) = \sum_{\mathbf{r}} V^{\mathrm{scr}}(\mathbf{r}) e^{i\mathbf{q}\cdot\mathbf{r}} = \frac{V(q)e^{-qd}}{1 - 2V(q)\Pi(q) + (1 - e^{-2qd})\, V^2(q)\Pi^2(q)}, \tag{2.8}$$

where

$$V(q) = \frac{e^2}{4\pi\epsilon_0\epsilon} \frac{1}{A} \frac{2\pi}{q}, \tag{2.9}$$

is the bare interaction [14], ϵ_0 is the permittivity of the vacuum, ϵ is the dielectric constant of the surrounding medium which we take to be air with $\epsilon = 1$, d is the distance between the graphene layers, and $A = 3\sqrt{3}a^2/2$ the area of the graphene unit cell, with $a = 0.142$ nm the nearest-neighbor distance between the carbon atoms. The polarizability Π is given in the Dirac approximation by $\Pi(q) = -4\nu(V_g)$ for $q < 2k_F$
which is the momentum range relevant for the carrier-band contribution to the gap equation. The factor 4 is due to spin and valley degeneracy, and the density of states is $\nu(V_g) = (A/2\pi)V_g/(3at/2)^2$ [35]. This form of $S_I[\psi^*, \psi]$ is valid in the long-wavelength approximation, where the interlayer Coulomb interaction is independent of the sublattice index. It will be convenient to introduce the dimensionless momentum variable $y = qd$, so that the dimensionless interaction $\tilde{V}^{\mathrm{scr}}(y)$ becomes

$$\tilde{V}^{\mathrm{scr}}(y) \equiv \frac{1}{V(1/d)} V^{\mathrm{scr}}(y/d) = \frac{e^{-y}}{y + 2\gamma(\epsilon)k_F d + (1 - e^{-2y})\,(\gamma(\epsilon)k_F d)^2/y}, \tag{2.10}$$

where we defined

$$-qV(q)\Pi(q) \equiv \gamma(\epsilon)k_F = 9.66k_F/\epsilon. \tag{2.11}$$

2.4.2 Derivation of the effective action

Since the condensed state is a broken symmetry state, we cannot resort to perturbation theory to determine T_c. Instead, we perform a so-called Hubbard-Stratonovich transformation to obtain an effective action in terms of the order parameter for exciton condensation. Concretely, this procedure entails multiplying the partition function Z from Eq. (2.4) by a Gaussian functional integral with value unity over the order parameter $\Delta_{\alpha,\alpha'}(\mathbf{r}, \mathbf{r}', \tau)$ that is on average given by $V^{\mathrm{scr}}(\mathbf{r} - \mathbf{r}')\langle\psi^*_{t,\alpha}(\mathbf{r}, \tau)\psi_{b,\alpha'}(\mathbf{r}', \tau)\rangle$. By an appropriate choice of the parameters in this integral, the interacting action $S_I[\psi^*, \psi]$ from Eq. (2.7) can be canceled from the argument of the exponent in the functional integral Eq. (2.4). Then, the integral over the electron fields can be performed analytically and an effective action

is obtained in terms of the order parameter, which is given by

$$S_{\text{eff}}[\Delta^*,\Delta] = -\hbar \text{Tr}\log\left(-\hat{G}^{-1}\right) + \frac{\hbar\beta}{N}\sum_{\mathbf{k},\mathbf{k}',\mathbf{K},\omega_m}\sum_{\alpha,\alpha'}\left(\frac{1}{V^{\text{scr}}}\right)(\mathbf{k}-\mathbf{k}')\,\Delta^*_{\alpha,\alpha'}(\mathbf{k},\mathbf{k}+\mathbf{K},i\omega_m)\Delta_{\alpha,\alpha'}(\mathbf{k}',\mathbf{k}'+\mathbf{K},i\omega_m), \tag{2.12}$$

where $\omega_m = 2\pi m/\hbar\beta$ are now the bosonic Matsubara frequencies, $\left(\frac{1}{V^{\text{scr}}}\right)(\mathbf{k})$ is the Fourier transform of the inverse interaction in position space $1/V^{\text{scr}}(\mathbf{r}-\mathbf{r}')$ and where $\hat{G}^{-1} = \hat{G}_0^{-1} - \hat{\Sigma}$ with the electron selfenergy given by

$$\hbar\Sigma_{\alpha,\sigma;\alpha',\sigma'}(\mathbf{k},i\omega_n;\mathbf{k}',i\omega_{n'}) = -\left[\delta_{\sigma,b}\delta_{\sigma',t}\Delta_{\alpha',\alpha}(\mathbf{k}',\mathbf{k},i\omega_n - i\omega_{n'}) + \delta_{\sigma,t}\delta_{\sigma',b}\Delta^*_{\alpha,\alpha'}(\mathbf{k},\mathbf{k}',i\omega_{n'} - i\omega_n)\right]. \tag{2.13}$$

We determine T_c for a second-order phase transition to the condensed state by expanding the effective action $S_{\text{eff}}[\Delta^*,\Delta]$ in Eq. (2.12) to second order in the order parameter Δ^* and Δ. Since we expect the order parameter to be translationally invariant in space and time, we only consider the contribution of the zero frequency and zero center-of-mass momentum components of the order parameter Δ^* and Δ to the effective action $S_{\text{eff}}[\Delta^*,\Delta]$ in Eq. (2.12). For notational simplicity, we define the shorthand $\Delta_{\alpha,\alpha'}(\mathbf{k},\mathbf{k},0) = \Delta_{\alpha,\alpha'}(\mathbf{k})$. This procedure yields

$$S_{\text{eff}}[\Delta^*,\Delta] = \hbar\beta\sum_{\mathbf{k},\mathbf{k}'}\sum_{\alpha_1,\alpha_2,\alpha_3,\alpha_4}\Delta^*_{\alpha_1,\alpha_2}(\mathbf{k})M_{\alpha_1,\alpha_2,\alpha_3,\alpha_4}(\mathbf{k},\mathbf{k}')\Delta_{\alpha_3,\alpha_4}(\mathbf{k}'), \tag{2.14}$$

where

$$M_{\alpha_1,\alpha_2,\alpha_3,\alpha_4}(\mathbf{k},\mathbf{k}') = \frac{1}{N}\delta_{\alpha_1,\alpha_3}\delta_{\alpha_2,\alpha_4}\left(\frac{1}{V^{\text{scr}}}\right)(\mathbf{k}-\mathbf{k}') - \delta_{\mathbf{k},\mathbf{k}'}\mathbf{B}_{\alpha_1,\alpha_2,\alpha_3,\alpha_4}(\mathbf{k}), \tag{2.15}$$

with the interlayer polarization $\mathbf{B}$ given by

$$\begin{aligned}\mathbf{B}_{\alpha_1,\alpha_2,\alpha_3,\alpha_4}(\mathbf{k}) &= -\frac{1}{\hbar^2\beta}\sum_{\omega_n}G_{0;\alpha_3,t;\alpha_1,t}(\mathbf{k},i\omega_n)G_{0;\alpha_2,b;\alpha_4,b}(\mathbf{k},i\omega_n)\\ &= \frac{1}{4}\begin{pmatrix} B_0 & e^{i\phi}B_1 & -e^{-i\phi}B_1 & B_2\\ e^{-i\phi}B_1 & B_0 & e^{-2i\phi}B_2 & -e^{-i\phi}B_1\\ -e^{i\phi}B_1 & e^{2i\phi}B_2 & B_0 & e^{i\phi}B_1\\ B_2 & -e^{i\phi}B_1 & e^{-i\phi}B_1 & B_0\end{pmatrix}.\end{aligned} \tag{2.16}$$

Here we dropped the $\mathbf{k}$ dependence of the B_i, defined $\phi = \arg[f(\mathbf{k})]$, and

$$B_0 = 2B(+,+) + B(-,+) + B(+,-) \tag{2.17}$$

$$B_1 = B(-,+) - B(+,-) \tag{2.18}$$

$$B_2 = 2B(+,+) - B(-,+) - B(+,-). \tag{2.19}$$

Moreover

$$B(s_t, s_b) = -\frac{n_f\left(\epsilon_{s_t,t}(\mathbf{k})\right) - n_f\left(\epsilon_{s_b,b}(\mathbf{k})\right)}{\epsilon_{s_t,t}(\mathbf{k}) - \epsilon_{s_b,b}(\mathbf{k})}, \tag{2.20}$$

with $s_t, s_b = \pm 1$ and top and bottom layer dispersions

$$\epsilon_{s,t}(\mathbf{k}) = s|f(\mathbf{k})| + V_g \quad \text{and} \quad \epsilon_{s,b}(\mathbf{k}) = s|f(\mathbf{k})| - V_g, \tag{2.21}$$

with $s = \pm 1$. The letter B is chosen in Eqs. (2.16,2.20) because Eq. (2.20) is the expression of a bubble diagram, which describes screening by electron-hole pairs. We note that when we perform a particle-hole transformation in the (hole-like) top layer, the numerator of the right-hand side of Eq. (2.20) becomes $1 - n_f(\epsilon_{s_1,t}(\mathbf{k})) - n_f(\epsilon_{s_2,b}(\mathbf{k}))$, and we obtain the familiar expression for the ladder diagram from BCS theory.

Now, we comment on the importance of the real electron spin. Each independent fermion species contributes to the screening of the Coulomb interaction. Therefore, a factor of two due to the spin degeneracy should be included in the expression for the polarizability $\Pi(q)$, as we did above. The interlayer Coulomb interaction is to a very good approximation independent of spin, and we need to consider how the effective action Eq. (2.14) changes if we include the electron spin, in Eq. (2.5) and Eq. (2.7). The electron spin can be incorporated in our formalism by extending the definition of α to include both the sublattice and spin quantum numbers, so that the order parameter has 16 components. The noninteracting Greens functions in the expression for $\mathbf{B}$ in Eq. (2.16) are diagonal in spin, so that the same is true for $\mathbf{B}$ in Eq. (2.16) and M in Eq. (2.15). Thus, we find that the contributions to the effective action of the 4 spin pairing channels are decoupled and thus we find four identical T_c equations, one for each channel. Thus, it is correct for the determination of the phase diagram to ignore the electron spin in our formalism.

2.4.3 Derivation of the linearized gap equation

The transition temperature T_c is now given by the maximum temperature for which the matrix M defined in Eq. (2.15) has a zero eigenvalue, or equivalently the maximal temperature for which for all $\mathbf{k}$, α_1, and α_2 we have

$$\sum_{\mathbf{k}'} \sum_{\alpha_3,\alpha_4} M_{\alpha_1,\alpha_2,\alpha_3,\alpha_4}(\mathbf{k},\mathbf{k}')\Delta_{\alpha_3,\alpha_4}(\mathbf{k}') = 0. \tag{2.22}$$

To get rid of the Fourier transform of the reciprocal interaction, we multiply with the interaction $V^{\mathrm{scr}}(\mathbf{k}'' - \mathbf{k})$ and sum over $\mathbf{k}$ to obtain the gap equation

$$\Delta_{\alpha_1,\alpha_2}(\mathbf{k}) = \frac{1}{N} \sum_{\mathbf{k}',\alpha_3,\alpha_4} V^{\mathrm{scr}}(\mathbf{k} - \mathbf{k}')\mathbf{B}_{\alpha_1,\alpha_2,\alpha_3,\alpha_4}(\mathbf{k}')\Delta_{\alpha_3,\alpha_4}(\mathbf{k}'). \tag{2.23}$$

Below, we use two methods to find approximate solutions of Eq. (2.23), namely by modeling the interaction as a contact interaction and using the separable-potential approximation.

We remark that the screened interaction in Eq. (2.23) should in first instance be evaluated at frequency $\omega = \epsilon_{\mathbf{k}} - \epsilon_{\mathbf{k}'}$. The frequency and wavevector arguments which appear in the remote band part of this integral are ones for which our static screening approximation is not reliable. It is, however, not immediately clear how to improve on the approximation we employ because of corrections to the simple RPA screening function and the role of σ and σ^* bands that we do not consider. We therefore choose to use the static RPA screening functions in this chapter, but remain cognizant of limitations in the predictive power of our (or any other) semi-analytic T_c calculation.

2.4.4 Approximation 1: Contact interaction

The contact-interaction approximation is rather crude for the Coulomb interaction and can only be used to obtain qualitative results for the phase diagram and the condensate structure. In this approximation, we replace the interaction matrix elements in momentum space $V^{\mathrm{scr}}(\mathbf{k}-\mathbf{k}')$ in Eq. (2.23) by an effective strength U which is an appropriate average of V^{scr} over its arguments. It then follows that the components of the order parameter $\Delta_{\alpha_1,\alpha_2}(\mathbf{k})$ are independent of momentum. This approach was used previously for this system [21, 25]. However, because the contact interaction averages out the structure of the Coulomb interaction, one may only expect to obtain qualitative results using this approximation. Setting $V^{\mathrm{scr}}(\mathbf{k}-\mathbf{k}') = U$ in Eq. (2.23), we obtain a 4×4 matrix equation

$$\Delta_{\alpha_1,\alpha_2} = \frac{U}{N}\sum_{\mathbf{k}',\alpha_3,\alpha_4} \mathbf{B}_{\alpha_1,\alpha_2,\alpha_3,\alpha_4}(\mathbf{k}')\Delta_{\alpha_3,\alpha_4}, \tag{2.24}$$

so that the critical condition is that the 4×4 matrix $\mathbf{\Pi} = (U/N)\sum_{\mathbf{k}}\mathbf{B}(\mathbf{k})$ has eigenvalue 1. We have that

$$\mathbf{\Pi} = \frac{U}{4N}\begin{pmatrix} \Pi_{0,0} & \Pi_{1,1} & -\Pi_{1,1} & \Pi_{2,0} \\ \Pi_{1,1} & \Pi_{0,0} & \Pi_{2,2} & -\Pi_{1,1} \\ -\Pi_{1,1} & \Pi_{2,2} & \Pi_{0,0} & \Pi_{1,1} \\ \Pi_{2,0} & -\Pi_{1,1} & \Pi_{1,1} & \Pi_{0,0} \end{pmatrix}, \tag{2.25}$$

where we defined

$$\Pi_{i,l} = \frac{1}{N}\sum_{\mathbf{k}} B_i(\mathbf{k})\cos\{l\arg[f(\mathbf{k})]\}. \tag{2.26}$$

The eigenvalues of Π can be computed in closed form. Equating the largest eigenvalue with 1 yields the following T_c equation:

$$1 = \frac{U}{8}\left(2\Pi_{0,0} - \Pi_{2,0} - \Pi_{2,2} + \sqrt{16\Pi_{1,1}^2 + (\Pi_{2,0} - \Pi_{2,2})^2}\right). \tag{2.27}$$

We remark that the eigenvector corresponding to this largest eigenvalue has opposite (A, A) and (B, B) components, a result previously found in a model without intersublattice components for the order parameter $\Delta_{A,B}$ and $\Delta_{B,A}$ [21].

Dirac approximation

It is interesting to consider the result for the critical temperature Eq. (2.27) in the Dirac approximation and compare its solution to the critical temperature obtained using the full dispersion. The linear Dirac spectrum is often used as an approximation to the dispersion of graphene, where one sets $f(\mathbf{k}) = (3at/2)(k_x + ik_y)$. Then, the $B_i(\mathbf{k})$ depend only on the length of $\mathbf{k}$ and it follows that the $\Pi_{i,l}$ vanish for nonzero angular momentum l. Then, Eq. (2.27) can be written as

$$1 = \frac{U}{2N}\sum_{\mathbf{k}}\left[B(-,+) \;+\; B(+,-)\right] = \frac{U}{2}\int_0^{\xi} d\epsilon\nu(\epsilon)\sum_{s=\pm 1}\frac{1 - 2n_f(\epsilon + sV_g)}{\epsilon + sV_g}, \tag{2.28}$$

where we used that $n_f(-\epsilon) = 1 - n_f(\epsilon)$, a factor 2 was added in the second line to account for the presence of the valley degeneracy in the momentum integral, and ξ is some high-energy cutoff, on which we comment below. Again, $\nu(\epsilon)$ is the density of states for a single valley and spin species. The equation Eq. (2.28) describes the situation of band-diagonal pairing, as described previously [25], in which there is no pairing between the close-lying conduction bands, and far-laying valance bands. Following an approach used to analyze superconductivity in single-layer graphene [36], we can evaluate Eq. (2.28) further and obtain

$$\frac{y}{\lambda} + x\int_{y-x}^{y+x} dx' \frac{\tanh(x')}{x'} - \log(\cosh(y-x)\cosh(y+x)) = 2x\int_0^x dx' \frac{\tanh(x')}{x'} - 2\log\cosh(x), \tag{2.29}$$

with $x = \beta V_g/2$, $y = \beta\xi/2$ and where the dimensionless coupling constant is given by $\lambda = U\nu(\xi)/2$. The system has a quantum critical point only for $U_{\mathrm{QCP}} = 6.25$ eV and $V_g = 0$ where $\lambda = 1/2$ and $U_{\mathrm{QCP}}\nu(\xi) = 1$, which is a Stoner criterion for the spontaneous polarization of the valence bands in the two layers which are filled for $V_g = 0$. An important point is that the solution of Eq. (2.29) depends on the high- energy cutoff ξ, and only when we choose a particular value for ξ, are we able to compare the results obtained using the Dirac approximation and the full dispersion. We find this value of ξ by demanding that the interaction strength

U_{QCP} at which the quantum critical point occurs for the Dirac approximation in Eq. (2.29) coincides with the value of U_{QCP} obtained from Eq. (2.27). This equality leads to the equation

$$\nu(\xi) = \frac{1}{2N} \sum_{\mathbf{k}} \frac{1}{|f(\mathbf{k})|}, \tag{2.30}$$

which yields $\xi = 6.83$ eV. The results obtained using this procedure are discussed in Sec. 2.2 and shown in Fig. 2.3. When $y \gg x \gg 1$ we may approximate Eq. (2.29) to obtain a BCS-like result for the transition temperature

$$k_b T_c = \frac{V_g}{2} \frac{\sqrt{\xi - V_g}}{\sqrt{\xi + V_g}} \exp\left(-\frac{1}{U\nu(V_g)} + \frac{\xi}{V_g} + C - 1 \right), \tag{2.31}$$

where $C = \lim_{R\to\infty} \left\{ \int_0^R [\tanh(x)/x] dx - \log(R) \right\} = 0.82$. Apart from the usual BCS term in the exponent $-1/U\nu(V_g)$, we also find an additional term which scales as the length of the pairing region ξ over the Fermi energy V_g. This effect will also influence the T_c found in our separable-potential approximation and one of the reasons that we predict a higher value of T_c for small Fermi energies as compared to Refs. [22] and [24]. We finally note that the gap equation on the close-band approximation can be obtained from Eq. (2.28) by only taking the $s = -1$ term of the summation. The close-band results are also discussed discussed in Sec. 2.2 and shown in Fig. 2.3. We note that an equation similar to Eq. (2.31) was found in Ref. [25] for the magnitude of the gap at zero temperature.

Estimation of U

By estimating the effective interaction strength U as a function of the interlayer distance d, we may transform the horizontal axis in Fig. 2.4 and obtain the phase diagram with the transition temperature versus d. We estimate U by evaluating the angular average of the screened interaction Eq. (2.8) over the incoming and outgoing momenta restricted to the Fermi surface, $\mathbf{k}$ and $\mathbf{k}'$, respectively

$$U(d) = \frac{\int_{\epsilon_{\mathbf{k}},\epsilon_{\mathbf{k}'}=V_g} d\mathbf{k} d\mathbf{k}' V^{\mathrm{scr}}(\mathbf{k}-\mathbf{k}')}{\int_{\epsilon_{\mathbf{k}},\epsilon_{\mathbf{k}'}=V_g} d\mathbf{k} d\mathbf{k}'} = \frac{1}{\pi} \int_0^{\pi} d\phi V^{\mathrm{scr}}\left(2k_F \sin(\phi)\right), \tag{2.32}$$

which can be easily evaluated numerically.

2.4.5 Approximation 2: Separable approximation

In order to obtain a quantitative prediction for the mean-field transition temperature, it is not sufficient to approximate the screened Coulomb interaction by a contact interaction. Instead, we will approximate the screened Coulomb interaction by a function which is separable in the incoming and outgoing momenta, as

was also done in Ref. [25] to determine the gap at zero temperature. We show below how to implement this procedure concretely. We will consider s-wave solutions for the gap functions of the form

$$\Delta_{\alpha_1,\alpha_2}(y) = \Delta_{\alpha_1,\alpha_2}(y)e^{il_{\alpha_1,\alpha_2}\phi}, \tag{2.33}$$

where ϕ is the azimuthal angle of $\mathbf{k}$, the l_{α_1,α_2} is the angular momentum quantum number, and we transformed to the dimensionless momenta $y = kd$. Since we showed that the influence of the full dispersion is small, we continue in the Dirac approximation, where we may rewrite the gap equation Eq. (2.23) as

$$\Delta_{\alpha_1,\alpha_2}(y) = \frac{A}{2\pi d^2}\sum_{\alpha_3,\alpha_4}\int y'dy' V^{\mathrm{av}}_{\alpha_1,\alpha_2,\alpha_3,\alpha_4}(y,y')\mathbf{B}^R_{\alpha_1,\alpha_2,\alpha_3,\alpha_4}(y')\Delta_{\alpha_3,\alpha_4}(y'), \tag{2.34}$$

where we defined the angular averaged interaction

$$V^{\mathrm{av}}_{\alpha_1,\alpha_2,\alpha_3,\alpha_4}(y,y') = \frac{1}{2\pi}\int d\phi' e^{i(l_{\alpha_3,\alpha_4}\phi' - l_{\alpha_1,\alpha_2}\phi)}e^{in_{\alpha_1,\alpha_2,\alpha_3,\alpha_4}\phi'} \times V^{\mathrm{scr}}\left(\sqrt{y^2+y'^2-2\cos(\phi'-\phi)yy'}\right), \tag{2.35}$$

where we anticipated the fact that the $l_{\alpha,\alpha'}$ will be chosen such that the right hand side of Eq. (2.35) does not depend on ϕ. We furthermore defined the radial part of $\mathbf{B}$ from Eq. (2.16) as $\mathbf{B}^R$ in the following way

$$\mathbf{B}_{\alpha_1,\alpha_2,\alpha_3,\alpha_4}(\mathbf{y}/d) = \mathbf{B}^R_{\alpha_1,\alpha_2,\alpha_3,\alpha_4}(y)e^{in_{\alpha_1,\alpha_2,\alpha_3,\alpha_4}\phi}, \tag{2.36}$$

where $\mathbf{B}$ should be considered in the Dirac approximation and the values of the integers $n_{\alpha_1,\alpha_2,\alpha_3,\alpha_4}$ can be read of from the expression for $\mathbf{B}$ in Eq. (2.16). Note that we did not include an extra factor 2 due to the valley degeneracy, since we assume that there is no intervalley scattering. Then, we may argue that each valley pairing channel leads to an equivalent gap equation, and we may ignore the valley label, similar as we did above for the electron spin. The right-hand side of Eq. (2.34) should be independent of ϕ, which is the case when

$$l_{A,A} = l_{B,B} = l_0, \quad l_{A,B} = l_0 - 1, \quad \text{and} \quad l_{B,A} = l_0 + 1. \tag{2.37}$$

for some integer l_0. Then, the gap equation Eq. (2.34) can be written in a simplified form as

$$\Delta_{\alpha_1,\alpha_2}(y) = \frac{\gamma(\epsilon)}{4}\sum_{\alpha_3,\alpha_4}\int y'dy'\tilde{V}^{\mathrm{av}}_{l_{\alpha_1,\alpha_2}}(y,y')\tilde{\mathbf{B}}_{\alpha_1,\alpha_2,\alpha_3,\alpha_4}(y')\Delta_{\alpha_3,\alpha_4}(y'), \tag{2.38}$$

where

$$\tilde{V}^{\mathrm{av}}_l(y,y') = \frac{1}{2\pi}\int d\phi\cos(l\phi)\tilde{V}^{\mathrm{scr}}\left(\sqrt{y^2+y'^2-2\cos(\phi)yy'}\right), \tag{2.39}$$

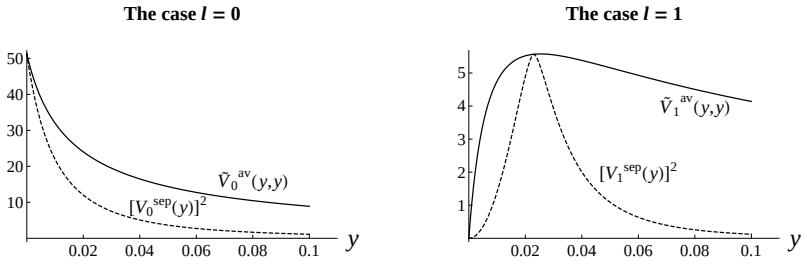

Figure 2.9: We plot $\tilde{V}_l^{\text{av}}(y,y)$ and $[V_l^{\text{sep}}(y)]^2$ by the solid and dashed line, respectively, for the cases $l=0$ (left graph) and $l=1$ (right graph).

where $\tilde{V}^{\text{scr}}(y)$ was defined above in Eq. (2.10). We defined $\tilde{\mathbf{B}}^R$ as dimensionless form of $\mathbf{B}^R$, i.e. with the $B(s_1,s_2)$ from Eq. (2.20) replaced by the dimensionless $\tilde{B}$ defined by

$$\tilde{B}(s_t,s_b) = -\frac{\frac{1}{1+\exp[\beta'(s_t y - k_F d)]} - \frac{1}{1+\exp[\beta'(s_b y + k_F d)]}}{(s_t y - k_F d) - (s_b y + k_F d)}, \tag{2.40}$$

with $\beta' = \beta\hbar v_f/d$. From these expressions we obtain that for a *fixed* value of $k_F d$ the transition temperature goes as $1/d$ and increases linearly with the Fermi momentum k_F and the carrier Fermi energy V_g. Up to this point, our rewriting of the gap equation Eq. (2.23) is exact, under the ansatz Eq. (2.33). In order to be able to obtain numerical results, we now approximate $\tilde{V}_l^{\text{av}}(y,y')$ by a function that is separable in y and y'. This approximation amounts to choosing a function V^{sep} such that

$$\tilde{V}_l^{\text{av}}(y,y') \simeq V_l^{\text{sep}}(y) V_l^{\text{sep}}(y'). \tag{2.41}$$

From Eq. (2.38) we see that the y dependence of $\Delta_{\alpha_1,\alpha_2}(y)$ in this case goes as $V^{\text{sep}}_{l_{\alpha_1,\alpha_2}}(y)$ so that it natural to define $\Delta_{\alpha_1,\alpha_2}(y) = V^{\text{sep}}_{l_{\alpha_1,\alpha_2}}(y)\Delta'_{\alpha_1,\alpha_2}$. The gap equation Eq. (2.38) thus becomes a 4×4 matrix equation independent of y

$$\Delta'_{\alpha_1,\alpha_2} = \frac{\gamma(\epsilon)}{4}\sum_{\alpha_3,\alpha_4}\int y'dy' V^{\text{sep}}_{l_{\alpha_1,\alpha_2}}(y') V^{\text{sep}}_{l_{\alpha_3,\alpha_4}}(y')\tilde{\mathbf{B}}_{\alpha_1,\alpha_2,\alpha_3,\alpha_4}(y')\Delta'_{\alpha_3,\alpha_4}. \tag{2.42}$$

After choosing a functional form of V_l^{sep} we can find the transition temperature as the largest temperature for which Eq. (2.42) has a solution. For our purposes, it is sufficient to choose the following form of V_l^{sep}

$$V_l^{\text{sep}}(y) = \frac{V_l^{\text{av}}\left(y, y_l^{\text{ref}}\right)}{\sqrt{V_l^{\text{av}}\left(y_l^{\text{ref}}, y_l^{\text{ref}}\right)}}, \tag{2.43}$$

where y_l^{ref} is some reference momentum. It is natural to choose y_l^{ref} as the position of the maximum of $V_l^{\mathrm{av}}(y,y)$, which yields

$$y_{l=0}^{\mathrm{ref}} = 0 \quad \text{and} \quad y_{l=1}^{\mathrm{ref}} \simeq 2.61\gamma(\epsilon)k_F d. \tag{2.44}$$

To gain insight in the effect of this approximation, we plot in Fig. 2.9 the functions $\tilde{V}_l^{\mathrm{av}}(y,y)$ and $[V_l^{\mathrm{sep}}(y)]^2$, which would fall on top of each other if the approximation Eq. (2.41) were exact. In Fig. 2.9 we plot $\tilde{V}_l^{\mathrm{av}}(y,y)$ and $[V_l^{\mathrm{sep}}(y)]^2$ by the solid and dashed line, respectively, for the cases $l = 0$ (left graph) and $l = 1$ (right graph). Since $[V_l^{\mathrm{sep}}(y)]^2$ is always lower than $\tilde{V}_l^{\mathrm{av}}(y,y)$ one expects that the transition temperatures found in our analysis are a lower boundary for the mean-field transition temperature for exciton condensation.

Chapter 3

Probing the topological exciton condensate via Coulomb drag

The onset of exciton condensation in a topological insulator thin film was recently predicted. We calculate the critical temperature for this transition, taking into account screening effects. Furthermore, we show that the proximity to this transition can be probed by measuring the Coulomb drag resistivity between the surfaces of the thin film as a function of temperature. This resistivity shows an upturn upon approaching the exciton-condensed state.

3.1 Introduction

Recently, there has been great experimental and theoretical interest in a new class of materials called topological insulators (TIs) [37]. These materials combine, for a particular doping level, an insulating behavior in the bulk with topologically protected conducting surface states that are described by a two-dimensional (2D) Dirac-Weyl Hamiltonian. When the surfaces of a TI film are independently doped or gated, electrons can be induced in one layer and holes in the other. In 2009, Seradjeh *et al.* [38] predicted that such a system can support a so-called topological exciton condensate. Electrons in one layer combine with holes in the other layer to form excitons, which condense for low enough temperatures. One of the interesting features of this state is that it supports vortices in the order parameter: these vortices carry a fractional charge $\pm e/2$ [38].

In a drag experiment with a two-layer system a current is applied through one of the layers (the drive or active layer) and an induced voltage is measured in the other layer (the passive layer). The drag resistivity ρ_{D} is defined as the ratio between the electric field in the passive layer and the current density in the

This chapter is published in Physical Review Letters: Probing the topological exciton condensate via Coulomb drag, M. P. Mink, H. T. C. Stoof, R.A. Duine, Marco Polini, G. Vignale, Phys. Rev. Lett **108**, 186402 (2012).

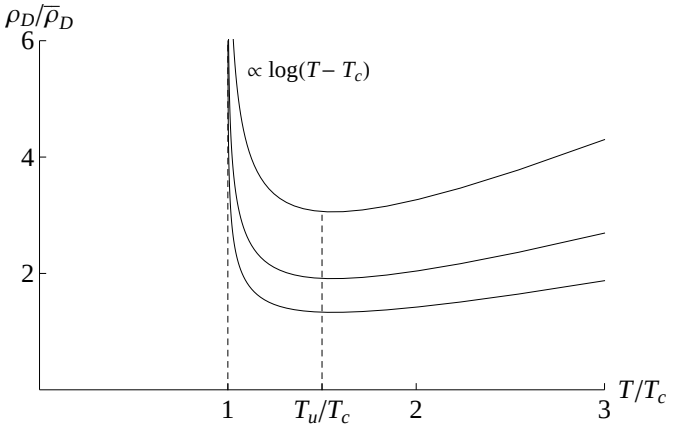

Figure 3.1: The drag resistivity $\rho_{\rm D}$ [in units of $\bar{\rho}_{\rm D} = (\nu_0 U)^2\hbar/4e^2$, with ν_0 the density of states at the Fermi level and U the interlayer interaction strength] calculated from Eq. (3.3) as a function of the reduced temperature $T/T_{\rm c}$. With this choice of units $\rho_{\rm D}/\bar{\rho}_{\rm D}$ depends on two parameters – the chemical potential μ and the critical temperature $T_{\rm c}$ – which implicitly determine the interaction strength U in Eq. (3.1). The curves correspond to the case of equal chemical potentials in the two layers ($\mu = 0.04$ eV). From top to bottom the critical temperatures are $T_{\rm c}/T_{\rm F} = (1/150, 1/200, 1/250)$. The vertical dashed lines are located at $T = T_{\rm c}$ (left) and at the "upturn" temperature scale (see text) $T = T_{\rm u}$ (right).

active layer. In the absence of an ordered state, the low-temperature behavior of the drag resistivity is $\rho_{\rm D} \propto T^2$ [or $T^2 \log(T)$ for a 2D system with short-range interactions]. This quadratic temperature dependence was first observed in 1991 by Gramila *et al.* [2] and is a hall mark of Fermi-liquid behavior. A review of drag effects in two-layer systems is given in Ref. [39]. A departure from the standard $\rho_{\rm D} \propto T^2$ temperature dependence indicates the occurrence of non-Fermi-liquid behavior. The low-temperature dependence of $\rho_{\rm D}$ for semiconductor electron-hole bilayers was studied experimentally in numerous recent works [40, 41]. On the theoretical side, we note the calculation by Hu [42], which predicted an enhancement of Coulomb drag for ordinary electron-hole bilayers at temperatures just above the excitonic instability, and the analysis of Ref. [43], which predicted a sharp increase of the drag resistivity as the temperature is lowered below the critical temperature of condensation.

In this chapter we show that the drag resistivity shows a precursor of the topological exciton condensed phase, *via* an upturn upon approaching the critical temperature, as shown in Fig. 3.1. Close to the critical temperature we find that on the basis of a Boltzmann analysis $\rho_{\rm D} \propto \log(T - T_{\rm c})$. This upturn could therefore be used to determine the proximity to the phase transition. We note that the

system considered here resembles double-layer graphene (DLG) – a system of two graphene layers separated by a dielectric barrier. The main differences are the number of degenerate electron species and the dielectric constant [14, 20]. The results presented here are therefore also qualitatively applicable to DLG, a system for which exciton condensation has been predicted too [14, 16, 15]. Coulomb drag in DLG has been intensively studied theoretically [44]. This literature, however, refers to drag in which both layers are either electron- or hole-doped so that exciton condensation does not occur.

3.2 Coulomb drag and exciton condensation

We consider a TI thin film whose top layer is electron-doped and whose bottom layer is hole-doped. We apply the "closed-band approximation" [14, 16, 15], *i.e.*, we consider only the upper Dirac cone for the electron layer and the lower Dirac cone for the hole layer. This is justified since the temperatures we consider are sufficiently small and the screening lengths sufficiently large, so that the far-lying bands can in first instance be considered inert. Then, the dispersions are well approximated by $\epsilon_{\mathrm{t}}(\boldsymbol{k}) = v|\boldsymbol{k}| - \mu_{\mathrm{t}}$ and $\epsilon_{\mathrm{b}}(\boldsymbol{k}) = -v|\boldsymbol{k}| + \mu_{\mathrm{b}}$ for the top and bottom layer, respectively ($\hbar = 1$ throughout this chapter). Here $v \approx 5 \times 10^5$ m/s is the Fermi velocity appropriate for the surface states of a typical TI thin film [11]. Note that the chemical potential for the electrons in the bottom layer is equal to $-\mu_{\mathrm{b}}$. These formulas are valid up to a cutoff $\xi = 0.2$ eV, which is the typical distance between the Dirac point and the bulk bands in a TI. We also introduce the mean Fermi energy, $\mu = (\mu_{\mathrm{t}} + \mu_{\mathrm{b}})/2$, and half the chemical potential imbalance, $h = (\mu_{\mathrm{t}} - \mu_{\mathrm{b}})/2$.

Our theoretical treatment is based on the Boltzmann equation, whose main merit is to give a physically transparent picture of the scattering processes that control the momentum transfer rate between the layers. The crucial quantity in the Boltzmann approach is the scattering amplitude $V_{\mathrm{eff}}(\boldsymbol{k}_1, \boldsymbol{k}_2, \boldsymbol{k}_3, \boldsymbol{k}_4)$, which is diagrammatically presented on the left-hand side in Fig. 3.2, where $\boldsymbol{k}_1$ and $\boldsymbol{k}_2$ are incoming electron momenta, one from each layer, and $\boldsymbol{k}_3$ and $\boldsymbol{k}_4$ outgoing electron momenta. Under ordinary circumstances this interaction is well approximated by the single *screened* interaction line $V_0(|\boldsymbol{k}_1 - \boldsymbol{k}_4|, \epsilon_{\mathrm{t}}(\boldsymbol{k}_1) - \epsilon_{\mathrm{t}}(\boldsymbol{k}_4))$, which is shown as a wavy line in Fig. 3.2 (see Sec. 3.6.1). But this simple picture breaks down in the vicinity of the exciton pairing transition, where it becomes necessary to include the effect of pairing fluctuations, diagrammatically represented by the infinite series of ladder diagrams shown in the right-hand side of Fig. 3.2. This series of diagrams diverges at the critical temperature T_{c} when the center-of-mass momentum of the electron-hole pair $\boldsymbol{K} = \boldsymbol{k}_1 - \boldsymbol{k}_3$ and the corresponding energy $\Omega = \epsilon_{\mathrm{t}}(\boldsymbol{k}_1) - \epsilon_{\mathrm{b}}(\boldsymbol{k}_3)$ tend to zero. Since the screened interlayer interaction V_0 is finite in the limit in

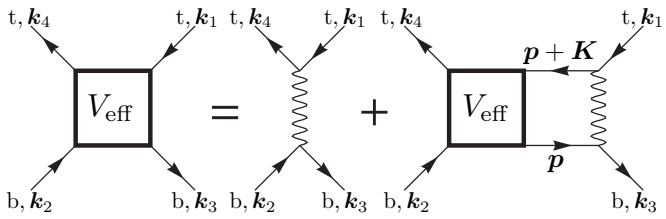

Figure 3.2: The Bethe-Salpeter equation for the effective interaction $V_{\rm eff}$ in Eq. (3.1). The thin wavy line is V_0 and the arrows are the electron propagators in the top layer (top arrows) and the bottom layer (bottom arrows). Furthermore, $\boldsymbol{K} = \boldsymbol{k}_1 - \boldsymbol{k}_3 = \boldsymbol{k}_4 - \boldsymbol{k}_2$ is the center-of-mass momentum of the electron-hole pair and $\boldsymbol{q} = \boldsymbol{k}_1 - \boldsymbol{k}_4 = \boldsymbol{k}_3 - \boldsymbol{k}_2$ is the interlayer momentum transfer, which is responsible for Coulomb drag. Finally, $\boldsymbol{p}$ is an integration variable. To make contact with the drag resistivity in Eq. (3.3) replace $\boldsymbol{k} = \boldsymbol{k}_1$ and $\boldsymbol{k}' = \boldsymbol{k}_2$.

which the momentum transfer $q = |\boldsymbol{k}_1 - \boldsymbol{k}_4|$ vanishes (*i.e.* it is not a long-range interaction), the qualitative behavior of the drag conductivity does not change when we neglect the momentum dependence of V_0. In this case the ladder sum in Fig. 3.2 can be performed exactly. In this manner one obtains an effective interaction that depends only on the center-of-mass momentum $\boldsymbol{K}$ and energy Ω as

$$V(\boldsymbol{k}_1, \boldsymbol{k}_2, \boldsymbol{k}_3, \boldsymbol{k}_4) \simeq V_{\rm eff}(\boldsymbol{K}, \Omega) \equiv \frac{U}{1 - U\Xi(\boldsymbol{K}, \Omega)} \ , \tag{3.1}$$

where U is an effective momentum-independent contact interaction strength representing the screened interaction and

$$\Xi(\boldsymbol{K}, \Omega) = \frac{1}{A} \sum_{\boldsymbol{k}} \frac{n(\epsilon_{\rm t}(\boldsymbol{k} + \boldsymbol{K})) - n(\epsilon_{\rm b}(\boldsymbol{k}))}{\epsilon_{\rm b}(\boldsymbol{k}) - \epsilon_{\rm t}(\boldsymbol{k} + \boldsymbol{K}) - \Omega - i0^+} \tag{3.2}$$

is the pairing susceptibility, A being the 2D electron system area. The temperature T enters the above expression through the Fermi-Dirac distribution, $n(E) = 1/[1 + \exp(\beta E)]$, where $\beta = (k_{\rm B}T)^{-1}$. It is easy to check that, in the symmetric case ($h = 0$) $\Xi(\boldsymbol{0}, 0)$ diverges logarithmically at zero temperature, and therefore the denominator of Eq. (3.1) must vanish at some non-zero temperature $T_{\rm c}$ no matter how small the electron-hole attraction. This is the mean-field pairing transition temperature. We see that, as the temperature is decreased towards $T_{\rm c}$, pairing fluctuations first lead to an enhancement of $V_{\rm eff}$ for small $\boldsymbol{K}$ and Ω and ultimately to a pole at $\Omega = 0$ and $\boldsymbol{K} = \boldsymbol{0}$ as $T = T_{\rm c}$. The occurrence of this pole is the cause for the upturn of the Coulomb drag resistivity close to $T_{\rm c}$.

By approximating V_0 by a contact interaction, we have introduced an unknown quantity in our theory, the contact interaction strength U, on which $T_{\rm c}$ depends. We stress that we do not calculate $T_{\rm c}$ by determining an estimate of U. Instead,

we leave U as a parameter in our theory, the dependence on which we scale out in Fig. 3.1. We determine the actual value of T_c using an alternative calculation, which does take into account the dependence of V_0 on momentum (see Sec. 3.6.2).

Inserting Eq. (3.1) in the Boltzmann collision integral and performing standard manipulations, we finally arrive at the following expression for the drag resistivity:

$$\begin{aligned}\rho_D = & -\frac{\beta}{2(2\pi)^6 e^2 n v^2}\int d\boldsymbol{K} d\Omega \frac{|V_{\rm eff}(\boldsymbol{K},\Omega)|^2}{\sinh^2(\beta\Omega/2)} \\ & \times \int d\boldsymbol{k} d\boldsymbol{k}' \Im m\left[b(\boldsymbol{k};\boldsymbol{K},\Omega)\right] \Im m\left[b(\boldsymbol{k}';\boldsymbol{K},\Omega)\right] \\ & \times \left[\boldsymbol{v}_t(\boldsymbol{k}'+\boldsymbol{K}) - \boldsymbol{v}_t(\boldsymbol{k}+\boldsymbol{K})\right]\cdot\left[\boldsymbol{v}_b(\boldsymbol{k}') - \boldsymbol{v}_b(\boldsymbol{k})\right] , \end{aligned} \tag{3.3}$$

where $\boldsymbol{v}_{t(b)}(\boldsymbol{k}) \equiv \boldsymbol{\nabla}\epsilon_{t(b)}(\boldsymbol{k})$ are the group velocities, n is the single layer carrier density, and

$$b(\boldsymbol{k};\boldsymbol{K},\Omega) \equiv \frac{n(\epsilon_t(\boldsymbol{k}+\boldsymbol{K})) - n(\epsilon_b(\boldsymbol{k}))}{\epsilon_b(\boldsymbol{k}) - \epsilon_t(\boldsymbol{k}+\boldsymbol{K}) - \Omega - i0^+} \tag{3.4}$$

is the summand of Eq. (3.2) [45]. Since $\boldsymbol{v}_t(\boldsymbol{k})$ and $\boldsymbol{v}_b(\boldsymbol{k})$ are oppositely directed ρ_D is positive, as expected for carriers of opposite polarities.

3.3 Drag Resistivity

To determine the drag resistivity we need to evaluate Eq. (3.3) numerically. However, the qualitative behavior near T_c can be obtained analytically as follows (in what follows we first consider the balanced case $h = 0$). First, we notice that the denominator of Eq. (3.1) can be expanded, for small K and Ω as follows:

$$1 - U\Xi(\boldsymbol{K},\Omega) \simeq \alpha(T) + a(T)U\nu_0(\beta v K)^2 + iU\nu_0\beta\Omega/4 , \tag{3.5}$$

where $\alpha(T) \propto T - T_c$ measures the distance from the critical point, $\nu_0 = \mu/(2\pi v^2)$ is the density-of-states at the Fermi energy, and $a(T)$ is a (dimensionless) positive ultraviolet-convergent quantity. Further, for $\boldsymbol{K} \to \boldsymbol{0}$ we have $[\boldsymbol{v}_t(\boldsymbol{k}'+\boldsymbol{K}) - \boldsymbol{v}_t(\boldsymbol{k}+\boldsymbol{K})]\cdot[\boldsymbol{v}_b(\boldsymbol{k}') - \boldsymbol{v}_b(\boldsymbol{k})] = 2v^2[\cos(\phi) - 1]$, where ϕ is the angle between $\boldsymbol{k}$ and $\boldsymbol{k}'$. Since this quantity vanishes only in a set of zero measure with respect to the two 2D integrals over $\boldsymbol{k}$ and $\boldsymbol{k}'$ in Eq. (3.3), we can approximate the scalar product with a momentum-independent quantity of the order of v^2. The integrals over $\boldsymbol{k}$ and $\boldsymbol{k}'$ can now be carried out analytically. Using that $\int d\boldsymbol{k}\ \Im m[b(\boldsymbol{k};\boldsymbol{0},\Omega)] = \Im m[\Xi(\boldsymbol{0},\Omega)] = -\nu_0\beta\Omega/4$ for $\beta\Omega \ll 1$, we obtain

$$\rho_D \propto \int dK d\Omega \frac{(\beta\Omega/4)^2}{\sinh^2(\beta\Omega/2)} \frac{(\nu_0 U)^2 K}{\left[\alpha(T) + aU\nu_0(\beta v K)^2\right]^2 + (U\nu_0\beta\Omega/4)^2} , \tag{3.6}$$

which is immediately seen to diverge logarithmically when $T \to T_c$, *i.e.*, for $\alpha \to 0$. This behavior is not altered by the momentum dependence of V_0, since V_0 remains finite in the limit $q \to 0$ due to screening by carrier density fluctuations.

In Fig. 3.1 we show the numerically evaluated drag resistivity ρ_{D} as a function of temperature. We observe that for temperatures much larger than T_{c}, the drag resistivity increases quadratically as $\rho_{\mathrm{D}} \propto T^2$ [46]. The logarithmic divergence of $\rho_{\mathrm{D}} \propto \log(T - T_{\mathrm{c}})$ is clearly visible. From top to bottom the curves correspond to $T_{\mathrm{c}}/T_{\mathrm{F}} = (1/150, 1/200, 1/250)$. Following Ref. [41], we define T_{u} as the temperature at which the upturn of ρ_{D} starts, as shown in Fig. 3.1. As a rule of thumb, $T_{\mathrm{u}} \approx (3/2)T_{\mathrm{c}}$.

3.4 Critical temperature

In order to assess whether the upturn in the drag resistivity can be observed experimentally, we now need to actually calculate the (mean-field [47]) critical temperature as a function of interlayer distance and carrier density, taking into account screening effects [22, 23]. To do so, we employ a separable approximation to the momentum-dependent interlayer interaction $V_0(|\boldsymbol{k}_1 - \boldsymbol{k}_4|, \epsilon_{\mathrm{t}}(\boldsymbol{k}_1) - \epsilon_{\mathrm{t}}(\boldsymbol{k}_4))$ – see Ref. [48] and Sec. 3.6.2. The advantage of this approach over using a contact interaction is that it captures the decrease of the interaction strength V_0 with increasing transferred momenta. In particular, no ultraviolet cutoff on which the result for T_{c} would depend is needed.

As briefly explained in Sec. 3.6.1 and in much more detail in Ref. [49], the screened interlayer Coulomb interaction is given by $V_0(q, \omega) = V_{\mathrm{tb}}(q)/\varepsilon(q, \omega)$, where $V_{\mathrm{tb}}(q)$ is the bare interaction between one electron on the top surface and one on the bottom surface, $q = |\boldsymbol{k} - \boldsymbol{k}'|$ and $\omega = \epsilon_{\mathrm{b}}(\boldsymbol{k}) - \epsilon_{\mathrm{b}}(\boldsymbol{k}')$ are momentum and energy transfers, respectively, and $\varepsilon(q, \omega)$ is the dielectric screening function of the carriers, which we approximate in the random phase approximation. Both $V_{\mathrm{tb}}(q)$ and $\varepsilon(q, \omega)$ depend on the dielectric constants of the TI and of the environment surrounding the thin film.

We consider a TI film with vacuum above the top surface and a typical substrate material (*e.g.* SiO_2) below the bottom surface: the appropriate background dielectric constants are $\epsilon_{\mathrm{top}} = 1,\ \epsilon_{\mathrm{TI}} = 100,\ \epsilon_{\mathrm{bottom}} = 4$. For the balanced case with $h = 0$ we obtain the phase diagram in Fig. 3.3. From right to left the lines correspond to carrier densities $n = (0.25, 0.5, 1) \times 10^{10}\ \mathrm{cm}^{-2}$. Our results show that the critical temperatures are within reach using existing cryogenic techniques for solid-state systems. Furthermore, also the required surface carrier densities have been reached previously [37]. In the inset of Fig. 3.3 we show the effect of a non-zero density imbalance. The solid curves represent the behavior of T_{c}/μ for constant $k_{\mathrm{F}}d$. From top to bottom the curves correspond to $k_{\mathrm{F}}d = (0.05, 0.075, 0.1)$. We note that T_{c}/μ decreases strongly with increasing density imbalance. The dashed line is the line along which the quartic term of the Ginzburg-Landau expansion of the free energy in powers of the order parameter, evaluated at T_{c}, vanishes (see

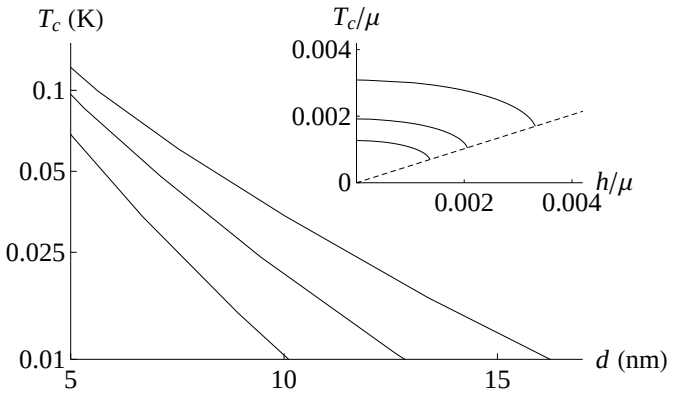

Figure 3.3: Critical temperature T_c (in K) versus interlayer distance d (in nm) in the absence of density imbalance ($h = 0$). From right to left the lines correspond to carrier densities $n = (0.25, 0.5, 1) \times 10^{10}$ cm^{-2}. Inset: The critical lines T_c/μ versus h/μ. From top to bottom the lines correspond to $k_F d = (0.05, 0.075, 0.1)$. The critical lines terminate on the dashed line, *i.e.*, the locus of the points where the fourth order term of the Ginzburg-Landau expansion of the free energy in powers of the order parameter vanishes.

Sec. 3.6.3). Thus, for a fixed $k_F d$, the transition becomes first order as h grows beyond the intersection of the dashed line and the curve corresponding to that $k_F d$ value. The first-order region below the dashed line cannot be accurately described by our present normal-state formalism. The decreasing behavior of T_c with h indicates that the excitonic transition is strongly suppressed by the presence of any density imbalance. Thus, it is important in experimental realizations to have accurate control over the electron and hole densities in the two layers.

3.5 Discussion and conclusions

Our theory predicts a divergence of ρ_D as T approaches T_c, but does not include the possible suppression of this divergence by critical fluctuations in the immediate vicinity of T_c. We expect that inclusion of these fluctuations leads to a down turn of ρ_D for temperatures very close to the critical temperature [50], before increasing again upon further decrease of the temperature, as predicted in Ref. [43].

We note that if the layers are brought too close together, the wave functions in the top layer and the bottom layer begin to overlap and interlayer tunneling becomes important. This limits our theory to a minimal interlayer distance $d \gtrsim 10$ nm. Actually, also conduction over the side layers of the TI film could be important. One expects that for samples of large enough area, these can be neglected. If not, a transport-prohibiting gap could be induced in the side layers

by interfacing those with a ferromagnet.

In closing, we note that the upturn of $\rho_{\rm D}$ is analogous to the upturn of the spin-drag resistivity recently predicted in a cold gas of fermionic atoms near a ferromagnetic transition [51]. In particular, spin-fluctuation contributions to the effective interaction in the ferromagnetic case play the same role as pairing fluctuations in the present case. The reason why in Ref. [51] the spin drag resistivity was predicted to remain finite at $T_{\rm c}$ is that the transverse spin-fluctuation channel was treated as part of the familiar (Hartree) charge and longitudinal spin-density fluctuation channels. When transverse spin fluctuations in the Fock channel are also included, a logarithmic divergence is obtained, just as in the present case. We also note that our results, while qualitatively similar to those obtained in Ref. [42] for massive electrons and holes in a conventional electron-hole semiconductor bilayer, differ, at the theoretical level, by the inclusion of an additional term in the collision integral. This term is easily missed by using the Kubo formula. The nature of the additional term is similar to the vertex corrections that are responsible for replacing the momentum lifetime by the transport lifetime in the classical Drude formula for the resistivity.

3.6 Appendix

3.6.1 Details on the screened interactions

In the random phase approximation (RPA) the screened inter-layer Coulomb interaction depicted as a wavy line in Fig. 3.2 is given by

$$V_0(q,\omega) = \frac{V_{\rm tb}(q)}{\varepsilon(q,\omega)} \ , \tag{3.7}$$

where $q = |\boldsymbol{k}_1 - \boldsymbol{k}_4|$ and $\omega = \epsilon_{\rm t}(\boldsymbol{k}_1) - \epsilon_{\rm t}(\boldsymbol{k}_4)$ are momentum and energy transfers, respectively. Here,

$$\varepsilon(q,\omega) = [1 - V_{\rm tt}(q)\chi_{\rm t}(q,\omega)][1 - V_{\rm bb}(q)\chi_{\rm b}(q,\omega)] - V_{\rm tb}^2(q)\chi_{\rm t}(q,\omega)\chi_{\rm b}(q,\omega) \tag{3.8}$$

is the RPA dielectric screening function [49], where $\chi_{\rm t(b)}(q,\omega)$ are the well-known Lindhard functions of a (spinless-valleyless) noninteracting massless Dirac fermion gas [52]. The other ingredients in the expression for $\varepsilon(q,\omega)$ are [49]:

- The bare interaction between one electron on the top surface and one in the bottom surface:
$$V_{\rm tb}(q) = \frac{8\pi e^2 \epsilon_{\rm TI}}{qD(q)} \ . \tag{3.9}$$
- The bare interaction between two electrons on the top surface:
$$V_{\rm tt}(q) = \frac{4\pi e^2[(\epsilon_{\rm TI} + \epsilon_{\rm bottom})\exp(qd) + (\epsilon_{\rm TI} - \epsilon_{\rm bottom})\exp(-qd)]}{qD(q)} \ , \tag{3.10}$$

d being the distance between the two surfaces of the TI film.

In the previous equations,

$$D(q) = (\epsilon_{\rm top} + \epsilon_{\rm TI})(\epsilon_{\rm TI} + \epsilon_{\rm bottom}) \exp(qd) + (\epsilon_{\rm top} - \epsilon_{\rm TI})(\epsilon_{\rm TI} - \epsilon_{\rm bottom}) \exp(-qd) \ , \tag{3.11}$$

$\epsilon_{\rm top}$ ($\epsilon_{\rm bottom}$) is the dielectric constant of the material above (below) the top (bottom) surface of the TI thin film, and $\epsilon_{\rm TI} \sim 100 \gg \epsilon_{\rm top}, \epsilon_{\rm bottom}$ is the dielectric constant of the TI film. The bare interaction between two electrons on the bottom surface, $V_{\rm bb}(q)$, can be obtained from $V_{\rm tt}(q)$ by interchanging $\epsilon_{\rm top} \leftrightarrow \epsilon_{\rm bottom}$.

3.6.2 Derivation of the equation for the critical temperature

In this Section we show how to obtain the equation for the critical temperature, which is briefly summarized in the footnote Ref. [48]. We start from the linearized gap equation, which reads [16]

$$\Delta(\boldsymbol{k}) = \frac{1}{(2\pi)^2} \int d^2\boldsymbol{k}' \ V_0(|\boldsymbol{k} - \boldsymbol{k}'|, \epsilon_{\rm t}(\boldsymbol{k}) - \epsilon_{\rm t}(\boldsymbol{k}')) \\ \times \frac{1 + \cos(\phi_{\boldsymbol{k}} - \phi_{\boldsymbol{k}'})}{2} \frac{n(\epsilon_{\rm b}(\boldsymbol{k}')) - n(\epsilon_{\rm t}(\boldsymbol{k}'))}{\epsilon_{\rm b}(\boldsymbol{k}') - \epsilon_{\rm t}(\boldsymbol{k}')} \ \Delta(\boldsymbol{k}') \ , \tag{3.12}$$

where, as we have seen in Sect 3.6.1, $V_0 = V_0(q, \omega)$ is the screened interlayer interaction incorporating screening effects by carrier density fluctuations and by the dielectric media. We note that for

$$V_0(|\boldsymbol{k} - \boldsymbol{k}'|, \epsilon_{\rm t}(\boldsymbol{k}) - \epsilon_{\rm t}(\boldsymbol{k}')) \ \frac{1 + \cos(\phi_{\boldsymbol{k}} - \phi_{\boldsymbol{k}'})}{2} \to U \ , \tag{3.13}$$

the gap equation has a solution when $1 - U\Xi(\boldsymbol{0}, 0) = 0$.

We consider solutions in which $\Delta(\boldsymbol{k})$ depends only on $k = |\boldsymbol{k}|$:

$$\Delta(k) = \frac{1}{2\pi} \int_0^\infty dk' \ k' V^{\rm av}(k, k') \frac{n(\epsilon_{\rm b}(k')) - n(\epsilon_{\rm t}(k'))}{\epsilon_{\rm b}(k') - \epsilon_{\rm t}(k')} \Delta(k') \ , \tag{3.14}$$

where the angle-averaged interaction $V^{\rm av}(k, k')$ is defined by

$$V^{\rm av}(k, k') \equiv \frac{1}{2\pi} \int_0^{2\pi} d\phi \frac{1 + \cos(\phi)}{2} V_0(|\boldsymbol{k} - \boldsymbol{k}'|, \varepsilon_{\rm t}(\boldsymbol{k}) - \varepsilon_{\rm t}(\boldsymbol{k}')) \ , \tag{3.15}$$

ϕ being the angle between $\boldsymbol{k}$ and $\boldsymbol{k}'$. To solve the gap equation (3.14) we employ the so-called "separable approximation" for $V^{\rm av}(k, k')$:

$$V^{\rm av}(k, k') = V^{\rm sep}(k) V^{\rm sep}(k') \ . \tag{3.16}$$

This is useful since under this approximation it follows that $\Delta(k) = \tilde{\Delta}\ V^{\rm sep}(k)$, where $\tilde{\Delta}$ is a constant, and we immediately obtain the $T_{\rm c}$-equation reported in the footnote Ref. [48], *i.e.*

$$1 = \frac{1}{2\pi}\int k'dk'[V^{\rm sep}(k')]^2\frac{n(\epsilon_{\rm b}(k')) - n(\epsilon_{\rm t}(k'))}{\epsilon_{\rm b}(k') - \epsilon_{\rm t}(k')}\ . \tag{3.17}$$

A natural choice for the separable interaction $V^{\rm sep}(k)$ is

$$V^{\rm sep}(k) = \frac{V^{\rm av}(k,k_{\rm F})}{\sqrt{V^{\rm av}(k_{\rm F},k_{\rm F})}}\ , \tag{3.18}$$

and we use this form of $V^{\rm sep}(k)$ to obtain Fig. 3.3. Notice that the choice (3.18) is an accurate representation of the microscopic angle-averaged interaction (3.15) when $k, k' \to k_{\rm F}$.

3.6.3 Ginzburg-Landau Expansion

In this Section we show how to find the Ginzburg-Landau expansion of the free energy used to obtain the dashed line in Fig. 3.3. The sign of the prefactor of the fourth-order term of this expansion in powers of the order parameter determines the stability of our theory, which uses an expansion in a small order parameter. If the sign is negative, the small order parameter expansion is not sufficient to obtain the phase diagram and in that region a more involved calculation is required. This region is indicated in Fig. 3.3 by the area below the dashed line.

The noninteracting action is

$$\begin{aligned} S_0[\psi^*,\psi] &= \sum_{\boldsymbol{k},\omega_n,\sigma}\psi^*_\sigma(\boldsymbol{k},i\omega_n)[-i\hbar\omega_n + \epsilon_\sigma(\boldsymbol{k})]\psi_\sigma(\boldsymbol{k},i\omega_n) \\ &\equiv \sum_{\sigma,\sigma',\boldsymbol{k},\omega_n}\psi^*_\sigma(\boldsymbol{k},i\omega_n)[-\hbar G^{-1}_{0,\sigma,\sigma'}(\boldsymbol{k},\omega_n)]\psi_{\sigma'}(\boldsymbol{k},i\omega_n)\ , \end{aligned} \tag{3.19}$$

where ψ^*_σ and ψ_σ are Grassmann-valued fields describing the electrons in the hole-doped bottom layer (σ = b) and the electrons in the electron-doped top layer (σ = t). The fermionic Matsubara frequencies are ω_n and the non-interacting inverse Green's function is G_0^{-1}. The contribution to the action from the interlayer interaction in the contact approximation is

$$\begin{aligned} &S_{\rm int}[\psi^*,\psi] = \\ &-\frac{U}{\hbar\beta A}\sum_{\substack{\boldsymbol{k},\boldsymbol{k}',\boldsymbol{q}\\ \omega_n,\omega_{n'},\omega_q}}\psi^*_{\rm b}(\boldsymbol{k}-\boldsymbol{q},i\omega_n - i\omega_q)\psi_{\rm t}(\boldsymbol{k}',i\omega_{n'})\psi^*_{\rm t}(\boldsymbol{k}'+\boldsymbol{q},i\omega_{n'}+i\omega_q)\psi_{\rm b}(\boldsymbol{k},i\omega_n)\ , \end{aligned} \tag{3.20}$$

where $\boldsymbol{q}$ is the momentum transferred in the interaction and $\omega_n, \omega_{n'}$ are fermionic Matsubara frequencies while ω_q is a bosonic Matsubara frequency. Since the pairing is between particles with the same momentum and frequency, we need only retain the terms with $\boldsymbol{k}' = \boldsymbol{k} - \boldsymbol{q}$, $\omega_{n'} = \omega_n - \omega_q$

$$S_{\mathrm{int}}[\psi^*, \psi] = -\frac{U}{\hbar\beta A}\left[\sum_{\boldsymbol{k},\omega_n} \psi^*_{\mathrm{b}}(\boldsymbol{k}, i\omega_n)\psi_{\mathrm{t}}(\boldsymbol{k}, i\omega_n)\right] \times \left[\sum_{\boldsymbol{k},\omega_n} \psi^*_{\mathrm{t}}(\boldsymbol{k}, i\omega_n)\psi_{\mathrm{b}}(\boldsymbol{k}, i\omega_n)\right] . \tag{3.21}$$

We multiply with unity to introduce the order parameter Δ by means of

$$1 = \int d\Delta^* d\Delta \exp\left[-\frac{1}{\hbar}\left(\Delta^* - \frac{U}{\hbar\beta A}\sum_{\boldsymbol{k},\omega_n} \psi^*_{\mathrm{b}}(\boldsymbol{k}, i\omega_n)\psi_{\mathrm{t}}(\boldsymbol{k}, i\omega_n)\right) \times \frac{\hbar\beta A}{U} \times \left(\Delta - \frac{U}{\hbar\beta A}\sum_{\boldsymbol{k},\omega_n} \psi^*_{\mathrm{t}}(\boldsymbol{k}, i\omega_n)\psi_{\mathrm{b}}(\boldsymbol{k}, i\omega_n)\right)\right] . \tag{3.22}$$

In this manner we cancel the electronic interaction and obtain the effective action

$$S[\psi^*, \psi, \Delta^*, \Delta] = S_0[\psi^*, \psi] + \frac{\hbar\beta A|\Delta|^2}{U} - \left[\Delta \sum_{\boldsymbol{k},\omega_n} \psi^*_{\mathrm{b}}(\boldsymbol{k}, i\omega_n)\psi_{\mathrm{t}}(\boldsymbol{k}, i\omega_n) + \mathrm{C.C.}\right] . \tag{3.23}$$

From this expression we can immediately read off the inverse electron Green's function:

$$-\hbar G^{-1}_{\sigma,\sigma'}(\boldsymbol{k}, i\omega_n) = -\hbar G^{-1}_{0,\sigma,\sigma'}(\boldsymbol{k}, i\omega_n) + \hbar\sigma_{\sigma,\sigma'} , \tag{3.24}$$

where the off-diagonal self-energy is $\hbar\sigma_{\mathrm{t,b}} = -\Delta^*$ and $\hbar\sigma_{\mathrm{b,t}} = -\Delta$. Integrating out the electrons yields an effective action in terms of the order parameter only:

$$S[\Delta^*, \Delta] = \frac{\hbar\beta A|\Delta|^2}{U} - \hbar\mathrm{tr}\log(-G^{-1}) , \tag{3.25}$$

and expanding up to fourth order in Δ yields

$$\begin{aligned} -\hbar\mathrm{tr}\log(-G^{-1}) &= -\hbar\mathrm{tr}\log(-(G_0^{-1} - \sigma)) = -\hbar\mathrm{tr}\log(-G_0^{-1}) - \hbar\mathrm{tr}\log(1 - G_0\sigma) \\ &\approx -\hbar\mathrm{tr}\log(-G_0^{-1}) + \frac{\hbar}{2}\mathrm{tr}(G_0\sigma)^2 + \frac{\hbar}{4}\mathrm{tr}(G_0\sigma)^4 , \end{aligned} \tag{3.26}$$

where we used that G_0 is diagonal and σ is off-diagonal in the band indices. Performing the traces and evaluating the Matsubara summation leads to

$$S[\Delta^*, \Delta] = P_2|\Delta|^2 + P_4|\Delta|^4 , \tag{3.27}$$

with $P_2 = \hbar\beta A[1 - U\Xi(0,0)]/U$ and

$$P_4 = \frac{\hbar\beta}{2}\sum_{\boldsymbol{k}}\left\{\frac{n'(\epsilon_{\mathrm{b}}(\boldsymbol{k})) + n'(\epsilon_{\mathrm{t}}(\boldsymbol{k}))}{[\epsilon_{\mathrm{b}}(\boldsymbol{k}) - \epsilon_{\mathrm{t}}(\boldsymbol{k})]^2} - 2\frac{n(\epsilon_{\mathrm{b}}(\boldsymbol{k})) - n(\epsilon_{\mathrm{t}}(\boldsymbol{k}))}{[\epsilon_{\mathrm{b}}(\boldsymbol{k}) - \epsilon_{\mathrm{t}}(\boldsymbol{k})]^3}\right\} . \tag{3.28}$$

The dashed line in Fig. 3.3 has been obtained by evaluating numerically the region of parameter space where P_4 vanishes. We find that $P_4 > 0$ above the dashed line in Fig. 3.3 and thus our theory is appropriate in this region.

Chapter 4

Spin transport in a unitary Fermi gas close to the BCS transition

We consider spin transport in a two-component ultracold Fermi gas with attractive interspecies interactions close to the BCS pairing transition. In particular, we consider the spin-transport relaxation rate and the spin-diffusion constant. Upon approaching the transition, the scattering amplitude is enhanced by pairing fluctuations. However, as the system approaches the transition, the spectral weight for excitations close to the Fermi level is decreased by the formation of a pseudogap. To study the consequence of these two competing effects, we determine the spin-transport relaxation rate and the spin-diffusion constant using both a Boltzmann approach and a diagrammatic approach. The former ignores pseudogap physics and finite lifetime effects. In the latter, we incorporate the full pseudogap physics and lifetime effects, but we ignore vertex corrections, so that we effectively calculate single-particle relaxation rates instead of transport relaxation rates. We find that there is qualitative agreement between these two approaches although the results for the transport coefficients differ quantitatively.

4.1 Introduction

Over the last decade, there has been a growing interest in the physics community in the properties of spin transport, caused by the idea of using the electron spin as a carrier of information. A spin current is a net flow of spin and is fundamentally different from a charge current, because it relaxes in a different way. In particular, spin currents can be strongly affected by interactions.

Ultracold fermion systems consisting of two spin species provide a valuable model system for the study of the effects of interactions on spin transport, because

This chapter is based on: Spin transport in a unitary Fermi gas close to the BCS transition, M. P. Mink, V. P. J. Jacobs, H. T. C. Stoof, Marco Polini, G. Vignale, and R. A. Duine, to be submitted.

of the absence of disorder and their high tunability. When the cloud of one species moves relatively to the cloud of the other species, the latter is dragged along due to momentum relaxation by the interatomic interaction, and as a consequence, the spin current relaxes. This mechanism is called spin drag. A similar phenomenon, Coulomb drag, occurs in bilayer systems, in which the drift momentum difference between the carriers in the top and bottom layer relaxes due to the Coulomb interaction [2, 39].

In an important recent experimental study, the spin-diffusion constant, the spin susceptibility, and the relaxation rate of spin transport were investigated in an ultracold two-component fermion gas in the unitarity regime, where the interspecies interactions are as strong as quantum mechanics allows [7, 53]. Inspired by this work, the spin-transport relaxation rate and the spin-diffusion constant were calculated using a Boltzmann approach for high and low temperature ranges separately [54].

When an ultracold Fermi gas with two spin species and an attractive interaction between the spins is cooled to low enough temperatures it shows a transition to a superfluid state, where the opposite-spin atoms pair up to form Cooper pairs. The effect of interactions on spin transport close to this BCS pairing transition is an interesting subject, since two effects are competing. On the one hand, the scattering amplitude between fermions is enhanced by pairing fluctuations (preformed Cooper pairs) not taken into account in Ref. [54]. When the temperature is lowered, this effect ultimately leads to a diverging interaction strength and an instability in the system towards the BCS state at the critical temperature. As a consequence, transport coefficients like the spin-transport relaxation rate and the spin-diffusion constant, are expected to be strongly affected when the system approaches the transition. These effects were not seen experimentally in Ref. [7], possibly because T_c was not reached but possibly also due to the competing effect we discuss shortly.

In related work, for ultracold fermions with repulsive interactions, enhancement of the spin-transport relaxation rate was predicted close to the ferromagnetic transition [51], and for ultracold bosons close to Bose-Einstein condensation [55]. The latter was recently also observed experimentally [64]. Riedl *et al.* studied the frequencies and damping of collective modes in an ultracold Fermi gas close to the BCS pairing transition [56] and found an enhancement of the collision rate in a fermionic gas close to the BCS pairing transition. The behavior of the viscosity was studied in Ref. [57]. In electron-hole bilayers the electrons in one layer and holes in the other can form excitons, which are expected to condense for low enough temperatures. Theoretically, it was predicted that the transport relaxation rate is enhanced when approaching this transition [42]. An enhancement was measured experimentally [40, 41], although it is still under debate whether this enhancement was indeed caused by exciton condensation. Also for a topological insulator thin

film, an enhancement of the transport relaxation rate was predicted close to the (in this case topological) exciton condensation [58].

However, as already mentioned, there is a competing effect at play. For temperatures below the transition temperature, the system is in the superfluid state and the excitation spectrum is gapped. Already above T_c, a precursor of this gap can be seen as the suppression of spectral weight close to the Fermi level, a so-called pseudogap [59]. The suppressed spectral weight is closely linked to the reduced lifetime for these excitations. The effect of this pseudogap is to reduce the phase space for scattering events around the Fermi level, which is expected to reduce the enhancement of transport coefficients. It is the competition between the increase in scattering amplitude due to pairing fluctuations on the one hand, and the decrease in available phase space due to the pseudogap on the other, and its effect on the transport relaxation rate and the spin-diffusion constant that we consider in this chapter. This competition was considered in Ref. [60] for the spin susceptibility. We note related work determining the static spin susceptibility for repulsive interactions in Ref. [61].

In general, the relaxation rate of a current and the decay rate of a single-particle excitation are different because of the amount with which the possible scattering directions contribute to either case. In the case of the decay of a single-particle excitation, all directions are weighed equally, but in the case of current relaxation, forward scattering (in the direction of the current) contributes much less than back scattering (in the direction opposite to the current). Theoretically, in diagrammatic calculations, a transport relaxation rate is obtained by inclusion of so-called vertex corrections to the appropriate response function. If these are neglected, the transport relaxation time is essentially equal to the single-particle relaxation time.

In this chapter we consider a two-component gas of fermions consisting of two spin states labeled by $\sigma = \uparrow, \downarrow$. We consider the balanced case where the densities of each spin component are equal $n_\uparrow = n_\downarrow \equiv n$, and where both species have the dispersion $\xi(\mathbf{k}) = \hbar^2 k^2/2m - \mu$. This article consists of two parts. In the first part in Sec. 4.2 we use Boltzmann theory to calculate the relaxation rate for spin transport in this system for arbitrary interaction strength, both close to the BCS pairing transition and for temperatures much higher than the Fermi temperature. Then, using the non-interacting spin susceptibility, we can determine the spin-diffusion constant using the Einstein relation. This calculation incorporates the effect of pairing fluctuations, but does not take into account the pseudogap physics or the effect of the finite lifetime of the quasiparticle eigenstates. At the diagrammatic level, however, this calculation includes vertex corrections.

In the second part in Sec. 4.3 we calculate the fermion self-energy at unitarity both close to the BCS pairing transition and for high temperatures within the many-body T matrix approximation. This self-energy is the many-body T ma-

trix closed with a bare (non-interacting) fermion line. Using this self-energy, we determine the spectral function, and the spin-transport relaxation rate and spin susceptibility ignoring vertex corrections. Again, the spin-diffusion constant can be obtained using the Einstein relation. We end in Sec. 4.4 with our conclusions.

By comparing the spin-transport relaxation rate and diffusion constant obtained using both methods, we assess the importance of pseudogap physics, finite lifetime effects, and vertex corrections. We find that although the results of these two methods for the transport coefficients differ quantitatively, there is qualitative agreement. This indicates that pseudogap physics, finite lifetime effects, and vertex corrections do not have a critical influence on the prediction for the behavior of transport coefficients close to the BCS transition.

4.2 Boltzmann Theory

In this section we derive an expression for the spin-transport relaxation rate using the Boltzmann equation. We incorporate many-body effects, so-called pair correlations, close the BCS pairing transition. We apply a spin dependent driving force $\mathbf{F}_\uparrow = \mathbf{F}$ and $\mathbf{F}_\downarrow = -\mathbf{F}$ which will give rise to a spin current $\mathbf{j}_s$. The momentum increase by the driving force is balanced by the momentum relaxation due to the interaction between opposite spins, so that the system reaches a steady state. This mechanism is called spin drag. In linear response, the quantum kinetic equations are written as

$$\frac{1}{\hbar}\mathbf{F}\cdot\partial_{\mathbf{k}} n_F(\xi(\mathbf{k})) = \Gamma_\uparrow(\mathbf{k}) \tag{4.1}$$

$$-\frac{1}{\hbar}\mathbf{F}\cdot\partial_{\mathbf{k}} n_F(\xi(\mathbf{k})) = \Gamma_\downarrow(\mathbf{k}), \tag{4.2}$$

where $n_F(\epsilon) = 1/[1+\exp(\beta\epsilon)]$ is the Fermi-Dirac distribution with $\beta = 1/k_B T$ the inverse thermal energy and where the collision integral $\Gamma_\sigma(\mathbf{k})$ gives the net particle flux into the $(\mathbf{k}, |\sigma\rangle)$ state due to interspecies interactions. The Fermi's golden rule expression for $\Gamma_\uparrow(\mathbf{k})$ is

$$\Gamma_\uparrow(\mathbf{k}) = \frac{2\pi}{\hbar V^2}\sum_{\mathbf{k}_1,\mathbf{k}_2,\mathbf{k}_3,\mathbf{k}_4} \delta_{\mathbf{k}_1+\mathbf{k}_2,\mathbf{k}_3+\mathbf{k}_4}\delta(\xi_1+\xi_2-\xi_3-\xi_4) \times |T^{MB}|^2 f_{\uparrow,1} f_{\downarrow,2}(1-f_{\downarrow,3})(1-f_{\uparrow,4})(\delta_{\mathbf{k}_1,\mathbf{k}} - \delta_{\mathbf{k}_4,\mathbf{k}}), \tag{4.3}$$

where V is the volume and where we used a shorthand notation for the energy $\xi_i = \xi(\mathbf{k}_i)$ and for the non-equilibrium distributions $f_{\sigma,i} = f_\sigma(\mathbf{k}_i)$, and where we note that an analogous expression holds for $\Gamma_\downarrow(\mathbf{k})$. Eq. (4.3) considers the total effect of incoming particles with momenta and spin $\mathbf{k}_1,\uparrow$ and $\mathbf{k}_2,\downarrow$ that are scattered into momenta and spin $\mathbf{k}_3,\downarrow$ and $\mathbf{k}_4,\uparrow$. Momentum and energy

conservation is ensured by the Kronecker and Dirac δ's, respectively. The many-body T matrix T^{MB} gives the scattering amplitude incorporating the effects of the medium, and will be specified below.

The distribution functions are shifted from the equilibrium distribution by a momentum $\mathbf{k}_\sigma = m\mathbf{v}_\sigma/\hbar$, where $\mathbf{v}$ is the so-called drift velocity, which is related to the spin current by $\mathbf{j}_s = n_\uparrow \mathbf{v}_\uparrow - n_\downarrow \mathbf{v}_\downarrow = 2n\mathbf{v}$. Here, we used that due to symmetry, the drift velocities of the two species will be opposite and of equal magnitude for both species. The distribution function $f_\sigma(\mathbf{k})$ to first order in the drift velocity is $f_\sigma(\mathbf{k}) = n_F(\xi_\sigma(\mathbf{k})) + f^1_\sigma(\mathbf{k})$, where $f^1_\sigma(\mathbf{k}) = -\hbar(\mathbf{v}_\sigma \cdot \mathbf{k})n'_F(\xi_\sigma(\mathbf{k}))$. By subtracting Eq. (4.2) from Eq. (4.1), multiplying with $\hbar\mathbf{k}$, and summing over $\mathbf{k}$, we arrive at the momentum balance equation

$$-n\mathbf{F} = \frac{1}{V}\sum_{\mathbf{k}} (\hbar\mathbf{k})\Gamma(\mathbf{k}) = \tilde{\Gamma}\mathbf{v} + \mathcal{O}(v^2), \tag{4.4}$$

where the coefficient $\tilde{\Gamma}$ of the linear term in the right-hand side is given by

$$\begin{aligned}\tilde{\Gamma} = -\frac{\pi\beta\hbar}{6V^3}\sum_{\mathbf{k}_i} &\delta(\mathbf{k}_1 + \mathbf{k}_2 - \mathbf{k}_3 - \mathbf{k}_4)\delta(\xi_1 + \xi_2 - \xi_3 - \xi_4) \\ &\times |T^{MB}|^2 n_1 n_2 (1 - n_3)(1 - n_4)(\mathbf{k}_1 - \mathbf{k}_2 + \mathbf{k}_3 - \mathbf{k}_4)^2\end{aligned} \tag{4.5}$$

and we introduced the shorthand notation $n_i = n_F(\xi(\mathbf{k}_i))$. We introduce the drag conductivity as $\mathbf{j}_s = \sigma_D\mathbf{F}$ and from Eq. (4.4), we identify $\sigma_D = -2n^2/\tilde{\Gamma}$. The drag conductivity can be related to the spin-transport relaxation rate $1/\tau_D$ by the Drude formula $\sigma_D = 2n\tau_D/m$ leading to $1/\tau_D = -\tilde{\Gamma}/mn$.

To make further progress, we rewrite Eq. (4.5) in a form that is convenient to account for a divergence in the pairing channel due to pairing fluctuations close to the superfluid transition. First, we introduce an additional energy integral over the variable $\hbar\omega = \xi(\mathbf{k}_1) + \xi(\mathbf{k}_2)$, i.e., the sum of the energies of the two incoming particles in the scattering event. This choice is convenient because close to the superfluid transition, in the on-shell approximation, the only energy on which T^{MB} depends is $\hbar\omega$. We stress that this choice is different from the conventional one, where $\hbar\omega$ is the taken to be the difference between the energies of the incoming and outgoing $\uparrow$-particles [39]. Next, we solve the momentum conserving delta function by choosing $\mathbf{k}_1 = \mathbf{k} + \mathbf{K}/2$, $\mathbf{k}_2 = \mathbf{K}/2 - \mathbf{k}$, $\mathbf{k}_3 = \mathbf{k}' + \mathbf{K}/2$, and $\mathbf{k}_4 = \mathbf{K}/2 - \mathbf{k}'$. Then, after using the Dirac identity $\Im[1/(x + i0)] = -\pi\delta(x)$, we rewrite Eq. (4.5)

into

$$\frac{1}{\tau_D} = \frac{\pi\beta\hbar}{6\pi^2 mn}\int \frac{d\mathbf{k}}{(2\pi)^3}\frac{d\mathbf{k}'}{(2\pi)^3}\frac{d\mathbf{K}}{(2\pi)^3} d(\hbar\omega)(\mathbf{k}'+\mathbf{k})^2 \frac{|T^{MB}(\mathbf{K},\hbar\omega)|^2}{\sinh^2(\beta\hbar\omega/2)} \times \Im\left[\frac{1-n_F(\xi(\mathbf{k}+\mathbf{K}/2))-n_F(\xi(\mathbf{K}/2-\mathbf{k}))}{\hbar\omega+i0-(\xi(\mathbf{k}+\mathbf{K}/2)+\xi(\mathbf{K}/2-\mathbf{k}))}\right] \times \Im\left[\frac{1-n_F(\xi(\mathbf{k}'+\mathbf{K}/2))-n_F(\xi(\mathbf{K}/2-\mathbf{k}'))}{\hbar\omega+i0-(\xi(\mathbf{k}'+\mathbf{K}/2)+\xi(\mathbf{K}/2-\mathbf{k}'))}\right]. \tag{4.6}$$

The many-body matrix element $T^{MB}(\mathbf{K},\hbar\omega)$ close to the superfluid transition takes the simple form

$$T^{MB}(\mathbf{K},\hbar\omega) = \frac{V_0}{1-V_0\Xi(\mathbf{K},\hbar\omega)} \tag{4.7}$$

in these variables, where $V_0 = 4\pi a\hbar^2/m$ with a the s-wave scattering length. The bare pairing susceptibility Ξ is given by

$$\Xi(\mathbf{K},\hbar\omega) = \frac{1}{V}\sum_{\mathbf{k}}\left[\frac{1-n_F(\xi(\mathbf{k}+\mathbf{K}/2))-n_F(\xi(\mathbf{k}-\mathbf{K}/2))}{\hbar\omega+i0-(\xi(\mathbf{k}+\mathbf{K}/2)+\xi(\mathbf{k}-\mathbf{K}/2))}+\frac{1}{2\epsilon(\mathbf{k})}\right], \tag{4.8}$$

with $\epsilon(\mathbf{k}) = \hbar^2k^2/2m$. We note that the transition temperature T_c to the superfluid state is determined by $1/T^{MB}(\mathbf{0},0) = 0$. In Eq. (4.6), we can perform the integrals over $\mathbf{k}$, $\mathbf{k}'$, and the angles of $\mathbf{K}$ exactly. The integrals over ω and the length of $\mathbf{K}$ must then be performed numerically. Our theory does not take into account the superfluid gap or the presence of Cooper pairs for $T < T_c$, and is thus only valid for temperature higher than the transition temperature.

To obtain results for $1/\tau_D$ at constant density, we need to solve the non-interacting equation of state $n = (1/V)\sum_{\mathbf{k}} n_F(\xi(\mathbf{k}))$, which yields the function $\mu(T,n)$, shown as the dashed line in Fig. 4.6. For low temperatures, μ is given by the familiar relation $\mu = \epsilon_F[1-(\pi^2/12)(k_BT/\epsilon_F)^2]$. Here, the Fermi energy $\epsilon_F = k_BT_F = \hbar^2k_F^2/2m$ with the Fermi wavenumber $k_F = (6\pi^2 n)^{1/3}$. The transition temperature can then be determined as a function of the dimensionless interaction parameter k_Fa. We find at unitarity ($-1/k_Fa = 0$) $T_c = 0.50T_F$ and that for weak coupling where ($-1/k_Fa \gg 1$) $T_c \propto T_F\exp(-\pi/2k_F|a|)$.

In Fig. 4.1 we show the dimensionless spin-transport relaxation rate $\hbar/\epsilon_F\tau_D$ obtained from Eq. (4.6) as a function of the reduced temperature T/T_F. Each curve terminates at the value of the transition temperature corresponding to its k_Fa value. These curves illustrate a number of effects. Firstly, we see that, for all k_Fa, the relaxation rate is enhanced (but remains finite) when approaching T_c from above. This enhancement is larger in the strong-coupling case than in the weak-coupling case. The reason for this enhancement is that pairing fluctuations become important close to the superfluid transition, which lead to the appearance of a pole in T^{MB} in the integrand of Eq. (4.6) at $\mathbf{K} = \mathbf{0}$ and $\omega = 0$.

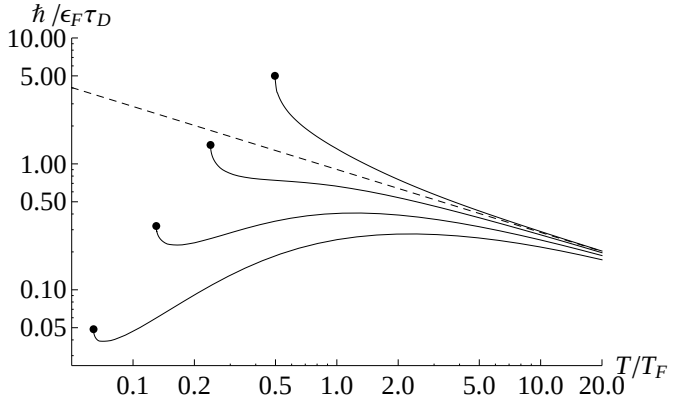

Figure 4.1: The dimensionless spin-transport relaxation rate $\hbar/\epsilon_F\tau_D$ obtained from Eq. (4.6) as a function of the reduced temperature T/T_F. From top to bottom the curves correspond to interaction parameters $-1/k_Fa = \{0, 0.56, 1.0, 1.4\}$. Each curve terminates at the value of the transition temperature corresponding to its k_Fa value: in decreasing order these are $T/T_F = \{0.50, 0.24, 0.13, 0.064\}$. The dashed line is the high-temperature asymptote $1/\tau_D \propto 1/\sqrt{T}$ predicted in Ref. [54].

For large temperatures, all curves approach the dashed line in Fig. 4.1 given by $1/\tau_D = (\epsilon_F/\hbar)(32\sqrt{2}/9\pi^{3/2})\sqrt{T_F/T}$ which falls off as $1/\sqrt{T}$, and was determined in [54]. This high-temperature behavior was also measured experimentally [7].

In the weak-coupling case ($-1/k_Fa \gtrsim 1$), we note an increase of $1/\tau_D$ with temperature up to $T \approx T_F$. An increase in temperature leads to a larger phase space available for scattering events due to reduced Pauli blocking. In the absence of many-body effects ($T^{MB} = V_0$), this effect would lead to the standard T^2 dependence of transport coefficients in a Fermi liquid. Indeed, when $T^{MB} = V_0$, we recover the weak-coupling result by Bruun, $1/\tau_D = (16\pi/9)(k_F^2a^2\epsilon_F/\hbar)(T/T_F)^2$ for $T \ll T_c$ [54].

We note that our theory overestimates the T_c at unitarity in comparison with the value $T_c = 0.15T_F$ obtained by Monte Carlo and RG methods (see e.g. Ref. [62]). In this sense, the experimental result for the spin-transport relaxation rate in Ref. [7] should not be compared to the top curve in Fig. 4.1 at unitarity, but instead to the second from below, which has a finite k_Fa value and $T_c = 0.13T_F$. Then, we see that our result agrees rather well with the experimental results Ref. [7].

To obtain the diffusion constant D_s we use the Einstein relation $D_s = \sigma_D/\chi_s$. For the spin susceptibility, we use the result from the non-interacting case $\chi_s = -(1/V)\sum_{\mathbf{k}} n'(\xi(\mathbf{k}))$. The result is shown in Fig. 4.2 where we plot the diffusion constant scaled by $m/\hbar$ versus the reduced temperature. The vertical order of the

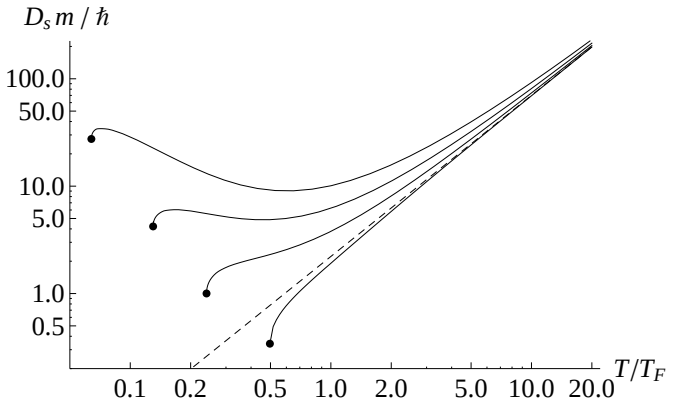

Figure 4.2: The dimensionless spin-diffusion constant $D_s m/\hbar$ obtained from the result of Fig. 4.1 using the Einstein relation. From bottom to top the curves correspond to interaction parameters $-1/k_F a = \{0, 0.56, 1.0, 1.4\}$. Each curve terminates at the value of the transition temperature corresponding to its $k_F a$ value. The dashed line is the high-temperature asymptote $D_s = (\hbar/m)(9\pi^{3/2}/16\sqrt{2})(T/T_F)^{3/2}$

curves is reversed with respect to Fig. 4.1. Each curve terminates again at the value of the transition temperature corresponding to its $k_F a$ value. The remarks made about Fig. 4.1 for a large part carry over to our results for the diffusion constant in Fig. 4.2. We see a suppression of D_s when approaching the transition for all $k_F a$ values. For the top two curves with $-1/k_F a = \{1.0, 1.4\}$ we see that the non-monotonous behavior of $1/\tau_D$ is also present in the curves for D_s, which for these $k_F a$ values now have a minimum around $T/T_F = 0.5$. Since χ_s follows the Curie law $\chi_s = n/k_B T$ for high temperatures , we find that for high temperatures $D_s = (\hbar/m)(9\pi^{3/2}/16\sqrt{2})(T/T_F)^{3/2}$, which is shown as the dashed line in Fig. 4.2. We note the factor 2 difference with the result for this asymptote from Ref. [54], which is caused by a different definition of σ_D. We note that if we again compare the second curve from above, which has a finite $k_F a$ value and $T_c = 0.13 T_F$, with the experimental results from Ref. [7] at unitarity, we see remarkably good qualitative agreement: both curves flatten off for temperatures below $T/T_F = 0.5$. Considering our results, we see that this behavior is actually the crossover behavior between the monotonous behavior of the unitary (bottom) curve in Fig. 4.2 and the non-monotonous behavior of the weak-coupling (top) curve. Clearly, a strength of our approach is that we can determine the whole temperature range using a single approach.

4.3 Diagrammatic Theory

In the second part of this work, we use a diagrammatic approach to determine the self-energy, spectral functions, and transport coefficients.

4.3.1 Definitions

First, we recall some aspects of the microscopic theory of an interacting gas of fermions. The central quantity in this theory is the self-energy, which is the sum of all one-particle reducible diagrams, and the spectral function derived from it. For reference we give the expressions for the spectral function, and the density of states and the particle density in an interacting system in terms of the spectral function. For a system which is translationally invariant in space and time, the retarded fermion Green's function is given by

$$G(\mathbf{k},\omega) = \frac{-\hbar}{-\hbar\omega^{+} + \xi(\mathbf{k}) + \hbar\Sigma(\mathbf{k},\omega)}, \tag{4.9}$$

where $\Sigma(\mathbf{k},\omega)$ is the retarded self-energy. The spectral function describes the weight of an excitation and is given by

$$\rho(\mathbf{k},\omega) = -\frac{1}{\pi\hbar}\Im\left[G(\mathbf{k},\omega)\right] = -\frac{1}{\pi\hbar}\frac{\Im\Sigma(\mathbf{k},\omega)}{\left[-\omega + \xi(\mathbf{k})/\hbar + \Re\Sigma(\mathbf{k},\omega)\right]^2 + \Im^2\Sigma(\mathbf{k},\omega)}. \tag{4.10}$$

In the absence of interactions, $\Sigma = 0$ and the spectral function is a δ-peak at $\hbar\omega = \xi(\mathbf{k})$. A nonzero real part of Σ will shift the δ-peak to the solution of $\omega = \xi(\mathbf{k})/\hbar + \Re\Sigma(\mathbf{k},\omega)$, while a nonzero $\Im\Sigma$ will lead to a broadening of the peak, indicating a finite life time of the single-particle excitation. In particular, a constant $\Im\Sigma = -1/2\tau$ will lead to a spectral function with a Lorentzian shape with width τ. We note several relations for the spectral function that we use later. The sum rule states that

$$\int d\hbar\omega\rho(\mathbf{k},\omega) = 1, \tag{4.11}$$

and follows from the commutation relation of the fermion fields. The density of states is

$$\nu(\omega) = \frac{1}{(2\pi)^3}\int d\mathbf{k}\rho(\mathbf{k},\omega), \tag{4.12}$$

and the equation of state is

$$n = \int d\hbar\omega n_F(\omega)\nu(\omega). \tag{4.13}$$

Using the Kubo formalism, we obtain the spin-transport relaxation rate $1/\tau_D$ and spin susceptibility $\chi_s = \partial(n_\uparrow - n_\downarrow)/\partial(\mu_\uparrow - \mu_\downarrow)$ in terms of the spectral function.

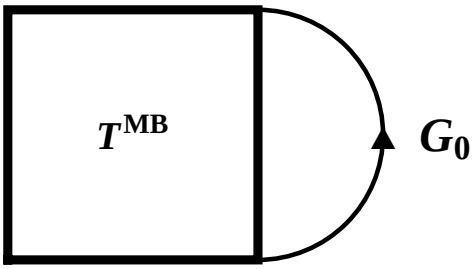

Figure 4.3: The self-energy Σ is the many-body T matrix closed with a single non-interacting Green's function line.

These are in the absence of vertex corrections given by

$$\frac{1}{\tau_D} = -\frac{3mn}{\pi\hbar^3}\left[\frac{1}{V}\sum_{\mathbf{k}}\mathbf{k}^2\int d\hbar\omega\rho^2(\mathbf{k},\omega)n'(\hbar\omega)\right]^{-1}, \tag{4.14}$$

and

$$\chi_s = -\frac{1}{V}\sum_{\mathbf{k}}\int d\hbar\omega d\hbar\omega'\rho(\mathbf{k},\omega)\rho(\mathbf{k},\omega')\frac{n_F(\hbar\omega)-n_F(\hbar\omega')}{\hbar\omega-\hbar\omega'}. \tag{4.15}$$

We note that for $\Sigma = -i/2\tau$, Eq. (4.14) gives $1/\tau_D = 1/\tau$, and that in the non-interacting case for low temperatures, Eq. (4.15) reduces to the well known $\chi_0 = 3n/2\epsilon_F$. Finally, we note that we can obtain the spin-diffusion constant D_s via the Einstein relation $D_s = \sigma_D/\chi_s$.

4.3.2 Self-energy

We calculate the fermion self-energy which is appropriate for this system both close to the BCS pairing transition and for high temperatures at unitarity [63]. Indeed the many-body T matrix closed with a non-interacting fermion line shown in Fig. 4.3, incorporates the effect enhancement of the interaction close to the BCS transition. In the dilute limit for weak interactions, where $T^{MB} \to V_0$, it reduces to the standard mean-field shift of the dispersion $V_0 n$. The expression for Σ as a function of momentum $\mathbf{k}$ and fermionic Matsubara frequency ω_n is

$$\Sigma(\mathbf{k}, i\hbar\omega_n) = \frac{1}{\hbar^2\beta}\frac{1}{V}\sum_{\mathbf{K},\omega_m} T^{MB}(\mathbf{K}, i\hbar\omega_m)G(\mathbf{K}-\mathbf{k}, i\hbar(\omega_m-\omega_n)), \tag{4.16}$$

where the summation is over the bosonic Matsubara frequencies ω_m. We compute the Matsubara summation of Eq. (4.16) to obtain

$$\Im\Sigma(\mathbf{k},\hbar\omega) = \frac{1}{\hbar}\frac{1}{V}\sum_{\mathbf{K}}[n_F(\xi(\mathbf{K}-\mathbf{k})) + n_b(\xi(\mathbf{K}-\mathbf{k})+\hbar\omega)] \times \Im[T^{MB}(\mathbf{K},\xi(\mathbf{K}-\mathbf{k})+\hbar\omega^+)]. \quad (4.17)$$

Using the optical theorem $\Im[T^{MB}(\mathbf{K},\hbar\omega)] = \Im[\Xi(\mathbf{K},\hbar\omega)]|T^{MB}(\mathbf{K},\hbar\omega)|^2$, we can rewrite Eq. (4.17) as

$$\Im\Sigma(\mathbf{k},\hbar\omega) = -\frac{\pi}{\hbar V^2}\sum_{\mathbf{k_2},\mathbf{k_3},\mathbf{k_4}} \delta(\hbar\omega+\xi(\mathbf{k_2})-\xi(\mathbf{k_3})-\xi(\mathbf{k_4}))\delta_{\mathbf{k}+\mathbf{k_2},\mathbf{k_3}+\mathbf{k_4}} \times |T^{MB}(\mathbf{k}+\mathbf{k_2},\hbar\omega+\xi(\mathbf{k_2}))|^2[n_2(1-n_3)(1-n_4)+(1-n_2)n_3n_4], \quad (4.18)$$

where we again used the shorthand notation $n_i = n_F(\xi(\mathbf{k}_i))$. Since $\Im\Sigma$ is a single-particle relaxation rate, we see that this rate is exactly the sum of the in and out rates for the state with momentum $\mathbf{k}$ and energy $\hbar\omega$ as would be obtained from a Fermi's golden rule expression. After some rewriting, we arrive at the following expression for $\Im\Sigma$

$$n_F(\omega)(1-n_F(\omega))\Im\Sigma(\mathbf{k},\hbar\omega) = \frac{m}{8\pi^2 k\hbar^3}\int_R d(\hbar\Omega)dK \times \frac{|T^{MB}(K,\hbar\Omega)|^2}{\sinh^2(\beta\hbar\Omega/2)}[1-n_F(\hbar\Omega-\hbar\omega)-n_F(\hbar\omega)]\Im[\Xi(K,\hbar\Omega^+)], \quad (4.19)$$

which is a convenient starting point for numerical evaluation. The integration range R is restricted by the following inequalities

$$2\mu+\hbar\omega-\frac{1}{2}\epsilon(K)>0 \quad \text{and} \quad \mu+\hbar\Omega-\hbar\omega>0 \quad (4.20)$$

and

$$|\sqrt{\epsilon(k)}-\sqrt{\mu+\hbar\Omega-\hbar\omega}| < \sqrt{\epsilon(K)} < \sqrt{\epsilon(k)}+\sqrt{\mu+\hbar\Omega-\hbar\omega}, \quad (4.21)$$

where we defined $\epsilon(k) = \hbar^2k^2/2m$. Then, the real part of the self-energy is obtained by a Kramers-Kronig transform

$$\Re\Sigma(\mathbf{k},\hbar\omega) = \frac{1}{\pi}\int d\omega' \frac{\Im\Sigma(\mathbf{k},\hbar\omega)}{\omega'-\omega}. \quad (4.22)$$

In the next subsection, we show the results for the spectral function and spin-transport coefficients obtained by evaluating Eqs. (4.19) and (4.22).

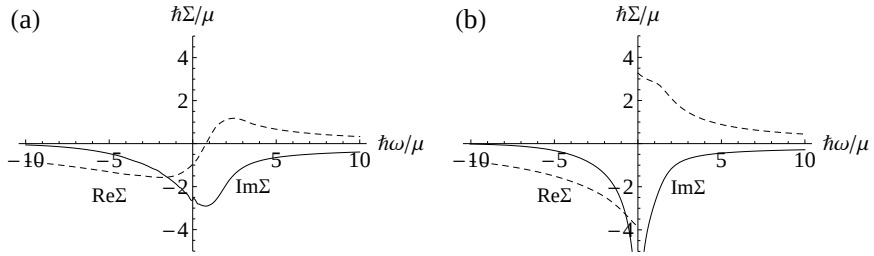

Figure 4.4: The imaginary (solid line) and real (dashed line) parts of the self-energy at unitarity for $\hbar k = \sqrt{2m\mu}$ for $k_B T/\mu = 1$ (a) and $T = T_c$ (b).

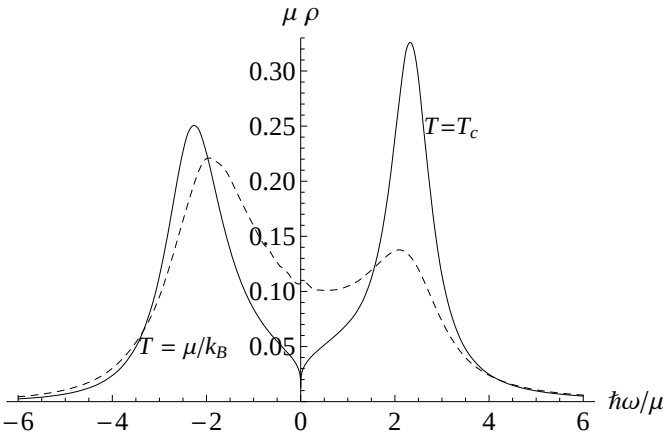

Figure 4.5: The spectral function ρ at unitarity for $\hbar k = \sqrt{2m\mu}$ for $k_B T/\mu = 1$ (dashed line) and $T = T_c$ (solid line).

4.3.3 Results

By evaluating Eqs. (4.19) and (4.22) numerically, we obtain Fig. 4.4 where we show the imaginary (solid line) and real (dashed line) parts of the self-energy for a typical momentum $\hbar k = \sqrt{2m\mu}$ at unitarity. Part (a) of Fig. 4.4 shows the results far from the transition at $T = \mu/k_B \approx 1.5T_c$, and part (b) of Fig. 4.4) shows the results at the transition $T = T_c$. From Fig. 4.4 we see that upon approaching the transition, a divergence develops at $\omega = 0$ in the imaginary part of the self-energy and a corresponding discontinuity in the real part. Closer inspection shows that the imaginary part divergences logarithmically. When $\Im\Sigma$ diverges as $a\log(\Delta\omega)$, with $\Delta\omega$ the distance from the pole, the resulting jump in the real part is πa. For general $\mathbf{k}$, the position of the divergence is $\hbar\omega = -\xi(\mathbf{k})$, which can be understood as follows: $\Im\Sigma(\mathbf{k}, \hbar\omega)$ describes the scattering rate for an excitation with momentum $\mathbf{k}$ and energy $\hbar\omega$. When, $\hbar\omega = -\xi(\mathbf{k})$ the excitation can form a Cooper pair with a particle from the medium with momentum $-\mathbf{k}$ and energy $\xi(\mathbf{k})$. As a check, we may also obtain the logarithmic divergence analytically. The divergence is caused by the development of a pole at $\Omega = 0$ and $K = 0$ in Eq. (4.19). For small Ω and K, $T^{MB} \propto 1/(a_1\Omega + a_2K^2 + a_3(T - T_c) + ia_4\Omega)$ (with the a_i's real) while the rest of the integrand is linear in K. Integration over Ω and K then yields a divergence $\log(T - T_c)$. In contrast, for small Ω and K the integrand in the Bolzmann case Eq. (4.6) goes as K^2. Integration shows that there is then no divergence, as was shown in Fig. 4.1.

From Eq. (4.10) we see that a divergence of $\Im\Sigma$ will lead to a suppression of the spectral function ρ. Indeed in Fig. 4.5 we show the spectral function ρ at unitarity for $\hbar k = \sqrt{2m\mu}$, for $k_BT/\mu = 1$ (dashed line) and $T = T_c$ (solid line). Already quite far from the transition at $T = \mu/k_B \approx 1.5T_c$, interactions cause a suppression of the spectral weight close to $\omega = 0$, which moves into peaks on both sides of $\omega = 0$ in order to keep the sum rule satisfied. At $T = T_c$, this suppression is maximal, and here ρ vanishes logarithmically as $|\omega| \to 0$.

In Fig. 4.6 we show the solution of the equation of state $n = \int d(\hbar\omega)n_F(\omega)\nu(\omega)$ for μ. The dashed line corresponds to the non-interacting result, which was used to obtain the Boltzmann results in Fig. 4.1. The solid line is the solution of the number equation at unitarity, which terminates at the critical temperature $T_c = 0.29T_F$. The difference of this value for T_c with the mean-field value for T_c at unitarity $T_c = 0.5T_F$ used in Sec. 4.2 is that there, we used the non-interacting equation of state. That μ is lower than the non-interacting value is intuitively clear: an attractive interaction will lower the energy of the atoms and thus μ must also be lowered in order to keep the number of particles the same.

In Fig. 4.7 we show the density of states ν versus ω. The dashed curve is the non-interacting result at $T = 0$, which goes as $\nu \propto \sqrt{\omega - \epsilon_F}$. The solid curve is the result at unitarity at $T = T_c$. We see that the suppressed spectral weight around

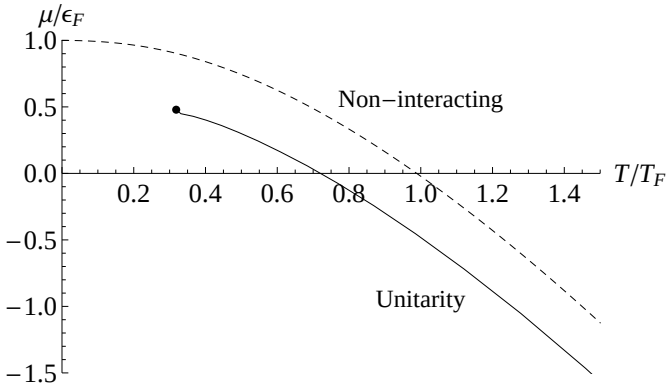

Figure 4.6: The solution of the number equation giving μ as a function of temperature. The dashed line is the non interacting result. The solid line gives the result at unitarity.

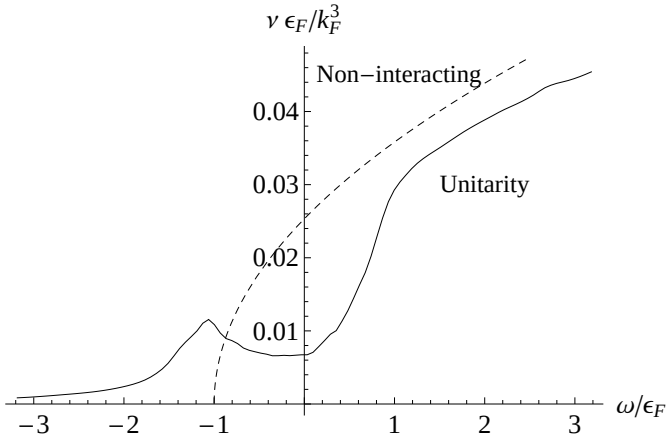

Figure 4.7: The density of states ν versus ω. The dashed curve is the non-interacting result, while the solid curve correspond to the unitarity case.

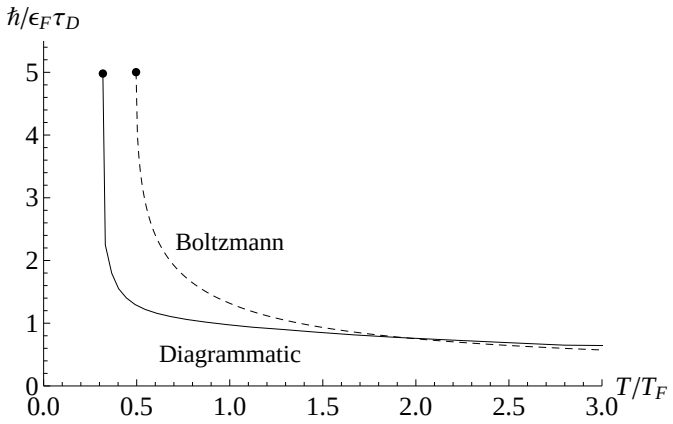

Figure 4.8: The spin-transport relaxation rate $1/\tau_D$ as a function of temperature at unitarity. The dashed line is the Boltzmann result, the solid line the diagrammatic result obtained by evaluating Eq. (4.14).

$\omega = 0$ leads to a greatly reduced density of states, a so-called pseudogap. We note that since T_c is not particularly low, the spectral functions are never very sharply peaked, and the density of states remains nonzero in the pseudogap in agreement with the results of Ref. [59].

In Fig. 4.8 we show the spin-transport relaxation rate obtained by evaluating Eq. (4.14) at unitarity as the solid line. The dashed line is the unitarity result from the Boltzmann calculation (the top line in Fig. 4.1). Since both lines are determined using different equations of state, they terminate at different T_c's. Similarly, in Fig. 4.9 we show the spin-diffusion constant. The dashed line is the unitarity result from the Boltzmann calculation (the bottom line in Fig 4.2), while the solid line is obtained by evaluating the spin susceptibility in Eq. (4.15) and using the Einstein relation to find D_s.

In Fig. 4.10 we show the spin susceptibility χ_s obtained by evaluating Eq. (4.15) scaled by the non-interacting zero-temperature value $\chi_0 = 3n/2\epsilon_F$ as the solid line. The dashed line corresponds to the non-interacting result. We see that for large temperatures the lines converge, and that our result shows a downturn close to T_c. This downturn is expected physically, since the magnetic response should diminish, when $\uparrow$ and $\downarrow$ spins become more correlated [60].

4.4 Conclusions and discussion

We have determined the spin-diffusion constant and the spin-transport relaxation rate using a Boltzmann approach and a diagrammatic approach at unitarity, as

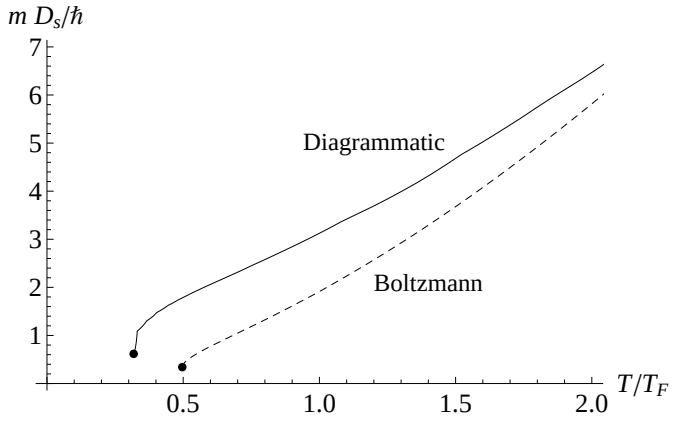

Figure 4.9: The spin-diffusion constant D_s as a function of temperature at unitarity. The dashed line is the Boltzmann result, the solid line the diagrammatic result obtained by evaluating the spin susceptibility in Eq. (4.15) and using the Einstein relation.

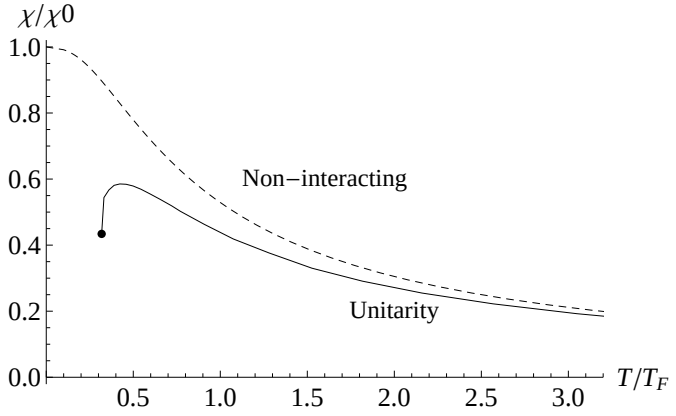

Figure 4.10: We show the spin susceptibility obtained by evaluating Eq. (4.15) scaled by the non-interacting zero-temperature value $\chi_0 = 3n/2\epsilon_F$ as the solid line. The dashed line corresponds to the non-interacting result. The solid curve terminates at the critical temperature $T_c = 0.29T_F$.

shown in Figs. 4.8 and 4.9. On a diagrammatic level, the Boltzmann calculation takes into account vertex corrections, while our diagrammatic approach does not. Oppositely, the diagrammatic approach takes into account pseudogap physics which suppresses the spectral weight close to the Fermi level, while the Boltzmann approach does not. Surprisingly, we find qualitatively equivalent behavior for both transport coefficients using these approaches. Seemingly, pseudogap physics and vertex corrections are not of critical importance when evaluating these transport coefficients close to the BCS transition. To research this claim further, vertex corrections appropriate to the self-energy we used should be evaluated.

Chapter 5

Boltzmann-transport theory for the drag resistivity close to a phase transition

We present a generic Boltzmann-transport theory for the drag resistivity ρ_{D} in systems close to a second-order phase transition. We find general expressions for ρ_{D} in two and three spatial dimensions, for arbitrary density and mass imbalance, for particle- and hole-like bands, and show how to incorporate the effect of gaussian critical fluctuations close to a phase transition. As an application, we use our formalism to determine the spin drag relaxation rate in an ultracold Fermi gas with repulsive interactions close the a ferromagnetic transition.

5.1 Introduction

The behavior of linear-response transport coefficients close to a phase transition has always been an interesting field of study. Two prime examples being the vanishing of the resistivity at the superconducting transition or the divergence of the magnetic susceptibility at a ferromagnetic transition. Indeed, the behavior of these coefficients is often the most important experimental signature in assessing whether or not the system has reached an ordered state. Any deviation of the standard low-temperature T^2 dependence indicates non-Fermi liquid behavior.

However, in condensed-matter systems, the theoretical calculation of these coefficients is often very hard, due to many competing phenomena: electron-phonon coupling, presence of impurities, localization, and Coulomb interaction between the carriers can all influence their behavior. The prime advantage of a drag experiment is that it singles out the effect of Coulomb interaction on a transport

This chapter is based on: Boltzmann-transport theory for the drag resistivity close to a phase transition: from ultracold Fermi gases near a Stoner instability to spatially-separated electron-hole systems close to exciton condensation, M. P. Mink, Arnaud Raoux, H. T. C. Stoof, Marco Polini, G. Vignale, and R. A. Duine, to be submitted.

coefficient. Consider a system consisting of two layers, separated by a barrier so that tunneling between the layers is absent. In a drag experiment in this bilayer system, a current is run in one of the layers, denoted as the drive layer. Due to momentum relaxation, the carriers in the other (the passive) layer are dragged along and a voltage drop is observed. The drag resistivity is the ratio between the current density in the active layer and the electric field in the passive layer. Due to the spatial separation of the layers, the Coulomb interaction between carriers in both layers can be singled out as the responsible for this effect, which for this reason is called Coulomb drag. In cold two-component Fermi gases a similar phenomenon can be observed, where now the two spin species play the role of the carriers in the two layers. When the cloud of atoms with a spin state moves relative to the other, due to momentum relaxation by the atomic interaction, the other spin species is dragged along: spin drag.

Coulomb drag was first observed in 1990 [2] for electron-electron bilayers and later also for electron-hole bilayers [8], for a review see Ref. [39]. In electron-hole bilayers the electrons in one layer and holes in the other can form excitons, which are expected to condense for low enough temperatures. The behavior of the drag resistivity in this ordered state was considered [43] and also its use as a precursor for this transition [42]. An enhancement of the drag resistivity was measured experimentally [40, 41], although it is not sure that the enhancement was indeed caused by exciton condensation. Also for a topological insulated film, an enhancement of the drag resistivity was predicted close to the (in this case topological) exciton condensation [58]. For ultracold fermions with repulsive interactions, enhancement of the drag resistivity was predicted close to the ferromagnetic transition [51], and for ultracold bosons close to Bose-Einstein condensation [55]. The latter has recently indeed been observed experimentally [64].

In this work we derive a general result for the drag resistivity using quantum kinetic theory and Fermi's golden rule for the scattering amplitudes. Our theory is valid for both two and three dimensions, for particle- and hole-like bands, and arbitrary imbalance in density and mass. We show how to choose the appropriate decoupling channel to include the effect of gaussian critical fluctuations close to a transition. In Section 5.2 we start by considering the Boltzmann equation for a single species as an introduction of our formalism. In Section 5.3 we solve the Boltzmann equation coupled between the two species and find an expression for the drag resistivity in terms of the collision integral. We derive a general expression for this collision integral in Section 5.4. Our results for quadratic-dispersion systems are given in Section 5.5 and for linear-dispersion systems in Section 5.6. Our conclusions are in Section 5.8 and the appendix in Section 5.9.

5.2 Single species results

We start by specifying the single-particle dispersion relations that we will use:

$$\xi_s(\boldsymbol{k}) = s(\hbar^2 k^2/2m - \mu) \quad \text{or} \quad \xi_s(\boldsymbol{k}) = s(\hbar v k - \mu) \ , \tag{5.1}$$

for a quadratic and linear dispersion, respectively. When the band is "particle-like" $s = 1$ and when the band is "hole-like" $s = -1$. Alternatively, we will say that for $s = 1$ the band has a positive character and for $s = -1$ a negative character. Note that when $s = -1$ the μ we introduce is actually minus the chemical potential.

Before writing two coupled Boltzmann equations to calculate the drag resistivity, it is instructive to consider the ordinary resistivity of a single species. To determine this resistivity, we need to determine the non-equilibrium carrier distribution f in the presence of a force $\boldsymbol{F}$. The time derivative is

$$\frac{d}{dt} f(\boldsymbol{k}(t)) = \dot{\boldsymbol{k}} \cdot \partial_{\boldsymbol{k}} f(\boldsymbol{k}) \ . \tag{5.2}$$

In the relaxation time approximation, we add a phenomenological term which relaxes f back to the equilibrium Fermi-Dirac distribution on a time scale τ. Under the influence of a force $\boldsymbol{F}$, we have $\hbar\dot{\boldsymbol{k}} = \boldsymbol{F}$. Then, for a steady-state solution

$$\frac{1}{\hbar}\boldsymbol{F} \cdot \partial_{\boldsymbol{k}} f(\boldsymbol{k}) = -\frac{1}{\tau}[f(\boldsymbol{k}) - n_{\mathrm{F}}(\xi_s(\boldsymbol{k}))] \ , \tag{5.3}$$

where $\xi_s(\boldsymbol{k})$ is the bare dispersion introduced above and $n_{\mathrm{F}}(\epsilon) = 1/(1 + \exp(\beta\epsilon))$ is the Fermi-Dirac distribution with $\beta = (k_{\mathrm{B}}T)^{-1}$ the inverse temperature.

We are interested in linear-response transport coefficients, so we take as an Ansatz for the solution of Eq. (5.3) the first-order expansion of a Fermi-Dirac distribution shifted by a drift momentum $\boldsymbol{k}^{\mathrm{drift}}$:

$$\begin{aligned} f(\boldsymbol{k}) &= n_{\mathrm{F}}[\xi(\boldsymbol{k} - s\boldsymbol{k}^{\mathrm{drift}})] \\ &= n_{\mathrm{F}}[\xi_s(\boldsymbol{k})] - s[\boldsymbol{k}^{\mathrm{drift}} \cdot \partial_{\boldsymbol{k}} \xi_s(\boldsymbol{k})] \ n'_{\mathrm{F}}[\xi_s(\boldsymbol{k})] \\ &\equiv n_{\mathrm{F}}(\xi(\boldsymbol{k})) + f^{(1)}(\boldsymbol{k}) \ , \end{aligned} \tag{5.4}$$

where the prime on n_{F} means differentiation with respect to the argument. The inclusion of the extra factor s before $\boldsymbol{k}^{\mathrm{drift}}$ in the argument of n_{F} makes sure that the total momentum $\boldsymbol{P}$ in a species is indeed in the direction of $\boldsymbol{k}^{\mathrm{drift}}$. Indeed, we find that for both $s = 1$ as $s = -1$

$$\boldsymbol{P} = \sum_{\boldsymbol{k}} \hbar \boldsymbol{k} f^{(1)}(\boldsymbol{k}) = \hbar \boldsymbol{k}^{\mathrm{drift}} n V \ . \tag{5.5}$$

where V is the volume. The quantity n is the carrier density, i.e., the number of electrons when $s = 1$ and the number of holes when $s = -1$.

We also need the evaluate the current density $\boldsymbol{j}$:

$$\boldsymbol{j} = \frac{1}{V\hbar}\sum_{\boldsymbol{k}}[\partial_{\boldsymbol{k}}\xi(\boldsymbol{k})]f^{(1)}(\boldsymbol{k}) \ . \tag{5.6}$$

Introducing the momentum-to-current conversion factor C

$$C = -\frac{1}{dV\hbar}\sum_{\boldsymbol{k}}[\partial_{\boldsymbol{k}}\xi(\boldsymbol{k})]^2 \ n'_{\rm F}(\xi_s(\boldsymbol{k})) \ , \tag{5.7}$$

where d is the dimensionality, we obtain $\boldsymbol{j} = sC\boldsymbol{k}^{\rm drift}$. The conversion factor is easily determined to be

$$C = \frac{\hbar n}{m} \quad \text{or} \quad C = \frac{\mu}{4\pi\hbar} \ , \tag{5.8}$$

for a quadratic and linear dispersion, respectively.

Using these definitions, we solve the Boltzmann equation Eq. (5.3) which in the linear response approximation reads

$$\frac{1}{\hbar}\boldsymbol{F}\cdot\partial_{\boldsymbol{k}}n_{\rm F}(\xi(\boldsymbol{k})) = -\frac{1}{\tau}f^{(1)}(\boldsymbol{k}) \ . \tag{5.9}$$

Performing the differentiation with respect to $\boldsymbol{k}$ leads to $\boldsymbol{k}^{\rm drift} = s(\tau/\hbar)\boldsymbol{F}$ and $\boldsymbol{F} = (\hbar/C\tau)\boldsymbol{j}$, from which we identify the resistivity $\boldsymbol{F} = \rho\boldsymbol{j}$ as

$$\rho = \frac{m}{n\tau} \quad \text{and} \quad \rho = \frac{4\pi\hbar^2}{\mu\tau} \ , \tag{5.10}$$

for a quadratic and linear dispersion, respectively. For the quadratic dispersion we recognize the familiar Drude result. We note that these resistivities are positive, also for hole-like bands. To understand this, one needs to realize that when $s = -1$ a force will actually induce a momentum density in the opposite direction, as explained in Fig. 5.1. The fact that the momentum direction and current direction are opposite for $s = -1$ gives an extra minus sign, so that the particle current will be in the same direction as the force, as indicated by the positive resistivity.

5.3 Drag resistivity and coupled Boltzmann equations

In this Section we first introduce and then solve two coupled Boltzmann equations that describe the drag resistivity. We denote the two species by the pseudospin label $\sigma = \uparrow, \downarrow$ which can either be hyperfine spin for the case of cold Fermi gases or layer index in the case of double-layer systems. The dispersions in Eq. (5.1) acquire the species label σ and are

$$\xi_\sigma(\boldsymbol{k}) = s_\sigma(\hbar^2k^2/2m_\sigma - \mu_\sigma) \quad \text{or} \quad \xi_\sigma(\boldsymbol{k}) = s_\sigma(\hbar vk - \mu_\sigma) \ , \tag{5.11}$$

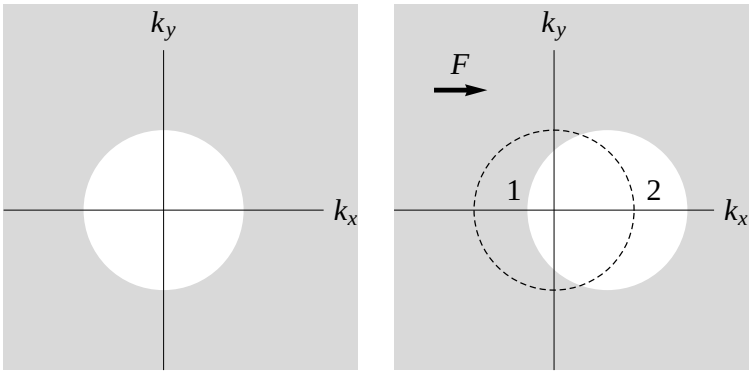

Figure 5.1: Left: The Fermi sphere for a negative dispersion in equilibrium. White corresponds to empty states, gray to filled states. Right: the shifted Fermi sea after application of a force $\boldsymbol{F}$ to the right. The equilibrium Fermi sphere is indicated by the dashed line. Note that the momentum density due to this force is in the opposite direction of this force to the left. The states is area 1 are now filled and carry a momentum to the left, while the sates in area 2 are now empty and carry a momentum to the right.

for the quadratic and linear dispersion, respectively. Note that we allow for a mass "imbalance" (i.e. $m_\uparrow \neq m_\downarrow$) and density imbalance (i.e. $\mu_\uparrow \neq \mu_\downarrow$). We will denote the number of degenerate fermion types in a species by g, which will always be equal for both species. For example, in an electron-hole double-layer, $g = 2$, because both layers have spin degeneracy. In double-layer graphene (two graphene sheets separated by a tunnel barrier), $g = 4$, due to the presence of spin degeneracy and two Dirac cones in each layer. The density n_σ is always the density of a single fermion type, the total density of species σ is gn_σ and the total carrier density in the system $g(n_\uparrow + n_\downarrow)$. We apply a species-dependent force $\boldsymbol{F}_\sigma$ so that the equivalent of the linearized Boltzmann equation in Eq. (5.9) is the following system of two coupled equations:

$$\frac{1}{\hbar}\boldsymbol{F}_\uparrow \cdot \partial_{\boldsymbol{k}} n_F(\xi_\uparrow(\boldsymbol{k})) = -\frac{1}{\tau_\uparrow} f_\uparrow^{(1)}(\boldsymbol{k}) + \Gamma_\uparrow(\boldsymbol{k}) \tag{5.12}$$

$$\frac{1}{\hbar}\boldsymbol{F}_\downarrow \cdot \partial_{\boldsymbol{k}} n_F(\xi_\downarrow(\boldsymbol{k})) = -\frac{1}{\tau_\downarrow} f_\downarrow^{(1)}(\boldsymbol{k}) + \Gamma_\downarrow(\boldsymbol{k}) \ , \tag{5.13}$$

where we introduced species-dependent intra-species relaxation times τ_σ. The $\Gamma_\sigma(\boldsymbol{k})$ are the collision integrals which give the net flux into the state $\boldsymbol{k}$ of species σ. We will specify them in the next section. We substitute the expressions for $f_\sigma^{(1)}$

to introduce the drift momenta $\boldsymbol{k}_\sigma^{\rm drift}$

$$\left[\frac{1}{\hbar}\boldsymbol{F}_\uparrow - \frac{s_\uparrow}{\tau_\uparrow}\boldsymbol{k}_\uparrow^{\rm drift}\right]\cdot[\partial_{\boldsymbol{k}}\xi_\uparrow(\boldsymbol{k})]n'_{\rm F}(\xi_\uparrow(\boldsymbol{k})) = \Gamma_\uparrow(\boldsymbol{k}) \tag{5.14}$$

$$\left[\frac{1}{\hbar}\boldsymbol{F}_\downarrow - \frac{s_\downarrow}{\tau_\downarrow}\boldsymbol{k}_\downarrow^{\rm drift}\right]\cdot[\partial_{\boldsymbol{k}}\xi_\downarrow(\boldsymbol{k})]n'_{\rm F}(\xi_\downarrow(\boldsymbol{k})) = \Gamma_\downarrow(\boldsymbol{k})\ . \tag{5.15}$$

To make connection to the current density, we multiply with the group velocity and sum over $\boldsymbol{k}$ with the result

$$-C_\uparrow\left[\frac{1}{\hbar}\boldsymbol{F}_\uparrow - \frac{s_\uparrow}{\tau_\uparrow}\boldsymbol{k}_\uparrow^{\rm drift}\right] = \boldsymbol{\Gamma}_\uparrow \tag{5.16}$$

$$-C_\downarrow\left[\frac{1}{\hbar}\boldsymbol{F}_\downarrow - \frac{s_\downarrow}{\tau_\downarrow}\boldsymbol{k}_\downarrow^{\rm drift}\right] = \boldsymbol{\Gamma}_\downarrow\ , \tag{5.17}$$

where we defined $\boldsymbol{\Gamma}_\sigma = (1/V\hbar)\sum_{\boldsymbol{k}}(\partial_{\boldsymbol{k}}\xi_\sigma(\boldsymbol{k}))\Gamma_\sigma(\boldsymbol{k})$.

Below, we find to first order in the drift momenta $\boldsymbol{\Gamma}_\uparrow = g^2(s_\uparrow\Gamma_\uparrow^{\rm S}\boldsymbol{k}_\uparrow^{\rm drift} + s_\downarrow\Gamma^{\rm D}\boldsymbol{k}_\downarrow^{\rm drift})$ and $\boldsymbol{\Gamma}_\downarrow = g^2(s_\downarrow\Gamma_\downarrow^{\rm S}\boldsymbol{k}_\downarrow^{\rm drift} + s_\uparrow\Gamma^{\rm D}\boldsymbol{k}_\uparrow^{\rm drift})$, where S (D) stands for "same" ("different") and we note that the coefficients for the cross dependence are equal in both relations. After substituting these expansions, we can easily obtain the resistivity matrix relating $\boldsymbol{F}$ to $\boldsymbol{j}$

$$\begin{pmatrix}\boldsymbol{F}_\uparrow\\ \boldsymbol{F}_\downarrow\end{pmatrix} = \begin{pmatrix}\rho_{\uparrow\uparrow} & \rho_{\uparrow\downarrow}\\ \rho_{\downarrow\uparrow} & \rho_{\downarrow\downarrow}\end{pmatrix}\begin{pmatrix}\boldsymbol{j}_\uparrow\\ \boldsymbol{j}_\downarrow\end{pmatrix}, \tag{5.18}$$

with the drag resistivity $\rho_{\rm D} \equiv \rho_{\downarrow\uparrow} = \rho_{\uparrow\downarrow} = -g\hbar\Gamma^D/C_\downarrow C_\uparrow$. The intraspecies resistivities are $\rho_{\sigma\sigma} = \hbar/gC_\sigma\tau_\sigma - g\hbar\Gamma_\sigma^S/C_\sigma^2$. When the collision integrals are zero, $\rho_{\sigma\sigma}$ reduces to the result obtained in the previous Section for the single-species problem and $g = 1$.

5.4 Collision Integral

In this Section we determine the collision integral $\boldsymbol{\Gamma}_\sigma$. We start with the expression for the scattering rate from Fermi's golden rule and expand it to first order in the drift momenta. Let $\uparrow, \boldsymbol{k}_1$ and $\downarrow, \boldsymbol{k}_2$ be the incoming states, which are scattered onto the final states $\downarrow, \boldsymbol{k}_3$ and $\uparrow, \boldsymbol{k}_4$. The rate for this process can be calculated from Fermi's golden rule

$$R = \frac{2\pi g^2}{\hbar V^2}|W(\boldsymbol{k}_1,\boldsymbol{k}_2,\boldsymbol{k}_3,\boldsymbol{k}_4)|^2\delta_{\boldsymbol{k}_1+\boldsymbol{k}_2,\boldsymbol{k}_3+\boldsymbol{k}_4}\delta(\xi_\uparrow(\boldsymbol{k}_1)+\xi_\downarrow(\boldsymbol{k}_2)-\xi_\downarrow(\boldsymbol{k}_3)-\xi_\downarrow(\boldsymbol{k}_4)) \times f_\uparrow(\boldsymbol{k}_1)f_\downarrow(\boldsymbol{k}_2)(1-f_\downarrow(\boldsymbol{k}_3))(1-f_\uparrow(\boldsymbol{k}_4))\ . \tag{5.19}$$

For chiral electron systems described by a massless Dirac equation, such as electrons in double-layer graphene or topological insulator thin films, we should multiply the r.h.s. of the previous equation with the following form factors

$$\frac{1+\cos(\phi_4-\phi_1)}{2}\frac{1+\cos(\phi_3-\phi_2)}{2}\ , \tag{5.20}$$

where ϕ_i is the angle of $\boldsymbol{k}_i$, which encode suppressed backscattering for $J=1$ chiral electron systems. For simplicity, we will drop these factors in the manipulations carried out in this Section, and reinstate them when we consider systems with a linear dispersions in Section 5.6.

To make our manipulations more tractable, we introduce some shorthands: for $i=1,4$ we have $\xi_i=\xi_\uparrow(\boldsymbol{k}_i)$ and $f_i=f_\uparrow(\boldsymbol{k}_i)$, and for $i=2,3$ we have $\xi_i=\xi_\downarrow(\boldsymbol{k}_i)$ and $f_i=f_\downarrow(\boldsymbol{k}_i)$. Furthermore, the delta-function expressing the conservation of momentum ($\delta_{\boldsymbol{k}_1+\boldsymbol{k}_2,\boldsymbol{k}_3+\boldsymbol{k}_4}$) will be indicated by $\delta_{\boldsymbol{k}_i}$, while the one expressing the conservation of energy ($\delta(\xi_\uparrow(\boldsymbol{k}_1)+\xi_\downarrow(\boldsymbol{k}_2)-\xi_\downarrow(\boldsymbol{k}_3)-\xi_\downarrow(\boldsymbol{k}_4))$) by $\delta(\xi_i)$. Using this new notation and dropping the arguments of the many-particle scattering amplitude W, the rate R becomes

$$R=\frac{2\pi g^2}{\hbar V^2}\delta_{\boldsymbol{k}_i}\delta(\xi_i)|W|^2 f_1 f_2(1-f_3)(1-f_4). \tag{5.21}$$

For concreteness, we will now determine the collision integral for the $\uparrow$-species. The expression for the $\downarrow$-species can be easily obtained by appropriate changing of the labels. The net flow into the state $\uparrow,\boldsymbol{k}$ which is $\Gamma_\uparrow(\boldsymbol{k})$ is then

$$\Gamma_\uparrow(\boldsymbol{k})=\sum_{\boldsymbol{k}_1,\boldsymbol{k}_2,\boldsymbol{k}_3,\boldsymbol{k}_4} R(\delta_{\boldsymbol{k}_4,\boldsymbol{k}}-\delta_{\boldsymbol{k}_1,\boldsymbol{k}}). \tag{5.22}$$

The expression for $\boldsymbol{\Gamma}_\uparrow$ is then

$$\begin{aligned}\boldsymbol{\Gamma}_\uparrow&=\frac{g^2}{V\hbar}\sum_{\boldsymbol{k}}(\partial_{\boldsymbol{k}}\xi_\uparrow(\boldsymbol{k}))\Gamma_\uparrow(\boldsymbol{k})\\&=\frac{2\pi}{\hbar^2V^3}\sum_{\boldsymbol{k}_i}\delta_{\boldsymbol{k}_i}\delta(\xi_i)|W|^2 f_1 f_2(1-f_3)(1-f_4)(\partial_{\boldsymbol{k}}\xi_4-\partial_{\boldsymbol{k}}\xi_1),\end{aligned} \tag{5.23}$$

where $\sum_{\boldsymbol{k}_i}$ is a shorthand for $\sum_{\boldsymbol{k}_1,\boldsymbol{k}_2,\boldsymbol{k}_3,\boldsymbol{k}_4}$ and where $\partial_{\boldsymbol{k}}\xi_i\equiv[\partial_{\boldsymbol{k}}\xi_\uparrow(\boldsymbol{k})]_{\boldsymbol{k}=\boldsymbol{k}_i}$ and $\partial_{\boldsymbol{k}}\xi_i\equiv[\partial_{\boldsymbol{k}}\xi_\downarrow(\boldsymbol{k})]_{\boldsymbol{k}=\boldsymbol{k}_i}$ for $i=1,4$ and $i=2,3$, respectively.

We perform the first-order expansion in the drift momenta $\boldsymbol{k}_\sigma^{\mathrm{drift}}$ of the distribution functions f_σ and obtain to first order in the $f_\sigma^{(1)}$'s

$$f_1f_2(1-f_3)(1-f_4)\to n_1n_2(1-n_3)(1-n_4)\left(\frac{f_1^{(1)}}{n_1}+\frac{f_2^{(1)}}{n_2}-\frac{f_3^{(1)}}{1-n_3}-\frac{f_4^{(1)}}{1-n_4}\right), \tag{5.24}$$

where we dropped the zeroth-order term since it evaluates to zero in the momentum summation. In the previous equation we introduced the shorthand $n_i = n_{\mathrm{F}}(\xi_i)$. Substituting Eq. (5.24) and the expression for $f_\sigma^{(1)}$ from Eq. (5.4) in Eq. (5.23) and using that $n'_{\mathrm{F}}(\epsilon) = -\beta n_{\mathrm{F}}(\epsilon)[1 - n_{\mathrm{F}}(\epsilon)]$ yields ultimately

$$\begin{aligned}\boldsymbol{\Gamma}_\uparrow = \frac{2\pi\beta g^2}{\hbar^2 V^3}\sum_{\boldsymbol{k}_i}\delta_{\boldsymbol{k}_i}\delta(\xi_i)|W|^2 n_1 n_2(1-n_3)(1-n_4)(\partial_{\boldsymbol{k}}\xi_4 - \partial_{\boldsymbol{k}}\xi_1)\\ \times\left[s_\uparrow \boldsymbol{k}_\uparrow^{\mathrm{drift}}\cdot(\partial_{\boldsymbol{k}}\xi_1(1-n_1) - \partial_{\boldsymbol{k}}\xi_4 n_4) + s_\downarrow \boldsymbol{k}_\downarrow^{\mathrm{drift}}\cdot(\partial_{\boldsymbol{k}}\xi_2(1-n_2) - \partial_{\boldsymbol{k}}\xi_3 n_3)\right] .\end{aligned} \tag{5.25}$$

When we interchange the labels of the incoming and outgoing states (specifically, when we transform $\boldsymbol{k}_1 \leftrightarrow \boldsymbol{k}_4$ and $\boldsymbol{k}_2 \leftrightarrow \boldsymbol{k}_3$), $\boldsymbol{\Gamma}_\uparrow$ remains invariant. Taking the original expression for $\boldsymbol{\Gamma}_\uparrow$ and the transformed one, taking the average, and using that due to energy conservation $n_1 n_2(1-n_3)(1-n_4) = n_4 n_3(1-n_2)(1-n_1)$ and that the interaction W remains invariant under this transformation, yields

$$\begin{aligned}\boldsymbol{\Gamma}_\uparrow = -\frac{\pi\beta g^2}{\hbar^2 V^3}\sum_{\boldsymbol{k}_i}\delta_{\boldsymbol{k}_i}\delta(\xi_i)|W|^2 n_1 n_2(1-n_3)(1-n_4)(\partial_{\boldsymbol{k}}\xi_4 - \partial_{\boldsymbol{k}}\xi_1)\\ \times\left[s_\uparrow \boldsymbol{k}_\uparrow^{\mathrm{drift}}\cdot(\partial_{\boldsymbol{k}}\xi_4 - \partial_{\boldsymbol{k}}\xi_1) + s_\downarrow \boldsymbol{k}_\downarrow^{\mathrm{drift}}\cdot(\partial_{\boldsymbol{k}}\xi_3 - \partial_{\boldsymbol{k}}\xi_2)\right] .\end{aligned} \tag{5.26}$$

In the Appendix (Section 5.9) we show that we may take the drift momenta out of the summation provided that we introduce a factor $1/d$, so that we obtain the anticipated result

$$\boldsymbol{\Gamma}_\uparrow = g^2(s_\uparrow \Gamma_\uparrow^{\mathrm{S}} \boldsymbol{k}_\uparrow^{\mathrm{drift}} + s_\downarrow \Gamma^{\mathrm{D}} \boldsymbol{k}_\downarrow^{\mathrm{drift}}) \tag{5.27}$$

$$\boldsymbol{\Gamma}_\downarrow = g^2(s_\downarrow \Gamma_\downarrow^{\mathrm{S}} \boldsymbol{k}_\downarrow^{\mathrm{drift}} + s_\uparrow \Gamma^{\mathrm{D}} \boldsymbol{k}_\uparrow^{\mathrm{drift}}) , \tag{5.28}$$

where we again remark that the cross contributions have the same coefficient Γ^D. The explicit expressions for these coefficients are

$$\Gamma_\uparrow^{\mathrm{S}} = -\frac{\pi\beta}{d\hbar^2 V^3}\sum_{\boldsymbol{k}_i}\delta_{\boldsymbol{k}_i}\delta(\xi_i)|W|^2 n_1 n_2(1-n_3)(1-n_4)(\partial_{\boldsymbol{k}}\xi_4 - \partial_{\boldsymbol{k}}\xi_1)^2 , \tag{5.29}$$

$$\Gamma_\downarrow^{\mathrm{S}} = -\frac{\pi\beta}{d\hbar^2 V^3}\sum_{\boldsymbol{k}_i}\delta_{\boldsymbol{k}_i}\delta(\xi_i)|W|^2 n_1 n_2(1-n_3)(1-n_4)(\partial_{\boldsymbol{k}}\xi_3 - \partial_{\boldsymbol{k}}\xi_2)^2 , \tag{5.30}$$

and

$$\Gamma^{\mathrm{D}} = -\frac{\pi\beta}{d\hbar^2 V^3}\sum_{\boldsymbol{k}_i}\delta_{\boldsymbol{k}_i}\delta(\xi_i)|W|^2 n_1 n_2(1-n_3)(1-n_4)(\partial_{\boldsymbol{k}}\xi_4 - \partial_{\boldsymbol{k}}\xi_1)\cdot(\partial_{\boldsymbol{k}}\xi_3 - \partial_{\boldsymbol{k}}\xi_2) . \tag{5.31}$$

We note that these results and the expression for the drag resistivity $\rho_{\mathrm{D}} = -\hbar\Gamma^D/C_\downarrow C_\uparrow$ are valid for two and three dimensions, for a quadratic dispersion,

for particle- and hole-like bands, and arbitrary density and mass imbalance. We, however, remind the reader that if we consider a system where the carriers have a linear dispersion, we should reinstate the from factors shown in Eq. (5.20).

We now comment on the signs of Γ^{D} and ρ_{D}. We stress that ρ_{D} is the transport coefficient relating the particle (and not the charge) current to the force. The sign of Γ^{D} is $s_\uparrow s_\downarrow$, as can be seen by considering a quadratic dispersion, so that the sign of ρ_{D} is $-s_\uparrow s_\downarrow$. Consider the situation in which there is a finite current in the "active" $\uparrow$ species $\boldsymbol{j}_\uparrow$, and that the current in the passive $\downarrow$ species is held to zero by the force $\boldsymbol{F}_\downarrow$, so that $\boldsymbol{F}_\downarrow = \rho_{\mathrm{D}} \boldsymbol{j}_\uparrow$. Recall that the intra-species resistivities are positive for both particle- and hole-like bands. For bands of equal character, the current in the active layer would induce in current in the passive layer in the same direction. This tendency is countered by a force $\boldsymbol{F}_\downarrow$ in the opposite direction since the intra-species resistivity is positive. Thus, for bands of equal character, ρ_{D} is negative. When one of the bands is particle-like and the other hole-like, the current in the active layer will want to induce a current in the opposite direction in the passive layer, so that ρ_{D} is positive.

It is interesting to consider the relations between $\Gamma^{\mathrm{S}}_{\uparrow,\downarrow}$ and Γ^{D}. For a quadratic dispersion we substitute Eq. (5.11) into Eqs. (5.29,5.30,5.31) and obtain

$$\boldsymbol{\Gamma}_\uparrow = -s_\uparrow m_\downarrow |\Gamma^{\mathrm{D}}| \left(\frac{\boldsymbol{k}^{\mathrm{drift}}_\uparrow}{m_\uparrow} - \frac{\boldsymbol{k}^{\mathrm{drift}}_\downarrow}{m_\downarrow} \right) \tag{5.32}$$

$$\boldsymbol{\Gamma}_\downarrow = -s_\downarrow m_\uparrow |\Gamma^{\mathrm{D}}| \left(\frac{\boldsymbol{k}^{\mathrm{drift}}_\downarrow}{m_\downarrow} - \frac{\boldsymbol{k}^{\mathrm{drift}}_\uparrow}{m_\uparrow} \right) . \tag{5.33}$$

When, $\boldsymbol{k}^{\mathrm{drift}}_\uparrow/m_\uparrow = \boldsymbol{k}^{\mathrm{drift}}_\downarrow/m_\downarrow$ the integrated collision integral vanishes and the resistivities are just given by the decoupled single-species result. The condition is satisfied when the drift velocities have the same magnitude, and the drift momenta have the same direction. This is what one expects for a Galilean invariant system. For the case of a linear dispersion the Hamiltonian is not Galilean invariant and we have not been able to find a simple relation between the $\Gamma^{\mathrm{S}}_\sigma$ and Γ^{D}.

5.4.1 Decoupling channels

The purpose of this Chapter is to show how to determine the collision integral Γ^{D} in Eq. (5.31) incorporating the effect of gaussian critical fluctuations close to a phase transition. In the case of a ferromagnetic transition these are magnetic fluctuations, while in the case of superconductivity or exciton condensation, these are pairing fluctuations. These fluctuations increase in strength when the system approaches the transition and ultimately lead to a divergence of the scattering amplitude at the critical temperature. To conveniently account for these fluctuations we should "decouple" Eq. (5.31) in the correct "channel". This decoupling is

Instability channel	Combination	$\hbar\omega$	$\boldsymbol{k}_p$
Hartree	In $\uparrow$ with Out $\uparrow$	$\xi_1 - \xi_4$	$\boldsymbol{k}_1 - \boldsymbol{k}_4 \equiv \boldsymbol{q}$
Fock	In $\uparrow$ with Out $\downarrow$	$\xi_1 - \xi_3$	$\boldsymbol{k}_1 - \boldsymbol{k}_3 \equiv \boldsymbol{Q}$
Cooper	In $\uparrow$ with In $\downarrow$	$\xi_1 + \xi_2$	$\boldsymbol{k}_1 + \boldsymbol{k}_2 \equiv \boldsymbol{K}$

Table 5.1: Overview of the three decoupling channels. In the third and fourth columns we specify the energy and momentum variables appropriate for this decoupling channel.

carried out by introducing an auxiliary energy variable $\hbar\omega$ through an integral over $\hbar\omega$ and "solving" the momentum-conserving Kronecker delta with $\boldsymbol{k}$, $\boldsymbol{k}'$, and $\boldsymbol{k}_\mathrm{p}$ in such a way that the pole in the scattering amplitude lies at $\hbar\omega = 0$ and $\boldsymbol{k}_p = \boldsymbol{0}$. For example, in the case of superconductivity between two bands with positive character, the pole in the scattering amplitude (in this case it is usually called the "many-body T-matrix") lies at zero energy and zero center-of-mass momentum of the two incoming particles $\hbar\omega = \xi_1 + \xi_2 = 0$ and $\boldsymbol{k}_\mathrm{p} = \boldsymbol{k}_1 + \boldsymbol{k}_2 = \boldsymbol{0}$. Thus, in this specific case, we would introduce ω as follows

$$\delta(\xi_1 + \xi_2 - \xi_3 - \xi_4) = \int d(\hbar\omega)\ \delta(\xi_1 + \xi_2 - \hbar\omega)\delta(\xi_3 + \xi_4 - \hbar\omega)\ . \tag{5.34}$$

The three possibilities of combining the incoming $\uparrow$ particle with energy ξ_1 with i) the incoming $\downarrow$ particle with energy ξ_2, ii) the outgoing $\downarrow$ particle with energy ξ_3, and iii) the outgoing $\uparrow$ particle with energy ξ_4, are denoted as decoupling in the Cooper, Fock, and Hartree channels, respectively. We summarize the properties of these decoupling channels in Table 5.1.

In the next Section, we discuss how to perform the decoupling of Eq. (5.31) in the three channels in full detail for a quadratic dispersion. These results will be valid for arbitrary space dimensionality, band character, mass, and density imbalance. In Section 5.6 we consider a linear dispersion and restrict ourselves to the calculation of Eq. (5.31) in a system with exciton-condensation, i.e., the decoupling of Eq. (5.31) in the Fock channel for bands of opposite character. Then, in Section 5.7 we use our formalism to determine the spin drag relaxation rate in an ultracold Fermi gas with repulsive interactions close the a ferromagnetic transition.

5.5 Quadratic Dispersion

For a quadratic dispersion, Eq. (5.31) simplifies to

$$\Gamma^\mathrm{D} = s_\uparrow s_\downarrow \frac{\pi\beta}{dV^3}\frac{\hbar^2}{m_\uparrow m_\downarrow}\sum_{\boldsymbol{k}_i}\delta_{\boldsymbol{k}_i}\delta(\xi_i)|W|^2 n_1 n_2(1-n_3)(1-n_4)(\boldsymbol{k}_1 - \boldsymbol{k}_4)^2\ , \tag{5.35}$$

where we note that $\boldsymbol{k}_1 - \boldsymbol{k}_4$ is just the momentum transferred in the scattering event. Although not of fundamental importance, we make an important working remark. For any form of the scattering amplitude W, all three decoupling channels should give the same result for Γ^D. We can explicitly check their agreement when W is a constant. This remark provides a powerful checking tool for the, sometimes lengthy, analytical results presented below.

5.5.1 Hartree decoupling

When the effective interaction W depends mostly on the transferred energy $\hbar\omega = \xi_1 - \xi_4$ and momentum $\boldsymbol{k}_\mathrm{p} = \boldsymbol{k}_1 - \boldsymbol{k}_4 \equiv \boldsymbol{q}$ in the scattering event, the Hartree channel is the appropriate decoupling channel. We introduce an additional integral over the $\hbar\omega$ using the identity

$$\delta(\xi_1 + \xi_2 - \xi_3 - \xi_4) = \int d(\hbar\omega)\ \delta(\xi_1 - \xi_4 - \hbar\omega) \times \delta(\xi_2 - \xi_3 + \hbar\omega)\ ,$$

and solve the delta-function for momentum conservation by writing $\boldsymbol{k}_1 = \boldsymbol{k}$, $\boldsymbol{k}_2 = \boldsymbol{k}'$, $\boldsymbol{k}_3 = \boldsymbol{k}' + \boldsymbol{q}$, and $\boldsymbol{k}_4 = \boldsymbol{k} - \boldsymbol{q}$, so that the $\boldsymbol{k}$ and $\boldsymbol{k}'$ summations in Eq. (5.35) decouple:

$$\begin{aligned}\Gamma^\mathrm{D} = s_\uparrow s_\downarrow \frac{\pi\beta\hbar^2}{dVm_\uparrow m_\downarrow} \sum_{\boldsymbol{q}} \int d(\hbar\omega)\ q^2\ |W(\boldsymbol{q},\hbar\omega)|^2 \\ \times \frac{1}{V}\sum_{\boldsymbol{k}} \delta(\xi_\uparrow(\boldsymbol{k}) - \xi_\uparrow(\boldsymbol{k}-\boldsymbol{q}) - \hbar\omega) n_\mathrm{F}(\xi_\uparrow(\boldsymbol{k}))[1 - n_\mathrm{F}(\xi_\uparrow(\boldsymbol{k}-\boldsymbol{q}))] \\ \times \frac{1}{V}\sum_{\boldsymbol{k}'} \delta(\xi_\downarrow(\boldsymbol{k}') - \xi_\downarrow(\boldsymbol{k}'+\boldsymbol{q}) + \hbar\omega) n_\mathrm{F}(\xi_\downarrow(\boldsymbol{k}'))[1 - n_\mathrm{F}(\xi_\downarrow(\boldsymbol{k}'+\boldsymbol{q}))]\ .\end{aligned} \tag{5.36}$$

This expression can be rewritten as

$$\Gamma^D = s_\uparrow s_\downarrow \frac{\beta\hbar^2}{4d\pi Vm_\uparrow m_\downarrow} \sum_{\boldsymbol{q}} \int d\hbar\omega \frac{q^2|W(\boldsymbol{q},\hbar\omega)|^2}{\sinh^2(\beta\hbar\omega/2)} \Im m\Pi_\uparrow(\boldsymbol{q},\hbar\omega)\Im m\Pi_\downarrow(\boldsymbol{q},\hbar\omega)\ , \tag{5.37}$$

where we have introduced the well-known polarizability (Lindhard function)

$$\Pi_\sigma(\boldsymbol{q},\hbar\omega) = \frac{1}{V}\sum_{\boldsymbol{k}} \frac{n_\mathrm{F}(\xi_\sigma(\boldsymbol{k}+\boldsymbol{q})) - n_\mathrm{F}(\xi_\sigma(\boldsymbol{k}))}{\xi_\sigma(\boldsymbol{k}+\boldsymbol{q}) - \xi_\sigma(\boldsymbol{k}) - \hbar\omega - i0^+}, \tag{5.38}$$

and we used that $\Pi_\sigma(\boldsymbol{q},\hbar\omega) = \Pi_\sigma(-\boldsymbol{q},\hbar\omega)$ and $\Pi_\sigma(\boldsymbol{q},-\hbar\omega) = \Pi^*_\sigma(\boldsymbol{q},\hbar\omega)$.

Next, we show how to determine Π. It will turn out that in three dimensions we may find an analytical expression for $\Im m\Pi$, while in two dimensions we will be left with a numerical integral. First, we note that $\Pi_\sigma(\boldsymbol{q},\hbar\omega)$ does not depend on

the character of the band s_σ, so that we may drop it, effectively setting $s_\sigma = 1$. Taking the imaginary part of Eq. (5.38) and shifting $\boldsymbol{k}$ by $\boldsymbol{q}/2$ leads to

$$\begin{aligned}\Im m\Pi_\sigma(\boldsymbol{q}, \hbar\omega) = \frac{\pi}{V}\sum_{\boldsymbol{k}} \delta(\hbar^2 kq\cos(\theta)/m_\sigma - \hbar\omega) \\ \times \left[n_F(\xi_\sigma(\boldsymbol{k}+\boldsymbol{q}/2)) - n_F(\xi_\sigma(\boldsymbol{k}-\boldsymbol{q}/2))\right],\end{aligned} \tag{5.39}$$

where θ is the angle between $\boldsymbol{k}$ and $\boldsymbol{q}$. In three dimensions, we choose $\boldsymbol{q}$ along the z-axis, so that θ is the polar angle of $\boldsymbol{k}$. In two dimensions, we choose $\boldsymbol{q}$ along the x-axis so that θ is the angle between $\boldsymbol{k}$ and the x-axis. The delta function has a solution when

$$k \geq \frac{m_\sigma|\hbar\omega|}{\hbar^2 q} \equiv k_{\min}, \tag{5.40}$$

where we defined the lower bound $k_{\min}$ for the k integration. We solve the δ for the angle θ and find

$$\begin{aligned}\Im m\Pi_\sigma(\boldsymbol{q}, \hbar\omega) = \frac{\pi}{(2\pi)^d}\int_{k_{\min}}^{\infty} dk H_d(k) \\ \times \left[n_F\left(\epsilon_\sigma(k) + \epsilon_\sigma(q/2) - \mu_\sigma + \hbar\omega/2\right) - n_F\left(\epsilon_\sigma(k) + \epsilon_\sigma(q/2) - \mu_\sigma - \hbar\omega/2\right)\right],\end{aligned} \tag{5.41}$$

where we define the kinetic energy $\epsilon_\sigma(k) = \hbar^2k^2/2m_\sigma$ and the function $H_d(k)$ depends on the dimensionality

$$H_2(k) = \frac{2k}{\sqrt{\hbar^4k^2q^2/m_\sigma^2 - \hbar^2\omega^2}} \quad \text{and} \quad H_3(k) = \frac{2\pi k m_\sigma}{\hbar^2 q}. \tag{5.42}$$

In the three dimensional case, we may evaluate this integral exactly, leading to

$$\begin{aligned}\Im m\Pi_\sigma(\boldsymbol{q}, \hbar\omega) = -\frac{m_\sigma^2}{4\pi\hbar^4\beta q}\{\beta\hbar\omega \\ + \log\left[1 + \exp\left(\beta(\epsilon_\sigma(q/2) + m_\sigma\omega^2/2q^2 - \hbar\omega/2 - \mu_\sigma)\right)\right] \\ - \log\left[1 + \exp\left(\beta(\epsilon_\sigma(q/2) + m_\sigma\omega^2/2q^2 + \hbar\omega/2 - \mu_\sigma)\right)\right]\}.\end{aligned} \tag{5.43}$$

In the two dimensional case, we must resort to numerical methods to determine $\Im m\Pi_\sigma$. Substitution of the result for $\Im m\Pi_\sigma$ into Eq. (5.37) leads to our final expression for Γ^D after decoupling in the Hartree channel. The real part of Π_σ which is typically present in the interaction W can be obtained by a Kramers-Kronig transform of $\Im m\Pi_\sigma$. We note that since Π is an intraspecies quantity, the presence of imbalance in the chemical potential or mass does not make the determination of Π_σ more difficult.

5.5.2 Cooper decoupling

When the effective interaction W depends mostly on the center-of-mass momentum $\boldsymbol{K} = \boldsymbol{k}_1 + \boldsymbol{k}_2$ and total energy $\hbar\omega = \xi_1 + \xi_2$ of the incoming particles, the Cooper channel is the most appropriate channel to decouple the collision integral (5.35). In this case we thus introduce the energy variable $\hbar\omega$ using the identity

$$\delta(\xi_1 + \xi_2 - \xi_3 - \xi_4) = \int d(\hbar\omega)\ \delta(\xi_1 + \xi_2 - \hbar\omega)\delta(\xi_3 + \xi_4 - \hbar\omega)\ , \tag{5.44}$$

and solve the delta-function of momentum conservation by setting $\boldsymbol{k}_1 = \boldsymbol{K}/2 + \boldsymbol{k}$, $\boldsymbol{k}_2 = \boldsymbol{K}/2 - \boldsymbol{k}$, $\boldsymbol{k}_3 = \boldsymbol{K}/2 - \boldsymbol{k}'$, and $\boldsymbol{k}_4 = \boldsymbol{K}/2 + \boldsymbol{k}'$. We find:

$$\begin{aligned}\Gamma^{\mathrm{D}} = s_\uparrow s_\downarrow \frac{\pi\beta\hbar^2}{dV^3 m_\uparrow m_\downarrow} \sum_{\boldsymbol{k},\boldsymbol{k}',\boldsymbol{K}} & |W(\boldsymbol{K},\hbar\omega)|^2 (\boldsymbol{k}' - \boldsymbol{k})^2 \\ & \times \delta(\xi_\uparrow(\boldsymbol{K}/2 + \boldsymbol{k}) + \xi_\downarrow(\boldsymbol{K}/2 - \boldsymbol{k}) - \hbar\omega) \\ & \times n_{\mathrm{F}}(\xi_\uparrow(\boldsymbol{K}/2 + \boldsymbol{k}))n_{\mathrm{F}}(\xi_\downarrow(\boldsymbol{K}/2 - \boldsymbol{k})) \\ & \times \delta(\xi_\uparrow(\boldsymbol{K}/2 + \boldsymbol{k}') + \xi_\downarrow(\boldsymbol{K}/2 - \boldsymbol{k}') - \hbar\omega) \\ & \times [1 - n_{\mathrm{F}}(\xi_\uparrow(\boldsymbol{K}/2 + \boldsymbol{k}'))][1 - n_F(\xi_\downarrow(\boldsymbol{K}/2 - \boldsymbol{k}'))]\ .\end{aligned} \tag{5.45}$$

Expanding the factor $(\boldsymbol{k}' - \boldsymbol{k})^2$ we can decouple the $\boldsymbol{k}$ and $\boldsymbol{k}'$ summations and obtain

$$\begin{aligned}\Gamma^{\mathrm{D}} = s_\uparrow s_\downarrow \frac{\beta\hbar^2}{2\pi dV m_\uparrow m_\downarrow} \int d(\hbar\omega) \sum_{\boldsymbol{K}} \frac{|W(\boldsymbol{K},\hbar\omega)|^2}{\sinh^2(\beta\hbar\omega/2)} \\ \times [\Im m\ \Xi_0(\boldsymbol{K},\hbar\omega)\Im m\ \Xi_2(\boldsymbol{K},\hbar\omega) - \Im m\ \Xi_1^2(\boldsymbol{K},\hbar\omega)],\end{aligned} \tag{5.46}$$

where we have introduced the following three "generalized pairing susceptibilities" ($n = 0, 1$, and 2)

$$\Im m\ \Xi_n(\boldsymbol{K},\hbar\omega) = \frac{1}{V}\Im m \sum_{\boldsymbol{k}} C_n(\boldsymbol{k}) \frac{1 - n_{\mathrm{F}}(\xi_\uparrow(\boldsymbol{k} + \boldsymbol{K}/2)) - n_{\mathrm{F}}(\xi_\downarrow(\boldsymbol{k} - \boldsymbol{K}/2))}{\hbar\omega + i0^+ - (\xi_\uparrow(\boldsymbol{k} + \boldsymbol{K}/2) + \xi_\downarrow(\boldsymbol{k} - \boldsymbol{K}/2))}\ . \tag{5.47}$$

Here $C_0(\boldsymbol{k}) = 1$, $C_1(\boldsymbol{k}) = \boldsymbol{k}$, and $C_2(\boldsymbol{k}) = |\boldsymbol{k}|^2$. Note that we introduced a minor abuse of notation for the sake of accessibility of our formalism: although $\Im m\Xi_1$ and C_1 are vector valued functions, they are printed in plain face. In determining the susceptibility Ξ, we restrict ourselves to the case of bands of equal character $s_\uparrow = s_\downarrow = 1$. It will turn out that the case $s_\uparrow = -s_\downarrow$ can be obtained by considering the susceptibility Δ defined in Eq. (5.61), obtained by performing the Fock decoupling in the case that the bands have equal character $s_\uparrow = s_\downarrow$. We will show this point explicitly in the next subsection in which we perform the Fock decoupling.

To determine the generalized susceptibilities it is convenient to make a shift of the summation variable $\boldsymbol{k}$ such that the denominator in Eq. (5.47) becomes independent of the angle θ between $\boldsymbol{k}$ and $\boldsymbol{K}$. We do not need to shift the $\boldsymbol{k}$ as argument of the C_n's, as can be seen by making the shift for both $\boldsymbol{k}$ and $\boldsymbol{k}'$ in Eq. (5.45) before expanding the factor $(\boldsymbol{k}' - \boldsymbol{k})^2$. The result is

$$\Im m\Xi_n(\boldsymbol{K}, \hbar\omega) = \frac{1}{V}\Im m \sum_{\boldsymbol{k}} C_n(\boldsymbol{k}) \frac{1 - n_F(\xi_\uparrow(\boldsymbol{k} + R_\uparrow \boldsymbol{K})) - n_F(\xi_\downarrow(\boldsymbol{k} - R_\downarrow \boldsymbol{K}))}{\hbar\omega + i0 - (\xi_\uparrow(\boldsymbol{k} + R_\uparrow \boldsymbol{K}) + \xi_\downarrow(\boldsymbol{k} - R_\downarrow \boldsymbol{K}))}, \tag{5.48}$$

where $R_\sigma = m_\sigma/(m_\uparrow + m_\downarrow)$ and $R_\uparrow + R_\downarrow = 1$. We convert the summation to an integration and introduce the delta function

$$\begin{aligned}\Im m\Xi_n(\boldsymbol{K}, \hbar\omega) = & -\frac{\pi}{(2\pi)^d}\Im m \int d\boldsymbol{k}^d C_n(\boldsymbol{k}) \\ & \times [1 - n_F(\xi_\uparrow(\boldsymbol{k} + R_\uparrow \boldsymbol{K})) - n_F(\xi_\downarrow(\boldsymbol{k} - R_\downarrow \boldsymbol{K}))] \\ & \times \delta(\mu_\uparrow + \mu_\downarrow + \hbar\omega - (\hbar^2/2)(k^2/m_\uparrow + k^2/m_\downarrow + K^2/(m_\uparrow + m_\downarrow))),\end{aligned} \tag{5.49}$$

where we choose $\boldsymbol{K}$ along the x-axis in the two dimensional case and $\boldsymbol{K}$ along the z-axis in the three dimensional case, and where we noted that $\Im m\Xi_1(\boldsymbol{K}, \hbar\omega)$ can only have a component in the direction of $\boldsymbol{K}$. The solution of the delta function is

$$k_0 = \frac{1}{\sqrt{\hbar^2/2m_\uparrow + \hbar^2/2m_\downarrow}} \sqrt{\mu_\uparrow + \mu_\downarrow + \hbar\omega - \frac{\hbar^2 K^2}{2(m_\uparrow + m_\downarrow)}}. \tag{5.50}$$

This solution only exists when

$$K^2 \leq \frac{\mu_\uparrow + \mu_\downarrow + \hbar\omega}{\hbar^2/2(m_\uparrow + m_\downarrow)} \equiv K_{\max}^2, \tag{5.51}$$

which gives an upper bound for the length of $\boldsymbol{K}$ in Eq. (5.46). For $K > K_{max}$ the imaginary part of Ξ is zero. We solve the delta function and take into account the Jacobian and the transformation rule for the delta function, which leads for the three dimensional case to

$$\begin{aligned}\Im m\Xi_n(\boldsymbol{K}, \hbar\omega) = & \frac{-\pi}{(2\pi)^2} \int_0^\pi d\theta C_n(\boldsymbol{k}) \\ & \frac{k_0^2 \sin(\theta)}{2k_0(\hbar^2/2m_\uparrow + \hbar^2/2m_\downarrow)} [1 - n_F(E_\uparrow(\theta)) - n_F(E_\downarrow(\theta))].\end{aligned} \tag{5.52}$$

The expression for the two dimensional case, differs in the Jacobian and the upper

integration boundary for θ

$$\Im m\Xi_n(\boldsymbol{K},\hbar\omega) = \frac{-\pi}{(2\pi)^2}\int_0^{2\pi} d\theta C_n(\boldsymbol{k}) \\ \frac{k_0}{2k_0(\hbar^2/2m_\uparrow+\hbar^2/2m_\downarrow)}[1-n_F(E_\uparrow(\theta))-n_F(E_\downarrow(\theta))]. \quad (5.53)$$

We defined the energies

$$E_\uparrow(\theta) = \hbar^2k_0^2/2m_\uparrow+m_\uparrow\hbar^2K^2/2(m_\uparrow+m_\downarrow)^2+\cos(\theta)\hbar^2k_0K/2(m_\uparrow+m_\downarrow)-\mu_\uparrow \quad (5.54)$$

and

$$E_\downarrow(\theta) = \hbar^2k_0^2/2m_\downarrow+m_\downarrow\hbar^2K^2/2(m_\uparrow+m_\downarrow)^2-\cos(\theta)\hbar^2k_0K/2(m_\uparrow+m_\downarrow)-\mu_\downarrow. \quad (5.55)$$

Using the integrals

$$\int_0^\pi d\theta\frac{\sin(\theta)}{1+\exp(a+b\cos(\theta))} = 2+\frac{1}{b}\log\left[\frac{1+\exp(a-b)}{1+\exp(a+b)}\right], \quad (5.56)$$

and

$$\int_0^\pi d\theta\frac{\cos(\theta)\sin(\theta)}{1+\exp(a+b\cos(\theta))} \\ = -\frac{1}{b}\log\left[(1+\exp(a-b))(1+\exp(a+b))\right] \\ +\frac{1}{b^2}\left(\mathrm{Li}_2(-\exp(a-b))-\mathrm{Li}_2(-\exp(a+b))\right), \quad (5.57)$$

where $\mathrm{Li}_s(z)=\sum_{k=1}^\infty z^k/k^s$ is the polylogarithm, we can determine $\Im m\Xi_n(\boldsymbol{K},\hbar\omega)$ for the three dimensional case in closed form. However, the resulting expressions are not very enlightening and will not be given explicitly. Substitution of the results for $\Im m\Xi_n$ into Eq. (5.46) leads to our final expression for Γ^D after decoupling in the Cooper channel.

5.5.3 Fock decoupling

When the interaction depends mostly on the energy and momentum difference of the incoming $\uparrow$ particle and outgoing $\downarrow$ particle, the Fock channel is the appropriate channel to decouple the collision integral Eq. (5.35). We introduce this energy variable $\hbar\omega=\xi_1-\xi_3$ using the identity

$$\delta(\xi_1+\xi_2-\xi_3-\xi_4) = \int d\hbar\omega\delta(\xi_1-\xi_3-\hbar\omega)\delta(\xi_2-\xi_4+\hbar\omega), \quad (5.58)$$

and this momentum variable $\boldsymbol{Q} = \boldsymbol{k}_1 - \boldsymbol{k}_3$ by solving the momentum conserving delta function by $\boldsymbol{k}_1 = \boldsymbol{k} + \boldsymbol{Q}$, $\boldsymbol{k}_2 = \boldsymbol{k}'$, $\boldsymbol{k}_3 = \boldsymbol{k}$, and $\boldsymbol{k}_4 = \boldsymbol{k}' + \boldsymbol{Q}$. Then, we have for Γ^D

$$\begin{aligned}\Gamma^D = s_\uparrow s_\downarrow \frac{\pi\beta\hbar^2}{dV^3 m_\uparrow m_\downarrow} \sum_{\boldsymbol{k},\boldsymbol{k}',\boldsymbol{Q}} \int d\hbar\omega |W(\boldsymbol{Q},\hbar\omega)|^2 (\boldsymbol{k}'-\boldsymbol{k})^2 \\ \times \delta(\xi_\uparrow(\boldsymbol{k}+\boldsymbol{Q}) - \xi_\downarrow(\boldsymbol{k}) - \hbar\omega) n_F(\xi_\uparrow(\boldsymbol{k}+\boldsymbol{Q}))(1-n_F(\xi_\downarrow(\boldsymbol{k}))) \\ \times \delta(\xi_\downarrow(\boldsymbol{k}') - \xi_\uparrow(\boldsymbol{k}'+\boldsymbol{Q}) + \hbar\omega) n_F(\xi_\downarrow(\boldsymbol{k}'))(1-n_F(\xi_\uparrow(\boldsymbol{k}'+\boldsymbol{Q}))). \quad (5.59)\end{aligned}$$

We will again expand the factor $(\boldsymbol{k}' - \boldsymbol{k})^2$ and obtain

$$\begin{aligned}\Gamma^D = s_\uparrow s_\downarrow \frac{\beta\hbar^2}{2\pi dV m_\uparrow m_\downarrow} \sum_{\boldsymbol{Q}} \int d\hbar\omega \frac{|W(\boldsymbol{Q},\hbar\omega)|^2}{\sinh^2(\beta\hbar\omega/2)} \\ \times [\Im m\Delta_0(\boldsymbol{Q},\hbar\omega)\Im m\Delta_2(\boldsymbol{Q},\hbar\omega) - \Im m\Delta_1^2(\boldsymbol{Q},\hbar\omega)], \quad (5.60)\end{aligned}$$

where we defined the shorthand

$$\Im m\Delta_n(\boldsymbol{Q},\hbar\omega) = \frac{1}{V}\Im m \sum_{\boldsymbol{k}} C_n(\boldsymbol{k}) \frac{n_F(\xi_\uparrow(\boldsymbol{k}+\boldsymbol{Q})) - n_F(\xi_\downarrow(\boldsymbol{k}))}{\xi_\uparrow(\boldsymbol{k}+\boldsymbol{Q}) - \xi_\downarrow(\boldsymbol{k}) - \hbar\omega - i0}, \quad (5.61)$$

where again $C_0(\boldsymbol{k}) = 1$, $C_1(\boldsymbol{k}) = \boldsymbol{k}$, and $C_2(\boldsymbol{k}) = |\boldsymbol{k}|^2$. Now, we compare the susceptibilities for the Cooper and the Fock channel, Ξ and Δ, respectively. Defining $\tilde{\xi}_\downarrow(k) = -\xi_\downarrow(k)$ we rewrite the fraction in Eq. (5.61) as

$$\frac{1 - n_F(\xi_\uparrow(\boldsymbol{k}+\boldsymbol{Q})) - n_F(\tilde{\xi}_\downarrow(\boldsymbol{k}))}{\hbar\omega + i0 - \xi_\uparrow(\boldsymbol{k}+\boldsymbol{Q}) - \tilde{\xi}_\downarrow(\boldsymbol{k})}, \quad (5.62)$$

which is exactly the fraction of $\Xi_n(\boldsymbol{Q},\hbar\omega)$ in Eq. (5.47) with a switched sign for the $\downarrow$-dispersion. Thus, when determining Ξ and Δ, we can restrict ourselves to the case $s_\uparrow = s_\downarrow = 1$. When we need Ξ or Δ for dispersions of opposite sign, these are just obtained by considering the other susceptibility for bands of the same character $s_\uparrow = s_\downarrow = 1$.

Following up on the remarks made above, we now determine Δ for bands of the same character $s_\uparrow = s_\downarrow = 1$. The way the analysis proceeds depends on whether or not there is mass imbalance. The reason is that when $m_\uparrow = m_\downarrow$ the terms with k^2 cancel from the denominator of the integrand of Eq. (5.61), whereas they do not in the mass imbalanced case. Since the imbalanced case is less important for our purposes here, we will only consider the fully balanced case with $m_\uparrow = m_\downarrow \equiv m$ and $\mu_\uparrow = \mu_\downarrow \equiv \mu$. Shifting $\boldsymbol{k}$ with $\boldsymbol{Q}/2$, we arrive at

$$\begin{aligned}\Im m\Delta_n(\boldsymbol{Q},\hbar\omega) = \frac{\pi}{(2\pi)^d}\Im m \int d\boldsymbol{k}^d C_n(\boldsymbol{k}) \\ \times [n_F(\xi_\uparrow(\boldsymbol{k}+\boldsymbol{Q}/2)) - n_F(\xi_\downarrow(\boldsymbol{k}-\boldsymbol{Q}/2))]\delta((\hbar^2 kQ/m)\cos(\theta) - \hbar\omega), \quad (5.63)\end{aligned}$$

where θ is the angle between $\boldsymbol{k}$ and $\boldsymbol{Q}$. In three dimensions, we choose $\boldsymbol{Q}$ along the z-axis, so that θ is the polar angle of $\boldsymbol{k}$. In two dimensions, we choose $\boldsymbol{Q}$ along the x-axis so that θ is the angle between $\boldsymbol{k}$ and the x-axis. The argument of the delta function is the same as in the Hartree case in Eq. (5.39). The difference with that calculation is that apart from $\Im m\Delta_0$, we also need to determine $\Im m\Delta_1$, and $\Im m\Delta_2$. Using the results from the Hartree calculation, we arrive at the result

$$\Im m\Delta_n(\boldsymbol{Q},\hbar\omega) = \frac{\pi}{(2\pi)^d}\int_{k_{\min}}^{\infty} dk F_{n,d}(k) \\ \times \left[n_F\left(\epsilon(k)+\epsilon(Q/2)-\mu+\hbar\omega/2\right) n_F\left(\epsilon(k)+\epsilon(Q/2)-\mu-\hbar\omega/2\right)\right], \quad (5.64)$$

where $\epsilon(k) = \hbar^2k^2/2m$ and where we recall that $k_{\min} = m_\sigma|\hbar\omega|/\hbar^2Q$. The functions $F_{0,d}$ depend on the dimensionality have the same form as the function $H_d(k)$ defined in Eq. (5.42)

$$F_{0,2}(k) = \frac{2k}{\sqrt{\hbar^4k^2Q^2/m^2-\hbar^2\omega^2}} \quad \text{and} \quad F_{0,3}(k) = \frac{2\pi km}{\hbar^2Q}. \quad (5.65)$$

Then, $F_{1,d}(k)$ and $F_{2,d}(k)$ are related to these as follows $F_{1,d}(k) = (\omega m/\hbar Q)F_{0,d}(k)$ and $F_{2,d}(k) = k^2F_{0,d}(k)$. In the three dimensional case, one can find closed form expressions for the Δ_n using the following integrals

$$\int dk \frac{k}{1+\exp(a(b+k^2))} = \frac{k^2}{2} - \frac{1}{2a}\log(1+\exp(a(b+k^2))), \quad (5.66)$$

and

$$\int dk \frac{k^3}{1+\exp(a(b+k^2))} \\ = \frac{k^4}{4} - \frac{k^2}{2a}\log(1+\exp(a(b+k^2))) - \frac{1}{2a^2}\mathrm{Li}_2(-\exp(a(b+k^2))). \quad (5.67)$$

where $\mathrm{Li}_s(z)$ the polylogarithm defined below Eq. (5.57). These expressions are, however, not particularly insightful and will not be shown explicitly.

5.6 Linear Dispersion

For a linear dispersion, Eq. (5.31) simplifies to

$$\Gamma^D = -s_\uparrow s_\downarrow \frac{1}{4}\frac{\pi\beta v^2}{dV^3}\sum_{\boldsymbol{k}_i}\delta_{\boldsymbol{k}_i}\delta(\xi_i)|W|^2n_1n_2(1-n_3)(1-n_4) \\ \times(\hat{\boldsymbol{k}}_4-\hat{\boldsymbol{k}}_1)\cdot(\hat{\boldsymbol{k}}_3-\hat{\boldsymbol{k}}_2)\left(1+\hat{\boldsymbol{k}}_1\cdot\hat{\boldsymbol{k}}_4\right)\left(1+\hat{\boldsymbol{k}}_2\cdot\hat{\boldsymbol{k}}_3\right) \quad (5.68)$$

where we reinstated the form factors $\left(1+\hat{\boldsymbol{k}}_1\cdot\hat{\boldsymbol{k}}_4\right)\left(1+\hat{\boldsymbol{k}}_2\cdot\hat{\boldsymbol{k}}_3\right)$ mentioned in Sec. 5.4. The main purpose of this section is to derive the expressions given in Ref. [58], where the drag resistivity was determined in a topological insulator thin film close to (topological) exciton condensation. Then, $s_\uparrow = 1$ and $s_\uparrow = -1$ and the appropriate decoupling channel for this transition is the Fock channel. For comparison, we will also perform the decoupling of Eq. (5.68) in the Hartree channel.

In Ref. [58], we used an approximation for Γ^D in which the form factors were set to unity. The effect of the form factors is the suppression of backscattering: $1+\hat{\boldsymbol{k}}_1\cdot\hat{\boldsymbol{k}}_4$ vanishes when $\boldsymbol{k}_1$ and $\boldsymbol{k}_4$ are directed oppositely. The pole in the scattering amplitude W for the case of exciton condensation occurs at $\boldsymbol{Q} = \boldsymbol{k}_1 - \boldsymbol{k}_3 = 0$. The motivation for this approximation is that the condition for backscattering $\hat{\boldsymbol{k}}_1\cdot\hat{\boldsymbol{k}}_4 = -1$ is largely independent with the value of $\boldsymbol{Q}$. In other words, the suppression of backscattering does not favor or suppress a particular value for the exciton momentum $\boldsymbol{Q}$. In particular, ignoring the form factors will not have a qualitative influence on the behavior of Γ^D close to exciton condensation, which is determined by the $\boldsymbol{Q}$ dependence of the integrand of Eq. (5.68).

5.6.1 Hartree Decoupling

When the interaction depends mostly on the transferred energy $\hbar\omega = \xi_1 - \xi_4$ and momentum $\boldsymbol{k}_p = \boldsymbol{k}_1 - \boldsymbol{k}_4 \equiv \boldsymbol{q}$ in the scattering event, the Hartree channel is the appropriate decoupling channel. We introduce an additional integral over the $\hbar\omega$ using the identity

$$\delta(\xi_1+\xi_2-\xi_3-\xi_4) = \int d\hbar\omega\,\delta(\xi_1-\xi_4-\hbar\omega)\delta(\xi_2-\xi_3+\hbar\omega), \tag{5.69}$$

and solve the momentum conserving delta function by $\boldsymbol{k}_1 = \boldsymbol{k}$, $\boldsymbol{k}_2 = \boldsymbol{k}'$, $\boldsymbol{k}_3 = \boldsymbol{k}'+\boldsymbol{q}$, and $\boldsymbol{k}_4 = \boldsymbol{k}-\boldsymbol{q}$, so that the $\boldsymbol{k}$ and $\boldsymbol{k}'$ summations in Eq. (5.68) decouple

$$\begin{aligned}\Gamma^D = & -s_\uparrow s_\downarrow \frac{\pi\beta v^2}{dV^3}\sum_{\boldsymbol{k},\boldsymbol{k}',\boldsymbol{q}}\int d\hbar\omega |W(\boldsymbol{q},hb\omega)|^2 \\ & \times \delta(\xi_\uparrow(\boldsymbol{k})-\xi_\uparrow(\boldsymbol{k}-\boldsymbol{q})-\hbar\omega) n_F(\xi_\uparrow(\boldsymbol{k}))(1-n_F(\xi_\uparrow(\boldsymbol{k}-\boldsymbol{q}))) \\ & \times \left(\frac{\boldsymbol{k}-\boldsymbol{q}}{|\boldsymbol{k}-\boldsymbol{q}|}-\hat{\boldsymbol{k}}\right)\cdot\left(\frac{\boldsymbol{k}'+\boldsymbol{q}}{|\boldsymbol{k}'+\boldsymbol{q}|}-\hat{\boldsymbol{k}}'\right) \\ & \times \delta(\xi_\downarrow(\boldsymbol{k}')-\xi_\downarrow(\boldsymbol{k}'+\boldsymbol{q})+\hbar\omega) n_F(\xi_\downarrow(\boldsymbol{k}'))(1-n_F(\xi_\downarrow(\boldsymbol{k}'+\boldsymbol{q}))).\end{aligned} \tag{5.70}$$

This can be rewritten as

$$\Gamma^D = s_\uparrow s_\downarrow \frac{\beta v^2}{4\pi dV}\sum_{\boldsymbol{k},\boldsymbol{k}',\boldsymbol{q}}\frac{|W(\boldsymbol{q},hb\omega)|^2}{\sinh^2(\beta\hbar\omega/2)}\Im m\Pi_\uparrow(\boldsymbol{q},\hbar\omega)\cdot\Im m\Pi_\downarrow(\boldsymbol{q},\hbar\omega), \tag{5.71}$$

where we defined the polarizability

$$\Pi_\sigma(\boldsymbol{q},\hbar\omega) = \frac{1}{V}\sum_{\boldsymbol{k}} \frac{n_F(\xi_\sigma(\boldsymbol{k}+\boldsymbol{q})) - n_F(\xi_\sigma(\boldsymbol{k}))}{\xi_\sigma(\boldsymbol{k}+\boldsymbol{q}) - \xi_\sigma(\boldsymbol{k}) - \hbar\omega - i0} \left(\frac{\boldsymbol{k}+\boldsymbol{q}}{|\boldsymbol{k}+\boldsymbol{q}|} - \hat{\boldsymbol{k}}\right), \tag{5.72}$$

and used that $\Pi_\sigma(\boldsymbol{q},\omega) = -\Pi_\sigma(-\boldsymbol{q},\omega)$ and $\Pi_\sigma(\boldsymbol{q},-\omega) = -\Pi^*_\sigma(\boldsymbol{q},\omega)$. Using that $\Pi_\sigma(\boldsymbol{q},\omega)$ is independent of s_σ and only has a component along $\boldsymbol{q}$, we find

$$\begin{aligned}\Pi_\sigma(\boldsymbol{q},\hbar\omega) = \frac{1}{2\pi}\int_0^\pi d\theta \int_0^\infty k dk \delta(\hbar v\sqrt{k^2+q^2+2kq\cos(\theta)} - \hbar v k - \hbar\omega) \\ \times (n_F(\hbar v\sqrt{k^2+q^2+2kq\cos(\theta)} - \mu_\sigma) - n_F(\hbar v k - \mu_\sigma)) \\ \times \left(\frac{q+k\cos(\theta)}{\sqrt{q^2+k^2+2kq\cos(\theta)}} - \cos(\theta)\right),\end{aligned} \tag{5.73}$$

where we restricted the angular integration between 0 and π. The delta function has the solution $k = k_0$ with

$$k_0 = \frac{\omega^2 - v^2q^2}{2v(qv\cos(\theta) - \omega)} \tag{5.74}$$

when $|\omega|/vq < 1$ and $\cos^{-1}(\omega/v) < \theta \equiv \theta_{min}$. After solving the delta function, Π_σ becomes

$$\begin{aligned}\Pi_\sigma(\boldsymbol{q},\hbar\omega) = \frac{\hbar}{2\pi}\frac{(vq)^2 - (\omega)^2}{2\epsilon_F}\int_{\theta_{min}}^\pi d\theta \frac{qv - \omega\cos(\theta)}{(\omega - qv\cos(\theta))^2} \\ \times \left\{ n_F\left[\left(\frac{\hbar(\omega^2 - q^2v^2)}{2(qv\cos(\theta)-\omega)} - \mu_\sigma + \hbar\omega\right)\right] - n_F\left[\left(\frac{\hbar(\omega^2-q^2v^2)}{2(qv\cos(\theta)-\omega)} - \mu_\sigma\right)\right]\right\}.\end{aligned} \tag{5.75}$$

Substitution of the result for $\Im m\Pi_\sigma$ into Eq. (5.68) leads to our final expression for Γ^D after decoupling in the Hartree channel.

5.6.2 Fock Decoupling

When the interaction depends mostly on the energy and momentum difference of the incoming $\uparrow$ particle and outgoing $\downarrow$ particle, the Fock channel is the appropriate channel to decouple the collision integral Eq. (5.35). We introduce the energy variable $\hbar\omega = \xi_1 - \xi_3$ using the identity

$$\delta(\xi_1 + \xi_2 - \xi_3 - \xi_4) = \int d\hbar\omega \delta(\xi_1 - \xi_3 - \hbar\omega)\delta(\xi_2 - \xi_4 + \hbar\omega), \tag{5.76}$$

and the momentum variable $\boldsymbol{Q} = \boldsymbol{k}_1 - \boldsymbol{k}_3$ by solving the momentum conserving delta function by $\boldsymbol{k}_1 = \boldsymbol{k} + \boldsymbol{Q}$, $\boldsymbol{k}_2 = \boldsymbol{k}'$, $\boldsymbol{k}_3 = \boldsymbol{k}$, and $\boldsymbol{k}_4 = \boldsymbol{k}' + \boldsymbol{Q}$. Then, we have

for Γ^D

$$\Gamma^D = s_\uparrow s_\downarrow \frac{\pi\beta v^2}{dV^3} \sum_{\boldsymbol{k},\boldsymbol{k}',\boldsymbol{Q}} \int d\hbar\omega |W(\boldsymbol{Q},\hbar\omega)|^2 \left(\frac{\boldsymbol{k}'+\boldsymbol{Q}}{|\boldsymbol{k}'+\boldsymbol{Q}|} - \frac{\boldsymbol{k}+\boldsymbol{Q}}{|\boldsymbol{k}+\boldsymbol{Q}|} \right) \cdot (\hat{\boldsymbol{k}}' - \hat{\boldsymbol{k}}) \\ \times \delta(\xi_\uparrow(\boldsymbol{k}+\boldsymbol{Q}) - \xi_\downarrow(\boldsymbol{k}) - \hbar\omega) n_F(\xi_\uparrow(\boldsymbol{k}+\boldsymbol{Q}))(1 - n_F(\xi_\downarrow(\boldsymbol{k}))) \\ \times \delta(\xi_\downarrow(\boldsymbol{k}') - \xi_\uparrow(\boldsymbol{k}'+\boldsymbol{Q}) + \hbar\omega) n_F(\xi_\downarrow(\boldsymbol{k}'))(1 - n_F(\xi_\uparrow(\boldsymbol{k}'+\boldsymbol{Q}))). \quad (5.77)$$

Expanding the inner product between the unit vectors, we obtain after some rewriting

$$\Gamma^D = s_\uparrow s_\downarrow \frac{\beta v^2}{2\pi dV} \sum_{\boldsymbol{k},\boldsymbol{k}',\boldsymbol{Q}} \int d\hbar\omega |W(\boldsymbol{Q},\hbar\omega)|^2 \\ \times [\Im m\Delta_0(\boldsymbol{Q},\hbar\omega)\Im m\Delta_2(\boldsymbol{Q},\hbar\omega) - \Im m\Delta_{1a}(\boldsymbol{Q},\hbar\omega) \cdot \Im m\Delta'_{1b}(\boldsymbol{Q},\hbar\omega)]. \quad (5.78)$$

where we defined the generalized susceptibility

$$\Im m\Delta_n(\boldsymbol{Q},\hbar\omega) = \frac{1}{V}\Im m \sum_{\boldsymbol{k}} F_n(\boldsymbol{k}) \frac{n_F(\xi_\uparrow(\boldsymbol{k}+\boldsymbol{Q})) - n_F(\xi_\downarrow(\boldsymbol{k}))}{\xi_\uparrow(\boldsymbol{k}+\boldsymbol{Q}) - \xi_\downarrow(\boldsymbol{k}) - \hbar\omega - i0}, \quad (5.79)$$

where $F_0(\boldsymbol{k}) = 1$, $F_{1a}(\boldsymbol{k}) = \hat{\boldsymbol{k}}$, $F_{1b}(\boldsymbol{k}) = (\boldsymbol{k}+\boldsymbol{Q})|\boldsymbol{k}+\boldsymbol{Q}|$, $F_2(\boldsymbol{k}) = \hat{\boldsymbol{k}}\cdot(\boldsymbol{k}+\boldsymbol{Q})|\boldsymbol{k}+\boldsymbol{Q}|$. The reason that these functions are more complicated than for the quadratic case is that the exciton momentum $\boldsymbol{Q}$ does not cancel from the inner product in Eq. (5.78). We note that from Eq. (5.78) we can obtain Eq. (3) from Ref. [58]. We will evaluate $\Im m\Delta$ for $s_\uparrow = 1$ and $s_\downarrow = -1$, as is appropriate to for the case of exciton condensation. Evaluating the imaginary part of Eq. (5.79), we find

$$\Im m\Delta_n(\boldsymbol{Q},\hbar\omega) = -\frac{1}{4\pi} \int k dk \int_0^{2\pi} d\theta F_n(k,\theta) \\ \times \delta(\hbar\omega + \mu_\uparrow + \mu_\downarrow - \hbar v k - \hbar v\sqrt{k^2+Q^2+2kQ\cos(\theta)}) \\ \times (1 - n_F(\hbar v\sqrt{k^2+Q^2+2kQ\cos(\theta)} - \mu_\uparrow) - n_F(\hbar v k - \mu_\downarrow)). \quad (5.80)$$

The solution of the delta function is

$$k_0 = \frac{(\hbar\omega + \mu_\uparrow + \mu_\downarrow)^2 - (\hbar v Q)^2}{2\hbar v(\hbar\omega + \mu_\uparrow + \mu_\downarrow + \hbar v Q\cos(\theta))}, \quad (5.81)$$

when $\hbar\omega + \mu_\uparrow + \mu_\downarrow > \hbar v Q$. Solving the delta function in Eq. (5.80) leads to

$$\begin{aligned}\Im m\Delta_n(\boldsymbol{Q},\hbar\omega) = \frac{(\hbar\omega+\mu_\uparrow+\mu_\downarrow)^2-(\hbar vQ)^2}{8\pi(\hbar v)^2}\int_0^\pi d\theta F_n(\theta)\\ \times\frac{(\hbar\omega+\mu_\uparrow+\mu_\downarrow)^2+(\hbar vQ)^2+2\hbar vQ(\hbar\omega+\mu_\uparrow+\mu_\downarrow)\cos(\theta)}{[(\hbar\omega+\mu_\uparrow+\mu_\downarrow)+\hbar vQ\cos(\theta)]^3}\\ \times\left[1-n_F\left(-\frac{(\hbar\omega+\mu_\uparrow+\mu_\downarrow)^2-(\hbar vQ)^2}{2[(\hbar\omega+\mu_\uparrow+\mu_\downarrow)+\hbar vQ\cos(\theta)]}+\mu_\downarrow+\hbar\omega\right)\right.\\ \left.-n_F\left(\frac{(\hbar\omega+\mu_\uparrow+\mu_\downarrow)^2-(\hbar vQ)^2}{2[(\hbar\omega+\mu_\uparrow+\mu_\downarrow)+\hbar vQ\cos(\theta)]}-\mu_\downarrow\right)\right]. \quad (5.82)\end{aligned}$$

The functions $F_n(\theta)$ are given by $F_0(\theta)=1$, $F_1(\theta)=\cos(\theta)$ and

$$F_{1b}(\theta) = \frac{[(\hbar\omega+\mu_\uparrow+\mu_\downarrow)^2+(\hbar vQ)^2]\cos(\theta)+2\hbar vQ(\hbar\omega+\mu_\uparrow+\mu_\downarrow)}{(\hbar\omega+\mu_\uparrow+\mu_\downarrow)^2+(\hbar vQ)^2+2\hbar vQ(\hbar\omega+\mu_\uparrow+\mu_\downarrow)\cos(\theta)} \quad (5.83)$$

and

$$F_2(\theta) = \frac{(\hbar\omega+\mu_\uparrow+\mu_\downarrow)^2+2\hbar vQ(\hbar\omega+\mu_\uparrow+\mu_\downarrow)\cos(\theta)+(\hbar vQ)^2\cos(2\theta)}{(\hbar\omega+\mu_\uparrow+\mu_\downarrow)^2+(\hbar vQ)^2+2\hbar vQ(\hbar\omega+\mu_\uparrow+\mu_\downarrow)\cos(\theta)}. \quad (5.84)$$

Substitution of the result for $\Im m\Pi_\sigma$ into Eq. (5.68) leads to our final expression for Γ^D after decoupling in the Fock channel, which was used in Ref. [58]. We continue by presenting an application of the formalism presented above.

5.7 Ferromagnetism in an ultracold gas

In this section we extend the results of Ref. [51], which considers the behavior of the spin drag resistivity in an ultracold Fermi gas with repulsive interactions close to the ferromagnetic transition. This transition is accompanied by magnetic fluctuations of two different characters, longitudinal and transverse fluctuations. By summing all bubble diagrams that contribute to the interaction we obtain

$$|W(\boldsymbol{k}_1,\boldsymbol{k}_2,\boldsymbol{k}_3,\boldsymbol{k}_4)|^2 = |W_L(\boldsymbol{k}_1-\boldsymbol{k}_4,\xi_1-\xi_4)|^2 + |W_T(\boldsymbol{k}_1-\boldsymbol{k}_3,\xi_1-\xi_3)|^2, \quad (5.85)$$

where W_L is the contribution from longitudinal fluctuations and W_T is the contribution from transverse fluctuations, which will be specified below. To determine the spin drag resistivity we need to evaluate the collision integral in Eq. (5.31) for this scattering amplitude. We can do this by splitting the collision integral into two integrals, one with scattering amplitude W_L and one with W_T. The former integral can be evaluated by decoupling it in the Hartree channel as described in Section 5.5.1, and the latter by decoupling it in the Fock channel as described in Section 5.5.3. The final result for the drag resistivity is then the sum of these

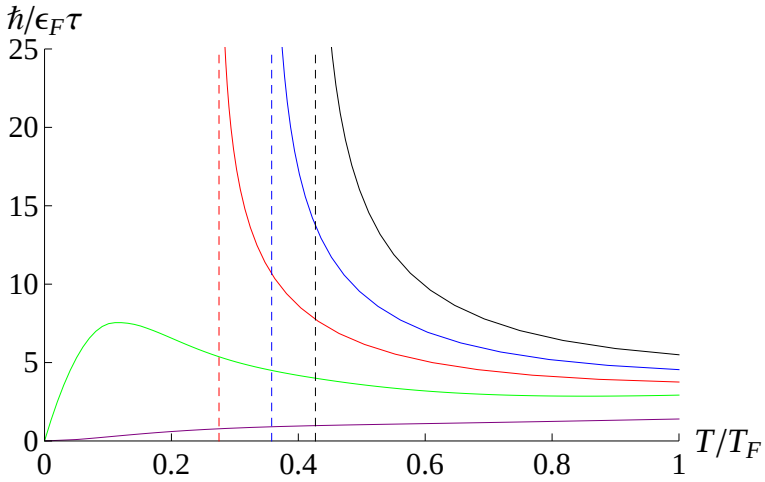

Figure 5.2: The dimensionless spin drag relaxation rate versus the temperature. The black line corresponds to $k_F a = 1.9$, the blue line to $k_F a = 1.8$, the red line to $k_F a = 1.7$, the green line to $k_F a = \pi/2$, and the purple line to $k_F a = 1.2$. The critical temperatures corresponding to the T_c values for the cases $k_F a = 1.7, 1.8, 1.9$ are indicated by the asymptotes.

two contributions. In Ref. [51], only the longitudinal fluctuations were taken into account. Instead, using our formalism, we may easily take into account the effect of both types of fluctuations.

The specific form of the scattering amplitude incorporating the longitudinal fluctuations is W_L is

$$W_L(\boldsymbol{q}, \hbar\omega) = U + \frac{U^2}{4} \frac{\Pi(\boldsymbol{q}, \hbar\omega)}{1 - U\Pi(\boldsymbol{q}, \hbar\omega)/2} - \frac{U^2}{4} \frac{\Pi(\boldsymbol{q}, \hbar\omega)}{1 + U\Pi(\boldsymbol{q}, \hbar\omega)/2}, \tag{5.86}$$

where $\Pi(\boldsymbol{q}, \hbar\omega) = \Pi_\uparrow(\boldsymbol{q}, \hbar\omega) + \Pi_\downarrow(\boldsymbol{q}, \hbar\omega)$ with $\Pi_\sigma(\boldsymbol{q}, \hbar\omega)$ given in Eq. (5.38), and where U is the contact interaction strength given by $U = 4\pi a\hbar^2/m$ with a the s-wave scattering length. The specific form of the scattering amplitude incorporating the transverse fluctuations is W_F is

$$W_T(\boldsymbol{Q}, \hbar\omega) = -\frac{U^2}{2} \frac{\Delta(\boldsymbol{Q}, \hbar\omega)}{1 + U\Delta(\boldsymbol{Q}, \hbar\omega)/2}, \tag{5.87}$$

where $\Delta(\boldsymbol{Q}, \hbar\omega) = 2\Delta_0(\boldsymbol{Q}, \hbar\omega)$ with Δ_0 given in Eq. (5.61).

The result of the complete calculation is shown in Fig. 5.2, where we shown the dimensionless spin drag relaxation rate versus the temperature. The spin drag relaxation rate is obtained from the drag resistivity by a the Drude formula $\rho_D = m/2n\tau$. In Fig. 5.2 we see that spin drag relaxation rate is enhanced close

to the critical temperature and diverges when approaching T_c from above. Closer inspection shows that this divergence is logarithmic.

Comparing our results to Ref. [51] (specifically to Fig. 1 from that work), we see that including the transverse fluctuations changes the character of the enhancement. If only longitudinal fluctuations are taken into account, the spin drag relaxation rate is enhanced but remains finite when approaching the critical temperature. Inclusion of the transverse fluctuations is vital to be able to obtain the correct, logarithmic, character of the enhancement close to T_c.

5.8 Conclusions

In conclusion, we have presented a general formalism to determine the drag resistivity in systems close to a phase transition. We show that by decoupling the collision integral in the appropriate channel, we can take into account the effect of gaussian critical fluctuations close the phase transition. Our theory is valid for both two and three dimensions, linear and quadratic dispersions, arbitrary mass and density imbalance, and bands of both positive and negative character. As an application, we determined the spin drag relaxation rate in an ultracold Fermi gas close to the ferromagnetic transition, for which we need to take into account fluctuations in two different channels.

5.9 Appendix

We show how to take the drift momenta $\boldsymbol{k}^{\text{drift}}$ out of the summation in Eq. (5.26)

$$\begin{aligned}\boldsymbol{\Gamma}_\uparrow = &-\frac{2\pi\beta}{2\hbar^2 V^3}\sum_{\boldsymbol{k}_i}\delta_{\boldsymbol{k}_i}\delta(\xi_i)|W|^2 n_1 n_2(1-n_3)(1-n_4)\\ &\times(\partial_{\boldsymbol{k}}\xi_4-\partial_{\boldsymbol{k}}\xi_1)\left[s_\uparrow\boldsymbol{k}_\uparrow^{\text{drift}}\cdot(\partial_{\boldsymbol{k}}\xi_4-\partial_{\boldsymbol{k}}\xi_1)+s_\downarrow\boldsymbol{k}_\downarrow^{\text{drift}}\cdot(\partial_{\boldsymbol{k}}\xi_3-\partial_{\boldsymbol{k}}\xi_2)\right].\end{aligned}\tag{5.88}$$

For a quadratic dispersion this is easy, since $\partial_{\boldsymbol{k}}\xi_i\propto\boldsymbol{k}_i$. Using momentum conservation $\boldsymbol{k}_1+\boldsymbol{k}_2=\boldsymbol{k}_3+\boldsymbol{k}_4$ and that

$$\int d\boldsymbol{q}F(q)\boldsymbol{q}(\boldsymbol{q}\cdot\boldsymbol{k}^{\text{drift}})=\frac{\boldsymbol{k}^{\text{drift}}}{d}\int d\boldsymbol{q}F(q)\boldsymbol{q}^2,\tag{5.89}$$

where $F(q)$ is a function that only depends on the length of q, immediately leads to the results Eqs. (5.29,5.30,5.31). When we have a two dimensional system with linear dispersion, then $\partial_{\boldsymbol{k}}\xi\propto\hat{\boldsymbol{k}}$. The collision integral $\boldsymbol{\Gamma}_\uparrow$ in Eq. (5.26) is invariant under a global rotation of all integration vectors, in particular, operating with

$$\frac{1}{2\pi}\int d\phi\tag{5.90}$$

where the angle ϕ is a global rotation angle around an z-axis of all vectors $\boldsymbol{k}_i$, leaves the integral invariant. The delta functions's, the interaction and the Fermi functions do not depend on ϕ. We write the integral for a general ϕ dependent term

$$\frac{1}{2\pi}\int d\phi \boldsymbol{k}_a(\boldsymbol{k}^{\mathrm{drift}}\cdot\boldsymbol{k}_b) = \frac{k_a k_b}{2\pi}\int d\phi \begin{pmatrix}\cos(\phi+\phi_a)\\ \sin(\phi+\phi_a)\end{pmatrix}\left[\begin{pmatrix}k_x^{\mathrm{drift}}\\ k_y^{\mathrm{drift}}\end{pmatrix}\cdot\begin{pmatrix}\cos(\phi+\phi_b)\\ \sin(\phi+\phi_b)\end{pmatrix}\right], \tag{5.91}$$

where $\boldsymbol{k}_a$ and $\boldsymbol{k}_b$ are momenta being summed Eq. (5.26), and we choose the x-axis along the external drift momentum $\boldsymbol{k}^{\mathrm{drift}}$, where $\boldsymbol{k}_a$ and $\boldsymbol{k}_b$ can either be the same or different. Now, reflecting the whole integrand in the x-axis and then doing the integral gives the same answer. This sends all angles ϕ_i to $-\phi_i$. Again, the delta functions's, interaction, and Fermi functions do not depend on ϕ and the sign of the angles, so we get the term

$$\frac{1}{2\pi}\int d\phi \boldsymbol{k}_a(\boldsymbol{k}^{\mathrm{drift}}\cdot\boldsymbol{k}_b) = \frac{k_a k_b}{2\pi}\int d\phi \begin{pmatrix}\cos(\phi-\phi_a)\\ \sin(\phi-\phi_a)\end{pmatrix}\left[\begin{pmatrix}k_x^{\mathrm{drift}}\\ k_y^{\mathrm{drift}}\end{pmatrix}\cdot\begin{pmatrix}\cos(\phi-\phi_b)\\ \sin(\phi-\phi_b)\end{pmatrix}\right], \tag{5.92}$$

Now, we can take the integrals over ϕ and perform the average of the two terms, leading to the replacement rule

$$\boldsymbol{k}_a(\boldsymbol{k}^{\mathrm{drift}}\cdot\boldsymbol{k}_b) \quad\rightarrow\quad \frac{1}{2}\boldsymbol{k}^{\mathrm{drift}}(\boldsymbol{k}_a\cdot\boldsymbol{k}_b), \tag{5.93}$$

which can be used to obtain Eqs. (5.29,5.30,5.31). Note that for the special case $\boldsymbol{k}_a = \boldsymbol{k}_b$, we recover the result for used for the quadratic dispersion.

Samenvatting

Een van de meest interessante aspecten van de moderne natuurkunde is het bestuderen van faseovergangen. Wanneer een parameter (bijvoorbeeld de temperatuur) van een systeem verandert, kan de fase van het systeem veranderen in een andere fase. Al op jonge leeftijd kennen kinderen het voorbeeld van het bevriezen van water wanneer de temperatuur daalt tot onder 0 graden Celsius. Met name in Nederland kan het belang van deze faseovergang niet worden overschat. Elke winter houdt het hele land de adem in in afwachting of er een voldoende dikke laag ijs komt bovenop de kanalen en meren, zodat men kan gaan schaatsen. Een andere faseovergang die geworteld is in de Nederlandse geschiedenis is supergeleiding. In 1911 ontdekte Kamerlingh Onnes in Leiden dat als je kwik afkoelt tot onder 4 Kelvin, de elektrische weerstand nul wordt. Het blijkt dat kwik dan overgaat in een supergeleidende toestand. De plotselinge daling van de elektrische weerstand is slechts één van de vele interessante eigenschappen van deze toestand.

De elektrische weerstand is een zogenaamde transportcoëfficiënt: hij relateert de kracht op de elektronen in kwik (de spanning) aan het transport van lading door deze kracht (de elektrische stroom). De waarde van deze transportcoëfficiënt hangt nauw samen met de fase van het systeem. De aanwezigheid van de faseovergang heeft zelfs al invloed op het gedrag van de weerstand boven de overgangstemperatuur. In het geval van kwik onderdrukken kritische fluctuaties de weerstand. Dit fenomeen kan worden gebruikt als voorbode van de faseovergang: door te kijken naar het gedrag van de transportcoëfficiënt boven de overgangstemperatuur kun je de aanwezigheid van de faseovergang bij lagere temperatuur afleiden.

Dit fenomeen is het belangrijkste onderwerp van dit proefschrift. We bestuderen het gedrag van de zogenaamde drag weerstand in verschillende fysische systemen nabij een faseovergang. De drag weerstand is het vermogen van een groep deeltjes die bewegen om een andere groep mee te sleuren. Stel je een groep deeltjes van type A voor die bewegen in een bepaalde richting. De deeltjes kunnen interageren met elkaar, maar dit verandert de totale impuls van de groep niet. Een groep deeltjes van een ander type B staat stil en wordt in contact gebracht met de bewegende type A deeltjes. Als de deeltjes van verschillende types interageren is er impuls overdracht tussen de twee groepen: de impuls van de groep A zal afnemen en die van groep B zal toenemen. Op deze wijze worden de deeltjes B

meegesleurd door de A deeltjes. De drag (sleur) weerstand geeft aan hoe effectief dit proces is.

In dit proefschrift beschouwen we heel verschillende fysische systemen: dubbellaagstructuren in vaste stoffen en koude atomaire gassen. De laatste zijn heel ijle gassen van atomen die kunnen worden afgekoeld (afgeremd) door ze te beschijnen met laserlicht. Als zo'n gas voldoende koud is, kan (in het geval van bosonen) Bose-Einstein condensatie plaatsvinden. Dit houdt in dat er een macroscopische hoeveelheid deeltjes zich in de grond toestand bevindt. Omdat deze deeltjes zich gedragen als een materiegolf, heeft deze toestand vele interessante kwantummechanische eigenschappen. In het geval van fermionen kan er geen Bose-Einstein condensatie van de atomen plaatsvinden, omdat er slechts een fermion in elke toestand kan zitten. Wat wel kan, is dat twee fermionen een paar vormen. Deze paren zijn bosonen en zij kunnen wel Bose-Einstein condenseren. Supergeleiding in kwik kan worden gezien als Bose-Einstein condensatie van paren van elektronen.

Het andere type systeem dat we in dit proefschrift bestuderen zijn dubbellaag structuren in vaste stoffen. Het is mogelijk om twee parallelle lagen te maken met een vaste onderlinge afstand. Elektronen kunnen zich bewegen in deze lagen, maar kunnen zich niet verplaatsen van de ene naar de andere laag. Het wordt interessant wanneer we de elektronen in een van de twee lagen vervangen door gaten. Deze gaten kan je zien als lege toestanden in een verder volledig gevulde band van elektronen. De gaten zijn positief geladen en kunnen paren vormen met de elektronen in de andere laag. Deze paren worden ook wel excitonen genoemd en zij zijn bosonen en kunnen Bose-Einstein condenseren.

In dit proefschrift bestuderen we het gedrag van de drag weerstand nabij deze twee faseovergangen, de Bose-Einstein condensatie van fermion paren in koude gassen en de condensatie van excitonen in dubbellaagstructuren in vaste stoffen.

Acknowledgements

Als eerste wil ik hier graag mijn begeleider Rembert Duine bedanken. Zijn informele en toegankelijke manier van begeleiden waardeer ik erg. Ik kon altijd langskomen met vragen en problemen wanneer ik even vast zat, en verliet dan eigenlijk altijd zijn kamer met een antwoord of oplossing, zodat ik weer verder kon. Ook Henk Stoof wil ik bedanken voor zijn enthousiasme en inbreng bij onze besprekingen. Furthermore, I would like to thank Allan MacDonald and Giovanni Vignale for pleasant collaborations, and Marco Polini for giving me the chance to work with him in Pisa. En Vivian Jacobs voor haar bijdrage aan het vierde hoofdstuk van dit proefschrift.

Ik wil mijn kamergenoot Wouter bedanken. Ik hoop dat ik hem niet te veel lastig gevallen heb met mijn vragen en de momenten dat ik even wat stoom moest afblazen. Alice, Chris, Hedwig, Jasper, Ralph en Wilke voor de gesprekken en de gezelligheid en de hele BEC groep for de koffiepauzes en group meetings.

Voor de organisatorische ondersteuning Biene, Joost, Geertje, Wilma, Olga, Els, Marion en Riny. Tenslotte, mijn ouders, mijn broer Sander, en mijn vrouw Ninke voor hun steun.

Curriculum Vitae

Martijn Mink werd geboren op 24 december 1984 in Geldrop. Het voorbereidend wetenschappelijk onderwijs doorliep hij op het Augustinianum te Eindhoven, waar hij in 2003 het gymnasiumdiploma behaalde. In 2003 begon hij aan bachelorstudies Natuur- en Sterrenkunde en Wiskunde aan de Universiteit Utrecht die hij in 2006 cum laude afrondde. Daarna startte hij zijn masterstudie Theoretische Natuurkunde aan de Universiteit Utrecht. In 2008 studeerde hij cum laude af, na voltooiing van zijn masteronderzoek naar de pinning van vortices in twee-components gecondenseerde bosonische gassen door een optisch rooster onder begeleiding van prof. dr. Cristiane Morais Smith en dr. Rembert Duine. Na zijn studie startte hij zijn promotieonderzoek onder begeleiding van dr. Rembert Duine aan het Instituut voor Theoretische Fysica van de Universiteit Utrecht.

Bibliography

[1] H. Kamerlingh Onnes, Akad. van Wetenschappen **14**, 818 (1911).

[2] T. J. Gramila, J. P. Eisenstein, A. H. MacDonald, L. N. Pfeiffer, and K. W. West, Phys. Rev. Lett. **66**, 1216 (1991).

[3] M. H. Anderson, J. R. Ensher, M. R. Matthews, C. E. Wieman, and E. A. Cornell, Science **14**, 198 (1995).

[4] J. Bardeen, L. N. Cooper, and J. R. Schrieffer, Phys. Rev. **106**, 162 (1957).

[5] H. T. C. Stoof, M. Houbiers, C. A. Sackett, and R. G. Hulet, Phys. Rev. Lett. **76**, 10 (1996).

[6] C. A. Regal, M. Greiner, and D. S. Jin, Phys. Rev. Lett. **92**, 040403 (2004).

[7] A. Sommer, M. Ku, G. Roati, and M. W. Zwierlein, Nature **472**, 201 (2011).

[8] U. Sivan, P. M. Solomon, and H. Shtrikman, Phys. Rev. Lett. **68**, 1196 (1992).

[9] A. High, J.R. Leonard, A.T. Hammack, M.M. Fogler, L.V. Butov, A.V. Kavokin, K.L. Campman, A.C. Gossard, Nature **483**, 584 (2012).

[10] K. S. Novoselov, A. K. Geim, S. V. Morozov, D. Jiang, Y. Zhang, S. V. Dubonos, I. V. Grigorieva, and A. A. Firsov, Science **306**, 666 (2004).

[11] Y. Xia *et al.*, Nature Phys. **5**, 398 (2009).

[12] A. Altland and B. Simons, *Condensed Matter Field Theory*, Cambridge University Press, Cambridge, 2006.

[13] A. H. Castro Neto, F. Guinea, N. M. R. Peres, K. S. Novoselov, and A. K. Geim, Rev. Mod. Phys. **81**, 109 (2009).

[14] Yu. E. Lozovik and A. A. Sokolik, JETP Lett. 87, **55** (2008).

[15] C.-H. Zhang and Yogesh N. Joglekar, Phys. Rev. B **77**, 233405 (2008).

[16] Hongki Min, Rafi Bistritzer, Jung-Jung Su, and A. H. MacDonald, Phys. Rev. B **78**, 121401 (2008).

[17] J.P. Eisenstein and A.H. MacDonald, Nature **432**, 691 (2004).

[18] J.J. Su and A.H. MacDonald, Nature Phys. **4**, 799 (2008).

[19] H. Schmidt, T. Ludtke, P. Barthold, E. McCann, V. I. Fal'ko, and R. J. Haug, Appl. Phys. Lett. **93**, 172108 (2008).

[20] Seyoung Kim, Insun Jo, Junghyo Nah, Z. Yao, S. K. Banerjee, and E. Tutuc, Phys. Rev. B **83**, 161401 (2011).

[21] B. Seradjeh, H. Weber, and M. Franz, Phys. Rev. Lett. **101**, 246404 (2008).

[22] Maxim Yu. Kharitonov and Konstantin B. Efetov, Phys. Rev. B **78**, 241401 (2008).

[23] R. Bistritzer, H. Min, J. J. Su, A.H. MacDonald, arXiv:0810.0331v1.

[24] Maxim Yu. Kharitonov, Konstantin B. Efetov, Semicond. Sci. Technol. **25**, 034004 (2010).

[25] Yu. E. Lozovik and A. A. Sokolik, Eur. Phys. J. B **25**, 195206 (2010).

[26] See for example E. V. Gorbar, V. P. Gusynin, V. A. Miransky, and I. A. Shovkovy, Phys. Rev. B **66**, 045108 (2002); D. V. Khveshchenko and H. Leal, Nucl. Phys. B **687**, 323 (2004); I. F. Herbut, Phys. Rev. Lett. **97**, 146401 (2006); J. E. Drut and T. A. Lähde, Phys. Rev. Lett. **102**, 026802 (2009) and work cited therein.

[27] See for example S. Y. Zhou, G.-H. Gweon, J. Graf, A. V. Fedorov, C. D. Spataru, R. D. Diehl, Y. Kopelevich, D.-H. Lee, Steven G. Louie, and A. Lanzara, Nat. Phys. **2**, 595 (2006); Aaron Bostwick, Taisuke Ohta, Thomas Seyller, Karsten Horn, and Eli Rotenberg, Nat. Phys. **3**, 36 (2007); Aaron Bostwick, Florian Speck, Thomas Seyller, Karsten Horn, Marco Polini, Reza Asgari, Allan H. MacDonald, and Eli Rotenberg, Science **328**, 999 (2010).

[28] Joseph G. Checkelsky, Lu Li, and N. P. Ong, Phys. Rev. B **79**, 115434 (2009). *ibid*, Phys. Rev. Lett. **100**, 206801 (2008); See also Yue Zhao, Paul Cadden-Zimansky, and Philip Kim, Bull. Am. Phys. Soc. (2010). [Abstract available at http://adsabs.harvard.edu/abs/2010APS..MARV22006Z]

[29] V. P. Gusynin, V. A. Miransky, S. G. Sharapov, and I. A. Shovkovy, Phys. Rev. B **74**, 195429 (2006); I. F. Herbut, Phys. Rev. Lett. **97**, 146401 (2006); Phys. Rev. B **75**, 165411 (2007).

[30] K. Nomura and A. H. MacDonald, Phys. Rev. Lett. **96**, 256602 (2006); K. Yang, S. Das Sarma, and A. H. MacDonald, Phys. Rev. B **74**, 075423 (2006); M. O. Goerbig, R. Moessner, and B. Douçot, *ibid.* **74**, 161407 (2006); J. Alicea and M. P. A. Fisher, *ibid.* **74**, 075422 (2006).

[31] Yafis Barlas, T. Pereg-Barnea, Marco Polini, Reza Asgari, and A. H. MacDonald, Phys. Rev. Lett. **98**, 236601 (2007).

[32] D. Basu, L. F. Register, Dharmendar Reddy, A. H. MacDonald, and S. K. Banerjee, Phys. Rev. B **82**, 075409 (2010).

[33] Lih-King Lim, C. Morais Smith, and H. T. C. Stoof , Phys. Rev. A **78**, 013634 (2008).

[34] Mitsutaka Fujita, Katsunori Wakabayashi, Kyoko Nakada, and Koichi Kusakabe, J. Phys. Soc. Jpn. **65**, 1920 (1996); S. Sorella and E. Tosatti, Europhys. Lett. **19**, 699 (1992); L. M. Martelo, M. Dzierzawa, L. Siffert, and D. Baeriswyl, Z. Phys. B **103**, 335 (1997). T. Paiva, R. T. Scalettar, W. Zheng, R. R. P. Singh, and J. Oitmaa, Phys. Rev. B **72** 085123 (2005).

[35] E. H. Hwang and S. Das Sarma, Phys. Rev. B **75**, 205418 (2007).

[36] N. B. Kopnin and E. B. Sonin, Phys. Rev. Lett. **100**, 246808 (2008).

[37] M.Z. Hasan and C.L. Kane, Rev. Mod. Phys. **82**, 3045 (2010); X.-L. Qi and S.-C. Zhang, Rev. Mod. Phys. **83**, 1057 (2011).

[38] B. Seradjeh, J.E. Moore, and M. Franz, Phys. Rev. Lett. **103**, 066402 (2009); see also Z. Wang *et al.*, arXiv:1106.5838.

[39] A.G. Rojo, J. Phys.: Condens. Matter **11**, R31 (1999).

[40] A.F. Croxall *et al.*, Phys. Rev. Lett. **101**, 246801 (2008).

[41] J.A. Seamons *et al.*, Phys. Rev. Lett. **102**, 026804 (2009).

[42] Ben Yu-Kuang Hu, Phys. Rev. Lett. **85**, 820 (2000).

[43] G. Vignale and A.H. MacDonald, Phys. Rev. Lett. **76**, 2786 (1996).

[44] W.-K. Tse, Ben Yu-Kuang Hu, and S. Das Sarma, Phys. Rev. B **76**, 081401(R) (2007); N.M.R. Peres, J.M.B. Lopes dos Santos, and A.H. Castro Neto, Europhys. Lett. **95**, 18001 (2011); M.I. Katsnelson, Phys. Rev. B **84**, 041407(R) (2011); E.H. Hwang and S. Das Sarma, arXiv:1105.3203v1.

[45] The interaction in Eq. (3.1) accounts for s-wave pairing fluctuations and correctly incorporates the low K and small Ω behavior of the interaction, which determines the behavior of the drag resistivity close to T_c. Any other dependence on the momenta due to the Coulomb interaction or wave function overlap does not alter the temperature dependence of the drag resistivity close to T_c and is effectively incorporated in U. However, the momentum dependence of the wave function overlap has been fully taken into account in our calculations of T_c in Fig. 3.1.

[46] In the absence of pairing fluctuations, the dominant low-temperature behavior is $\rho_D \propto T^2 \log(T)$ and not $\rho_D \propto T^2$. The logarithmic correction is an artifact of the contact interaction used.

[47] Berezinskii-Kosterlitz-Thouless (BKT) phase fluctuations tend to suppress T_c with respect to our mean-field estimate. The BKT temperature is given by $T_{BKT} = \pi\rho_s(T_{BKT})/2$, where $\rho_s(T)$ is the superfluid density, which can be estimated from a mean-field analysis. For DLG exciton condensates this analysis has been carefully carried out in Ref. [16].

[48] The T_c-equation is $1 = (1/A)\sum_{\boldsymbol{k}} V_{sep}^2(k)[n(\epsilon_t(\boldsymbol{k})) - n(\epsilon_b(\boldsymbol{k}))]/[\epsilon_b(\boldsymbol{k}) - \epsilon_t(\boldsymbol{k})]$, where $V_{sep}(k)$ is a separable approximation to the angular average of V_0 over incoming and outgoing momenta, *i.e.* $V_{sep}(k) = V_{av}(k, k_F)/\sqrt{V_{av}(k_F, k_F)}$ with $V_{av}(k, k') = \int d\phi\, V_0(q)|_{q=|\boldsymbol{k}-\boldsymbol{k}'|}\,[1+\cos(\phi)]/(4\pi)$, where we have included the form factor $[1 + \cos(\phi)]/2$ relevant for this system [Yu. E. Lozovik and A.A. Sokolik, Eur. Phys. J. B **73**, 195 (2010); M.P. Mink *et al.*, Phys. Rev. B **84**, 155409 (2011)].

[49] R.E.V. Profumo *et al.*, Phys. Rev. B **82**, 085443 (2010).

[50] R. Kittinaradorn, R.A. Duine, and H.T.C. Stoof, arXiv:1107.2024.

[51] R.A. Duine, Marco Polini, H.T.C. Stoof, G. Vignale, Phys. Rev. Lett.. **104**, 220403 (2010). R. A. Duine, M. Polini, A. Raoux, H. T. C. Stoof, and G. Vignale, New J. Phys. **13** 045010 (2011).

[52] See *e.g.* B. Wunsch *et al.*, New J. Phys. **8**, 318 (2006).

[53] Edward Taylor, Shizhong Zhang, William Schneider, and Mohit Randeria, Phys. Rev. A **84**, 063622 (2011).

[54] G. M. Bruun, New J. Phys. **13**, 035005 (2011).

[55] H. J. van Driel, R. A. Duine, and H. T. C. Stoof, Phys. Rev. Lett.. **105**, 155301 (2010).

[56] S. Riedl, E. R. Snchez Guajardo, C. Kohstall, A. Altmeyer, M. J. Wright, J. Hecker Denschlag, R. Grimm, G. M. Bruun, and H. Smith, Phys. Rev. A **78**, 053609 (2008).

[57] G. M. Bruun and H. Smith, Phys. Rev. A **72**, 043605 (2005).

[58] M. P. Mink, H. T. C. Stoof, R.A. Duine, Marco Polini, G. Vignale, Phys. Rev. Lett. **108**, 186402 (2012).

[59] See Chih-Chun Chien, Hao Guo, Yan He, and K. Levin, Phys. Rev. A **81**, 023622 (2010), and references therein.

[60] F. Palestini, P. Pieri, G. C. Strinati, Phys. Rev. Lett. **108**, 080401 (2012). Chi-Chun Chien, Hao Guo, K. Levin, arXiv:1202.5590v1.

[61] Alessio Recati and Sandro Stringari, Phys. Rev. Lett. **106**, 080402 (2011).

[62] K. B. Gubbels and H. T. C. Stoof, Phys. Rev. Lett. **100**, 140407 (2008).

[63] Satoshi Fujimoto, J. Phys. Soc. Jpn. **71** 1230 (2002).

[64] S.B. Koller, A. Groot, P.C. Bons, R.A. Duine, H.T.C. Stoof, P. van der Straten, arXiv:1204.6143.